THE UNIVERSITY OF CALGARY

Auroral Field-Aligned Currents Observed by OEDIPUS-C

by

Sheldon Franchuk

A THESIS

SUBMITTED TO THE FACULTY OF GRADUATE STUDIES

IN PARTIAL FULFILLMENT OF THE REQUIREMENTS FOR THE

DEGREE OF MASTER OF SCIENCE

DEPARTMENT OF PHYSICS AND ASTRONOMY

CALGARY, ALBERTA

September, 2000

Abstract

Auroral field-aligned current structures as determined by magnetic field observations from the OEDIPUS-C sounding rocket were analyzed in conjunction with measurements of electron flux. Within one inverted-V region, magnetometer current measurements appear more structured than electron flux. Electrons outside the energy or angular range of the detector may be responsible for carrying these smaller-scale currents.

Intense currents in the early stages and near the end of the flight were matched more closely with regions of depleted electron precipitation (downward current) and inverted-V events (upward current).

Analysis of auroral structures was compared to the positions of currents along the flight path of OEDIPUS-C. Results from this comparison show some correlation between auroral arc edges and upward currents.

There is substantial spatial structure in ionospheric currents. The structure of these currents appear at times to be distinct from the electron precipitation responsible for the aurora.

Acknowledgments

Many individuals provided information used for this thesis. I wish to acknowledge Dr. Gordon James for the electron density plot from the HEX/REX instrument, James Trickey and the CANOPUS team for the CANOPUS magnetometer data, Dr. Roger Smith for the Poker Flat meridian scanning photometer data, Dr. Paul Prikryl for the Kaktovic stacked plot, and Dr. John Olson for use of the GIMA magnetometer array data.

I also wish to thank Brenda Tschanz for all her assistance, Cliff Marcellus for computer support, Johnathan Burchill for watching my back, and the rest of the sixth floor personnel for putting up with me much longer than they needed to.

Finally, I wish to thank Dr. Don Wallis for allowing me access to his data, and Dr. Dave Knudsen for his patience and support in allowing me this opportunity.

Table of Contents

List of Tables

List of Figures

Chapter 1

Introduction

1.1 The Geomagnetic Environment

The earth possesses an intrinsic magnetic field. This field is essentially dipolar, and measures ~0.65 Gauss (6.5×10^4 nT) at the surface of the planet at high latitudes. This field extends outward, creating an envelope in interplanetary space known as the magnetosphere. In the absence of outside influences, earth's magnetosphere would extend to an arbitrarily large distance. However, the dipolar configuration of the geomagnetic field becomes significantly altered. This alteration is due to the existence of an extended interplanetary magnetic field and charged particle flux, both originating from the sun. The interactions between these structures and the geomagnetic field produce the distinctive shape of the earth's magnetosphere (figure 1.1).

The interplanetary magnetic field (IMF) is an extension of the sun's intrinsic field. Heliomagnetic field lines are propelled outward by the solar wind, producing a complex field structure that extends into deep interplanetary space. At the orbital distance of the earth, the IMF has a typical strength of a few 10's of nT. The direction of the field can change rapidly, and this changing field direction can have a profound effect on the earth's magnetic environment.

The value of the IMF perpendicular to the ecliptic plane is a dominant factor in how the IMF field lines interact with the geomagnetic lines. When the IMF has

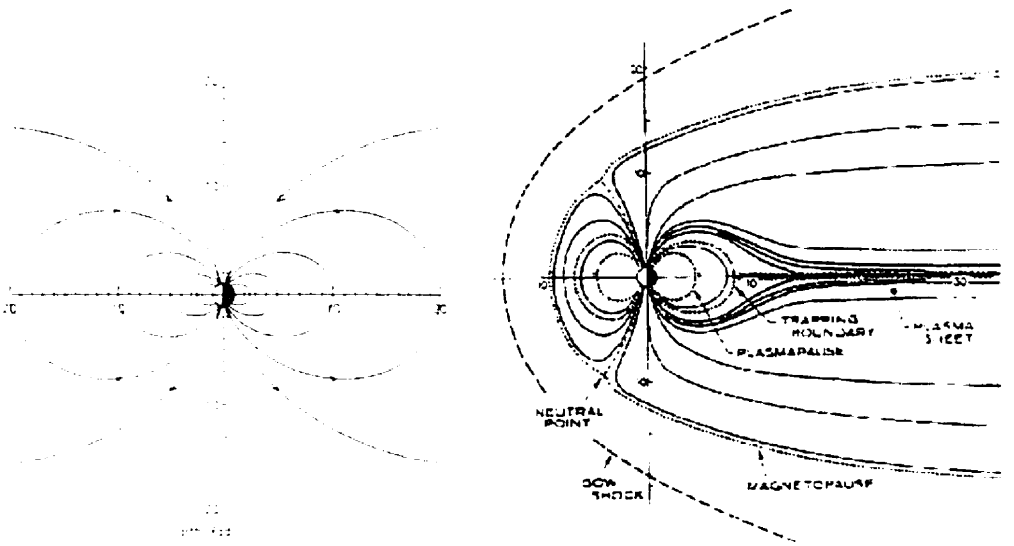

Figure 1.1: Dipole magnetic field compared to field immersed in solar wind and IMF. The sun is to the left in both diagrams.

a positive (northward) component, the interaction between the geomagnetic regime and the interplanetary regime is minimized. For negative, or southward, IMF, the field lines merge in a process called reconnection. This reconnection allows the two regimes to transfer particles and energy more freely, and this process provides an important source of energy and plasma for the magnetosphere.

The solar wind is the flow of plasma produced by the sun. Processes in the corona accelerate charged particles (mostly electrons and protons) to supersonic speeds. Once these particles reach the earth, they have a density of roughly $10/cm^3$ and speeds between 300 and 800 km/s [*Parks*, 1991]. A shock front is formed by the magnetic field of the earth acting as an obstacle in the solar wind path. This shock front creates the bow shock, a structure defining the sunward edge of the magnetosphere. As the solar wind flows around the earth, the plasma affects the

shape of the dipole field. The sunward side is compressed to roughly 10 earth radii, and the nightside field lines get dragged by the particles, stretching the field into a tail that extends more than 100 earth radii.

1.2 Particles in Magnetic Fields

The density of particles in the magnetospheric plasma is low ($< 1 - 1000/\mathrm{cm}^3$). This plasma is strongly affected by the geomagnetic field.

Particles with velocity $\vec{v}$ and charge q will be deflected in the presence of a magnetic field $\vec{B}$ due to the Lorentz force:

$$\vec{F} = q\vec{v} \times (\vec{B}) \tag{1.1}$$

The motion of the particle can be described in terms of velocities parallel to and perpendicular to the magnetic field:

$$\vec{v} = \vec{v}_{||} + \vec{v}_{\perp} \tag{1.2}$$

In a uniform field, a particle will travel in a helical path, with the radius r_c of the circle it traces around the field line (gyroradius) determined by $v_\perp$:

$$r_c = \frac{mv_\perp}{qB} \tag{1.3}$$

For processes that change slowly over a particle's gyroperiod $\frac{r_c}{v_\perp}$, the quantity $\mu = \frac{mv_\perp^2}{B}$ (magnetic moment) can be considered a constant, $\frac{\mathrm{d}\mu}{\mathrm{dt}} = 0$. This constant is known as the first adiabatic invariant.

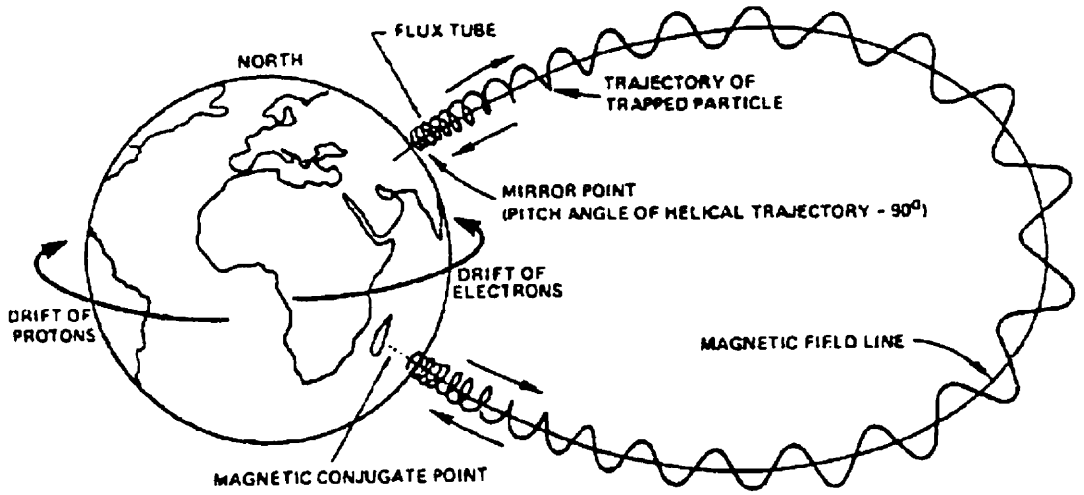

Figure 1.2: Cyclotron motion of electrons in Earth's magnetic field, courtesy [*Spjeldvik and Rothwell*, 1985]

The angle between the direction of the magnetic field and a particle's trajectory is referred to as the "pitch angle," denoted α.

$$\alpha = \tan^{-1}\left|\frac{v_\perp}{v_\parallel}\right| \tag{1.4}$$

If the magnetic field is non-uniform, such as the geomagnetic field (figure 1.2), the pitch angle will change, as energy conservation reduces the parallel component of velocity as $\vec{v}_\perp$ increases due to increasing magnetic field strength to maintain the first adiabatic invariant. Eventually, $\vec{v}_\parallel = 0$, and the particle reverses direction. The point at which this occurs is known as the "mirror point". Since the field is essentially symmetric about the poles, the particles mirror back and forth between the mirror points in either hemisphere, known as magnetic conjugate points.

The altitude at which a particle in earth's magnetic field mirrors is determined

by the pitch angle at the equator, where the field is the weakest and mostly parallel to the surface of the earth. In the magnetosphere, particle densities are low and collisions between particles are rare. Traveling through this region, a particle with a large pitch angle can remain trapped between mirror points until a random collision or interaction with a plasma wave changes the pitch angle of the particle. The Van Allen radiation belts are an example of trapped particles. Very energetic (> 1 MeV) cosmic ray components populate this region, and individual particles can remain trapped for years in these rings of plasma that encircle the earth. Particles with smaller pitch angle mirror closer to the surface of the earth. At altitudes below 100 km, the atmosphere is dense enough that collisions are common. A particle mirroring at this altitude can be lost, as it collides with an atmospheric particle and loses its energy. These lost particles fall within the "loss cone", the range of pitch angles for which particles mirror below roughly 100 km altitude.

1.3 Sources of Magnetospheric Particles

The ions and electrons in the magnetosphere form a plasma environment that supports electrical currents that drive the dynamic features of the magnetosphere. The plasma originates from the ionosphere, the solar wind, and from cosmic ray sources (Van Allen belts). Not all processes which contribute to the magnetospheric plasma are known.

Outflow from the ionosphere injects both light (H^+, He^{++}) and heavy ions (e.g. O^+, He^+) into the magnetosphere. The solar wind can transfer light ions into the magnetosphere via select processes that bypass the magnetopause boundary. These

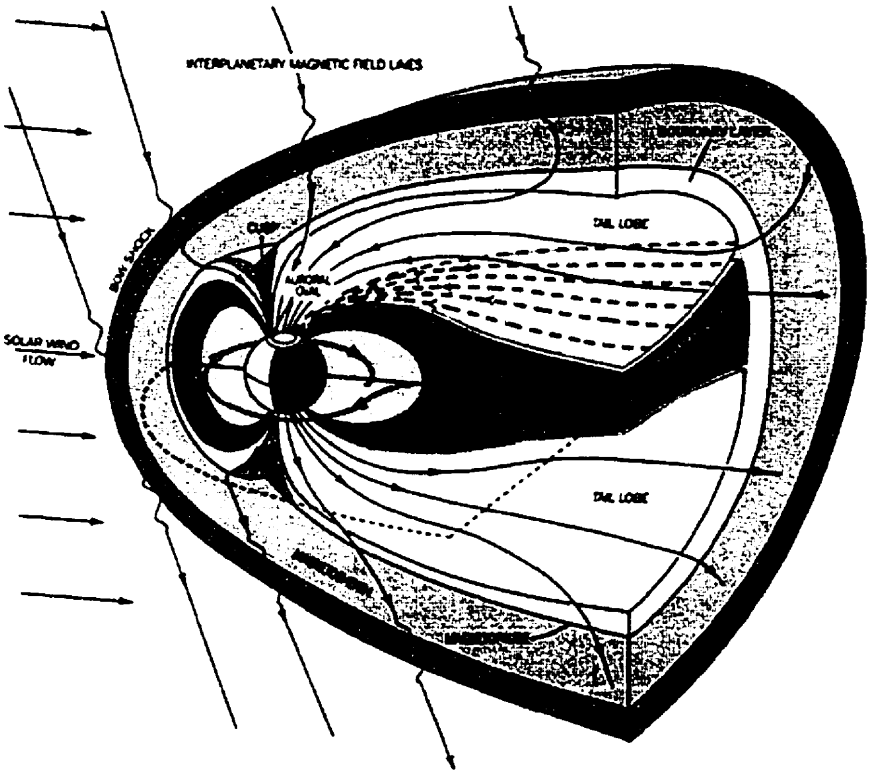

Figure 1.3: Magnetospheric regions, from *Burke et al.* [1985]

processes include reconnection, and entry through gaps in the magnetopause at the cusp (region between field lines that close on the sunward side and those that close on the nightside) and tail (see figure 1.3). More complex processes are thought to exist as well, such as wave-particle interactions that transport particles across field lines.

Once in the magnetosphere, this plasma is transported via convection to the various regions shown in figure 1.3. This plasma flows easily along magnetic field lines. Charged particles flowing along field lines can enter the atmosphere of the earth, contributing to the atmospheric region known as the ionosphere.

1.4 Ionosphere

The influx of charged particles into the atmosphere can alter the nature of the atmosphere itself. The upper atmosphere of the earth is itself partially ionized, by both magnetospheric particle flux and photoionization from the sun. This region of partially ionized atmosphere is called the ionosphere, and typically manifests at altitudes between 60 and 1000 km.

In the auroral latitudes, geomagnetic field lines connect magnetospheric current systems to the ionosphere. These "field-aligned currents" play a vital role in coupling energy between the ionosphere and the magnetosphere. The conductivity of the ionosphere allows electrical currents to flow, closing magnetospheric current circuits.

The electric currents that close in the ionosphere are linked with auroral structures. Figure 1.4 shows a generalized schematic of the various currents that exist in the pre-midnight auroral ionosphere. The figure is set looking westward, oriented along the north-south plane, at a high latitude such that the magnetic field is perpendicular to the surface. The vertical (field-aligned) currents transfer particles between the ionosphere and magnetosphere. Horizontal currents flowing mostly in the north-south plane (Pedersen currents) connect upward and downward field-aligned currents, and east-west (Hall) currents comprise the auroral electrojet.

1.5 Aurora

The aurora borealis forms in the high latitudes, concentrated in a ring known as the auroral oval encircling the magnetic north pole from 65 to 75° north invariant latitude, displaced to the nightside. The oval is a dynamic structure, changing in

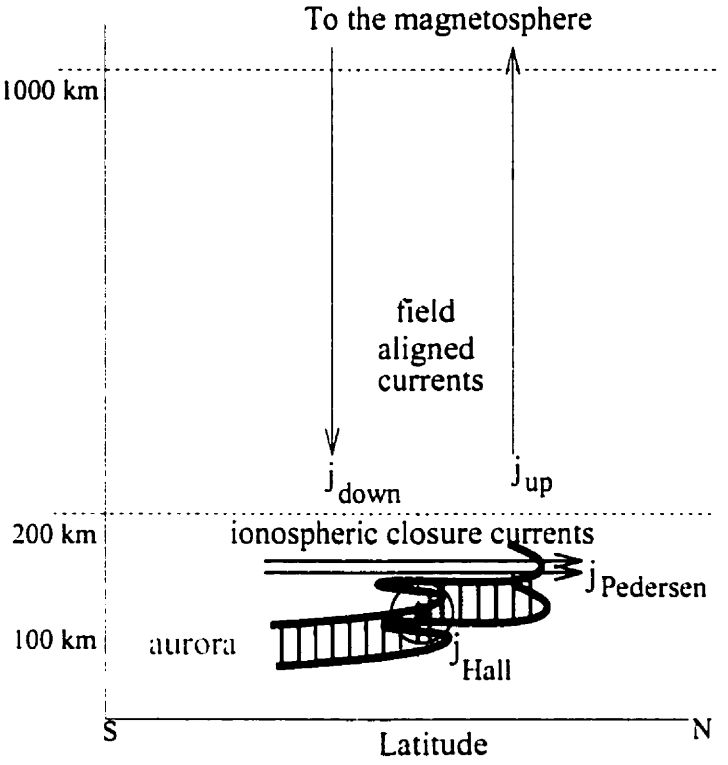

Figure 1.4: Currents flowing through the ionosphere

size in response to the conditions of the magnetosphere.

The energy released as aurora appears as sheets of light, sometimes extending from horizon to horizon. The most common wavelengths of light are caused by excitation of atomic oxygen, with the 557.7 nm (green) emission the most common, followed by the 630.0 nm (red) photon emission somewhat rarer [*Davis*, 1992]. There are many other emission wavelengths in the aurora, but these are either not in the visible spectrum, or are significantly weaker in intensity (or both).

Geomagnetic and optical activity associated with the aurora typically follows a pattern, known as a substorm. Substorms are brief (2-3 hour) magnetospheric distur-

bances that occur after the interplanetary magnetic field turns southward, allowing reconnection between geomagnetic and interplanetary field lines and enabling energy to be transferred from the solar wind to the magnetosphere. The storage of some of this energy in the Earth's magnetotail constitutes the first of the three phases of the substorm, the "growth" phase.

During the second phase, the substorm expansion phase, the energy stored in the tail is released when the field lines in the magnetosphere relax from their stretched, tail-like configuration and return to a more dipolar configuration. This phase is accompanied by a sudden and dramatic increase in auroral luminosity of the equatorward auroral arc [*Burke et al.*, 1985], the poleward propagation of this arc, as well as an increased intensity of the ionospheric current that runs parallel to the planet surface known as the auroral electrojet. This may be triggered by a northward turning of the IMF, but this is not a requirement for expansion.

The third phase is the recovery phase, during which the magnetosphere returns to its quiet state, as the energy in the magnetosphere returns to pre-substorm levels.

Analysis of auroral current structures provides information on how these currents transport energy between the magnetosphere and ionosphere. Comparing these currents to locations of particle precipitation and to auroral arcs will allow a greater understanding of how these phenomena are related.

1.6 Large Scale Current Systems

The aurora is an optical manifestation of the electrodynamic interactions between the ionosphere and the magnetosphere. A direct relationship between auroral structure

and field-aligned currents has been investigated in scores of experiments over the last forty years.

The field-aligned, or Birkeland, currents that flow between the ionosphere and magnetosphere are known to possess a statistical pattern over the auroral oval region. This large scale structure (figure 1.5) has been well documented since it was mapped with the TRIAD satellite mission [*Zmuda et al.*, 1966; *Ijima and Potemra*, 1976]. The distinctive shape of the distribution zones describe the statistical pattern of currents over scales of hundreds of kilometers.

These large-scale current systems are linked to the overall pattern of the oval, but the aurora often manifests as narrow structures with widths of 10's of kilometers down to hundreds of meters. Narrow (10's of km) regions of accelerated electron flux termed inverted V's have been detected by satellites since the early 70's (see the review by *Boyd* [1975]), and some of these have been matched with ground-based observations of auroral forms.

Spacecraft measurements of auroral currents show structures of scales similar to inverted-V scales, but also at smaller scales (see section 1.10). Later in this thesis, it will be shown that field-aligned currents can exhibit complex structures, including sub-structure, and even reversals of polarity, within inverted-V events.

1.7 Magnetic Field Detection

Aurorae often appear in ribbons or sheets that can extend from horizon to horizon. The currents related to the aurora are assumed to have similar structure. How these structures form and persist is something of a mystery. Analysis of current structure

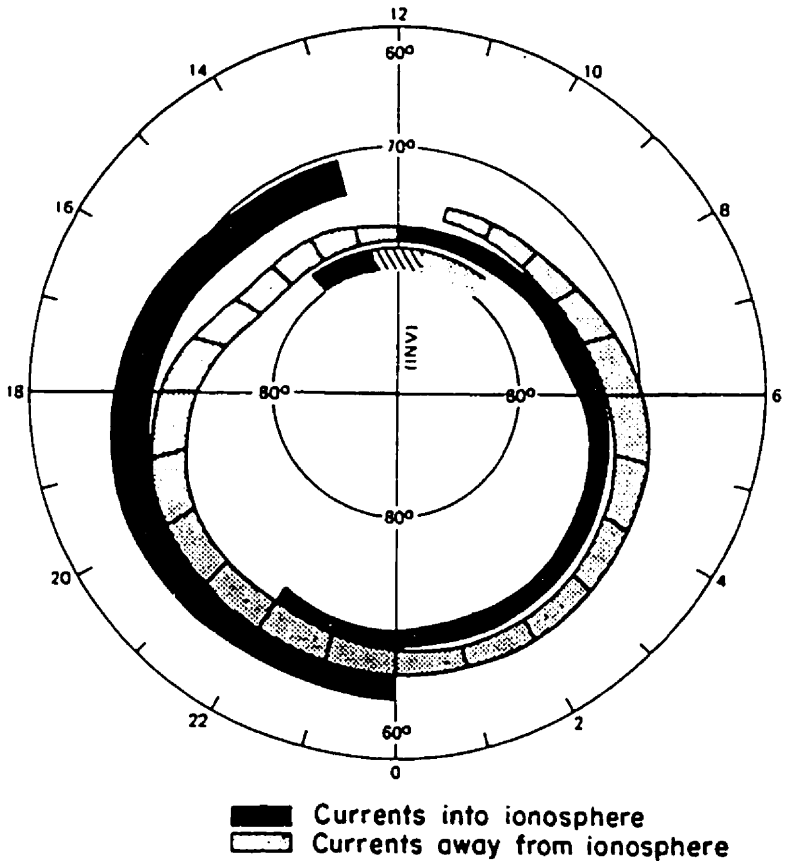

Figure 1.5: Birkeland current patterns over the auroral oval. After *Ijima and Potemra* [1976].

can provide information on the nature of the link between currents and these auroral forms. Direct (*in situ*) measurement of the currents and the related particles is possible, using instruments mounted on spacecraft that can enter these regions of electrical activity.

Ampere's Law can be used to determine the value of the current density $\vec{J}$ using measured values of the perturbation magnetic field ($\Delta\vec{B}$) generated by the current :

$$\nabla \times \Delta\vec{B} = \mu_o \vec{J} \tag{1.5}$$

Since measurement of curl requires more than one simultaneous measurement of the magnetic field, any single set of spacecraft-based magnetometers can only approximate the current density in the flight by the change in one component of the perturbation field perpendicular to the spacecraft trajectory. For example, a rocket payload traveling northward (x) and measuring the eastward (y) component of the perturbation field can be used to estimate the current flowing in the field-aligned (z) direction:

$$\frac{\partial(\Delta B_y)}{\partial x} = \mu_o j_z \tag{1.6}$$

This equation contains the assumption that the deviation in all other components are negligible compared to $\frac{\partial(\Delta B_y)}{\partial x}$. A current sheet flowing up or down the geomagnetic field, lying in a plane parallel to the geomagnetic field direction, and with the sheet oriented along the east-west direction, would produce a perturbation in the east-west (y) direction ΔB_y, with negligible deviations in the x and z directions. This is commonly referred to as the sheet current approximation, and is used extensively in magnetometer data analysis [*Primdahl*, 1971].

Figure 1.6 shows a conceptual diagram of a rocket payload flying northward through a pair of sheet currents aligned in the east-west plane. The currents are assumed to extend along the east-west direction for a large distance, but are not infinite. Beside this is a qualitative model of the eastward magnetic field trace as it could appear due to this configuration.

Field-aligned current sheet orientation need not be restricted to the east-west

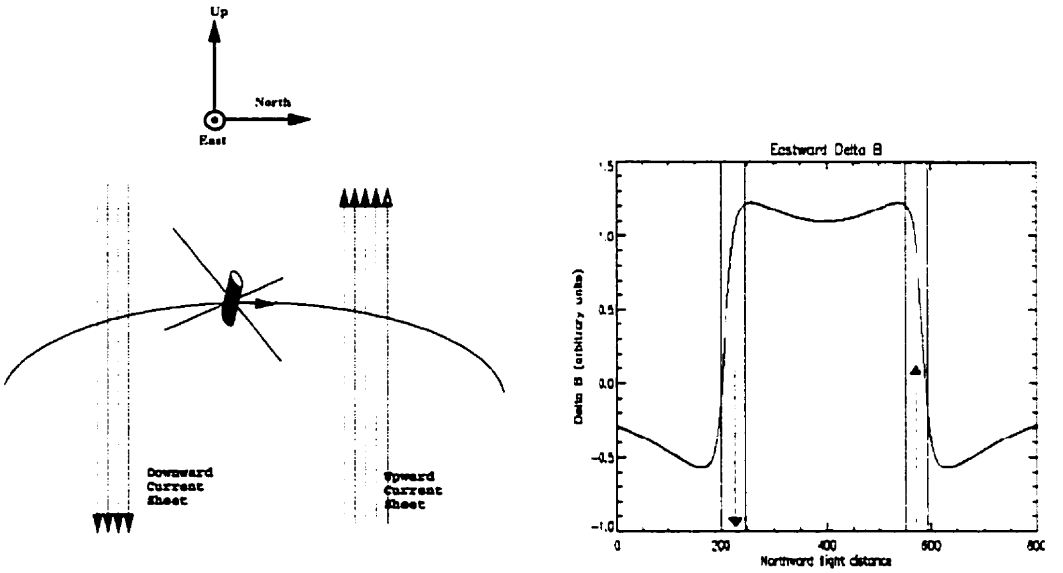

Figure 1.6: Sheet currents and the related magnetic trace, assuming currents extend nearly infinitely along the east-west plane.

vertical plane, and these structures may have some component in the north-south direction. The orientation of the sheet current with respect to the earth can be found by measuring the vector perturbation field along both the north-south (x) and east-west (y) directions. The resultant 2-dimensional $\Delta\vec{B}$ vector will be parallel to the current sheet, which then reveals the orientation of the current sheet itself. Such a vector field is discussed in more detail in chapter 4.

Field-aligned current signatures from magnetic perturbations can be compared to measurements of the charged particle flux in the region. Particle detectors are used to calculate the electric current, and show how the current carriers (electrons or ions) are distributed in energy. The higher energy particles can be detected easily, and have been measured as significant components of the circuit. However, particles

with energies below the threshold of detectors may be in great abundance, and could account for many results that show greater current densities implied by the magnetic perturbations than are determined by the particle detectors.

1.8 Ground-based Observations

In-situ measurements of auroral structures can be placed in context by examination of data collected by ground-based instruments that independently analyze attributes of the auroral ionosphere. These instruments also enable investigators to determine the real-time conditions before launching rocket-based experiments.

Ground-based magnetometer data from an array of stations scattered throughout the auroral zone can be used to form a large-scale picture of currents in the ionosphere. The auroral electrojet current produces a perturbation in the earth's magnetic field, which at the surface can have intensities of the order of hundreds of nT. As the pre-midnight electrojet flows eastward, the perturbation at ground level appears as a northward deviation of the magnetic field.

Meridian scanning photometers are optical sensors that scan the sky at a variety of wavelengths, showing the auroral emissions. By studying the optical auroral conditions during the flight, structures in the rocket data can be placed in a larger-scale context by comparing with the structure of the optical aurora.

Figure 1.7 shows a composite image from the Poker Flat, Alaska meridian scanning photometer. The photometer scans a narrow section of the night sky, with approximately 1 degree field of view, from the northern horizon to the southern horizon, along the magnetic meridian. One scan is completed every 16 seconds [*Mi-*

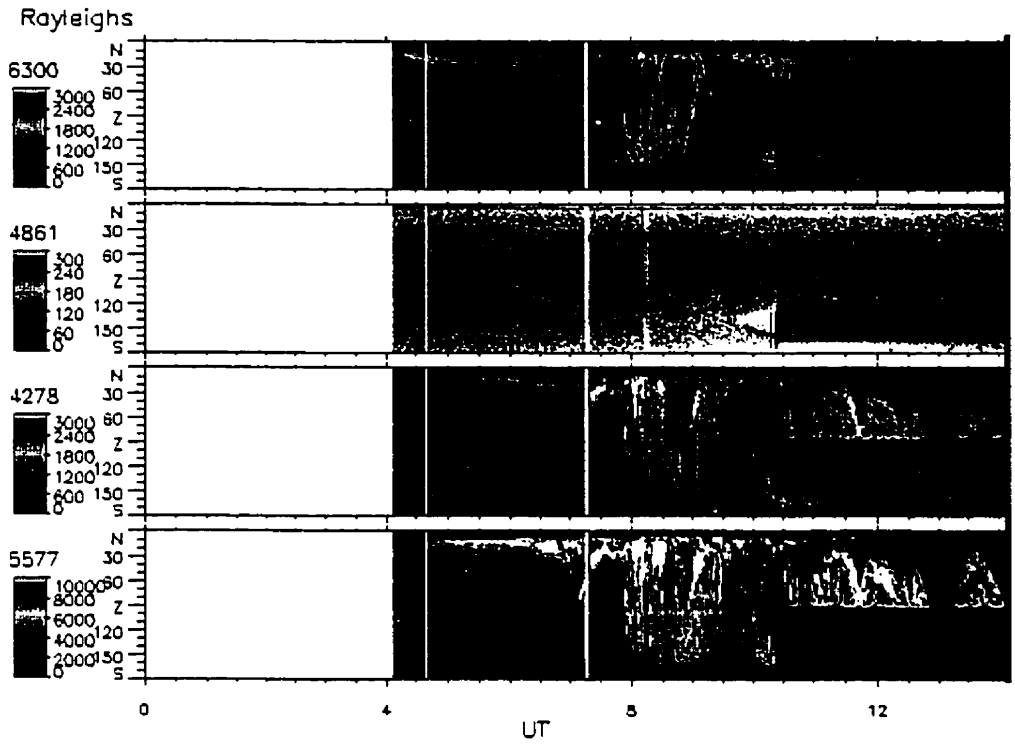

Figure 1.7: Keogram from Poker Flat, AK for Nov.7, 1995, including 630.0 nm, 486.1 nm, 427.8 nm, and 557.7 nm wavelengths. Highest intensities (in Rayleighs) appear white.

now, 1995]. The resultant image, known as a keogram, displays the auroral emission intensity at several wavelengths, each corresponding to an emission line common to aurorae. The scale for each image is different, corresponding to the spectral line intensity of the transition.

The cycle of a substorm can be observed in the behaviour of auroral emissions in figure 1.7. The wavelength providing the clearest structure and highest maximum intensity is 557.7 nm, and the image at this wavelength will be examined here . At

0700 UT, a slow southward progression of emission indicates the growth phase of a substorm. A rapid poleward motion 20 minutes later signals a weak substorm expansion, followed by a brief northward retreat at 0730 UT, signaling the recovery phase. Near 0800 UT a more intense expansion due to a second substorm develops, filling the sky over Poker Flat with auroral light.

The OEDIPUS-C rocket experiment, the subject of this thesis, was launched at 0638 UT, 2 hours after an earlier substorm. The onset of this substorm is shown clearly in ground-based magnetometer plots, described in chapter 2, and appears in the photometer plot as a weak structure. The apparent weakness is due to autoscaling of the intensity, as the substorm at 0800 UT produced much brighter aurorae than the 0430 substorm. Detailed analysis of the auroral structures encountered by OEDIPUS-C will be provided in chapter 4.

1.9 Measuring Electron Precipitation

Auroral arcs are caused by electron beams impinging on neutral atoms in the upper atmosphere between about 90-300 km (and sometimes above). Typically, these electron beams are organized into sheets which are extended in longitude, and which exhibit peaks in electron energy as a function of latitude. This rising/falling pattern in electron energy is illustrated in figure 1.8; it was given the name "inverted V" by *Frank and Ackerson* [1971].

The inverted V's in figure 1.8 were observed by the OEDIPUS-C rocket. They are typical in that electron energy reaches roughly 10 keV within the arcs and falls off roughly symmetrically northward and southward of the peak. The OEDIPUS-C

rocket traveled mostly northward, so that geographic latitude increases with time as displayed in the plot.

Rocket-borne electron detectors serve two purposes. First, they determine the location and morphology of inverted V's and other auroral structures (not all auroral electron precipitation follows an inverted-V pattern). Secondly, electron flux can provide an independent estimate of the electrical current strength in the vicinity of the spacecraft.

It is the purpose of this thesis to compare electron precipitation measurements with magnetic perturbations, in order to determine the structure of field-aligned currents and their relation to auroral arcs.

1.10 Literature Review

This section will describe a number of experiments that dealt with the study of auroral field-aligned currents. Some of the earliest studies are described in *Vondrak* [1970] and *Park and Cloutier* [1971]. These describe a rocket experiment that was flown through a quiet auroral arc in 1969. Magnetometers and particle detectors were used to determine the location, intensity and direction of field-aligned currents and relate them to regions of electron precipitation.

The particle detectors were capable of measuring electrons over an energy range of 2-18 keV and above 50 keV, and protons with energies of 2-18 keV and over 700 keV. The magnetometer used was an optically-pumped single-cell cesium vapor scalar device with a fixed bias coil. The total vector magnetic field was determined using this device and a lunar aspect sensor that recorded the attitude of the payload.

Using the magnetometer data, a model of the current sheets and electrojet were

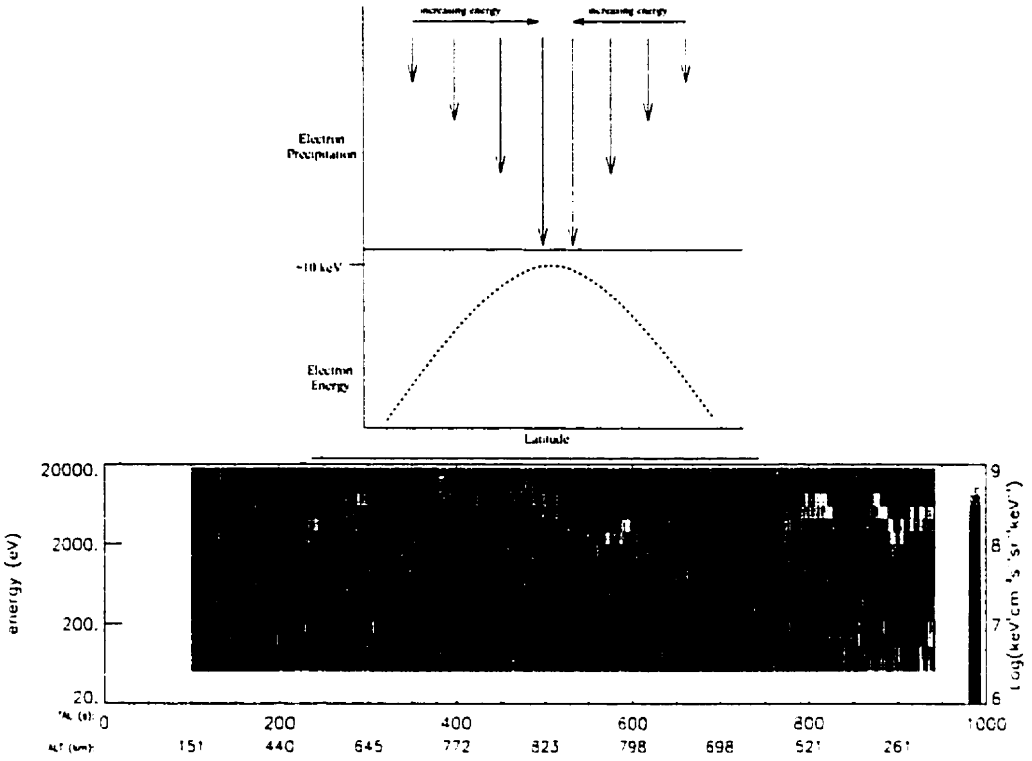

Figure 1.8: (Top) General structure of an inverted-V resulting from a local maximum in electron energy and energy flux (represented by vertical arrows). (Bottom) A series of inverted V's encountered by OEDIPUS-C. Details of this diagram will be discussed in chapter 4.

constructed. The model consisted of a set of adjacent, oppositely-directed, Birkeland current sheets with current strength of 0.16 amp/m and average current density of 5 μA/m^2 in magnitude, and a northwestward electrojet with a line current density of 6 $\times$ 10^3 amps. The two current sheets were both calculated to have widths of 16 km, and the electrojet was determined to be 15-25 km wide, at a mean altitude of 119 km.

The locations of maximum downward electron flux ($\sim$ 3 $\times$ 10^8/ster/cm^2/s/keV)

were correlated to the upward current sheet locations, which indicated that energetic (> 2 keV) electrons carry a substantial part of the upward Birkeland current. The location of the related downward current could not be identified, and no particles carrying this current were detected.

Two sets of all-sky camera were used to determine the position of the auroral arc that the rocket flew through. Sections of the arc that allowed triangulation were within 100-120 $\pm$ 15 km altitude and the remainder was assumed to be at 110 km. The horizontal location of the arc was determined to within 1 km, using similar methods as the altitude determination. The arc width in the horizontal plane was found to be about 7 km, and electron fluxes were found to occur near the center of this arc and as well as near the north edge. No significant fluxes were observed outside the arc.

Data from the Ogo-4 satellite was presented in *Berko et al.* [1975]. This satellite contained 8 particle detectors and 3 search-coil magnetometers. Four of the particle detectors were arranged to point radially away from the earth, and measured energies of 0.7, 2.3, 7.3, and 23.8 keV, respectively.

The results from this experiment were collected over many satellite passes. Statistical comparisons were made of locations of field-aligned electron precipitation and magnetic field indications of field-aligned currents. From these comparisons, it was found that there were a large number of events where electron precipitation coincided with upward field-aligned current events. Maximum current densities of 50 $\mu A/m^2$ were recorded.

Results from the ISIS-2 satellite are presented in *Klumpar et al.* [1976]. This paper presents simultaneous magnetic field signatures of field-aligned currents with

charged particle measurements. ISIS-2 instruments included a Soft Particle Spectrometer (SPS) which detected ions and electrons over energy ranges of 5 eV to 15 keV. Pitch angle coverage was accomplished by placing the detector in the spin plane of the satellite, enabling a full 360° sweep to be performed over every spin period (18 seconds). A three-axis magnetometer was used for both attitude analysis and for detection of currents. Sections of the magnetometer analysis in this thesis is based on concepts explained in the *Klumpar et al.* [1976] paper.

Analysis of several post-midnight passes of the ISIS-2 satellite allowed several conclusions to be made. Magnetic field deviations were often accompanied by changes in the low-energy (< 1 keV) electron flux. Positive ions in the energy range of the SPS carried less than 10 percent, and often less than 1 percent of the current carried by electrons in the same energy range. Insufficient electron flux to carry downward currents determined by magnetic deviation was seen in some cases, suggesting low-energy ionospheric electrons carry a significant portion of these currents. In some cases, magnetic perturbations suggested finer-scale current structures than indicated by the particle flux.

A later paper by *Klumpar and Heikkila* [1982] on data from the same satellite found evidence of intense bursts of low energy (tens to hundreds of eV) electrons streaming out of the ionosphere along magnetic field lines. These bursts were highly constrained along the field lines, with pitch angles within 10° of anti-parallel to the magnetic field. The paper suggests that these electrons are responsible for downward currents, which have been notoriously difficult to measure. The acceleration of the ionospheric electrons is thought to be caused by a downward electric field located in the lower ionosphere.

Observations recorded in *Theile and Wilhelm* [1980] show comparable upward current densities from electron precipitation and magnetic field variations. Electrons were measured with energy ranges of 15 eV to 35 keV. Downward currents were not seen in the electron data, leading to the familiar conclusion that low-energy ionospheric electrons are carriers of this current.

The CENTAUR I experiment, discussed in *Primdahl and Marklund* [1986] and *Marklund et al.* [1986], was a sounding rocket flight into the dayside polar cusp region. The payload was equipped with three-axis fluxgate magnetometers mounted on a telescoping boom. Electric fields were also measured, using a double-probe instrument. One region of eastward magnetic perturbation (implying an upward flowing current) was matched to a region of a northward electric field, suggesting a uniform height-integrated conductivity existed in this region.

Recent findings have utilized improvements in technology to increase the precision of measurements in space. *Carlson et al.* [1998] and *Elphic et al.* [1998] describe results from the FAST satellite. FAST contained a wide range of state-of-the-art instruments, including 16 "top-hat" electrostatic analyzers, each with a 180° field-of-view. These instruments collected electrons with energies of 4 eV to 30 keV and ions with energies between 3 eV and 25 keV. Pitch-angle coverage spanned 360°. Both fluxgate and search-coil magnetometers were mounted on the satellite, both on booms to reduce effects due to stray fields on the spacecraft. Other instruments on FAST included electric field detectors and ion mass spectrometers.

Analysis of field-aligned currents and inverted V's by FAST found that downward currents were found near the edges of inverted V's. These currents were carried by low- to medium-energy electron beams from the ionosphere, with energies up to

several keV. Locations of downward currents were commonly found in regions where little or no downward electron flux existed, as expected. This finding will be discussed later in the analysis of the OEDIPUS-C data.

Chapter 2

Experiment

This chapter will discuss the launch and flight details of the OEDIPUS-C experiment. Included will be a description of the payload, a breakdown of the flight, a review of the auroral conditions during the mission, and a list of the instruments that provided the data for the remainder of this thesis.

2.1 OEDIPUS-C

The **OEDIPUS** (**O**bservations of the **E**lectric field **D**istributions in the **I**onospheric **P**lasma - a **U**nique **S**trategy) program was begun to investigate the nature of tethered systems in space, as well as to make available platforms for upper atmosphere auroral research.

The instruments on board OEDIPUS-C relevant to this thesis include fluxgate magnetometers, electrostatic analyzers for detection of electron energy flux, and a high-frequency transmitter/receiver experiment that provided information on the local electron density.

2.2 Flight Details

OEDIPUS-C was launched from Poker Flat, Alaska on 06:38:17.2 UT, November 7, 1995 using a Bristol Aerospace Black Brant XII rocket. The principal investigator for this mission was Dr. H. G. James of the Communications Research Center in

Figure 2.1: OEDIPUS-C decal

Ottawa, Ontario. The OEDIPUS-C payload consisted of two sub-payloads which separated in flight, but remained connected by a conducting tether. The bi-static configuration was used for RF propagation experiments not related to this thesis. Each sub-payload had identical experiments to probe auroral particles and fields. The information in this thesis is restricted to the forward sub-payload experiments.

Once the rocket motors separated from the payloads, an attitude control system aligned the payloads to within 0.5 degrees of the local magnetic field. This alignment was necessary for the proper operation of the scientific instruments on board. The spin rate of 3.75 Hz was reduced to 0.084 Hz with the deployment of the booms on the two sub-payloads. The forward payload booms extended 19 metres tip-to-tip,

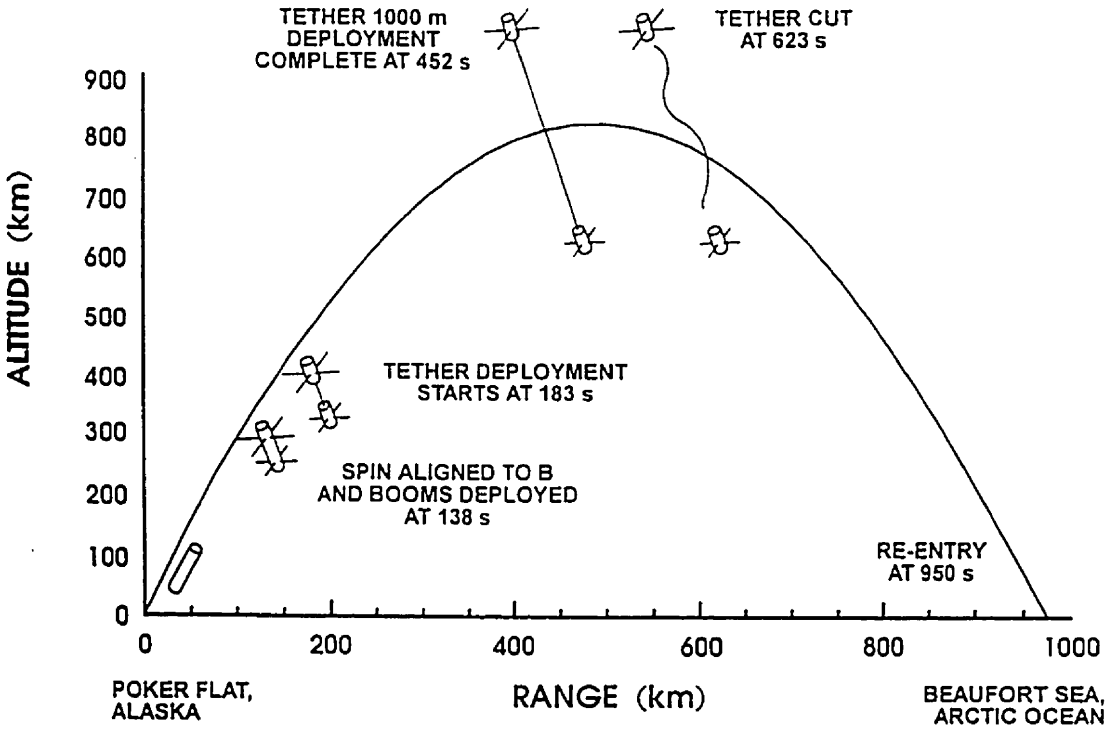

Figure 2.2: Rocket flight path

and the aft booms were 13 metres tip-to-tip. The booms acted as dipole antennas for plasma physics experiments, and were also used as stabilizers for the payloads, controlling the dynamics of the spinning vehicles.

After boom deployment, the two sub-payloads separated, allowing the tether to unwind to 1174 metres. The tether was severed at apogee, 623 seconds after launch at an altitude of 824 km, allowing the payloads to operate in electrical isolation for the remainder of the flight. Re-entry occurred 957 seconds after launch, and the payloads eventually impacted in the Beaufort Sea.

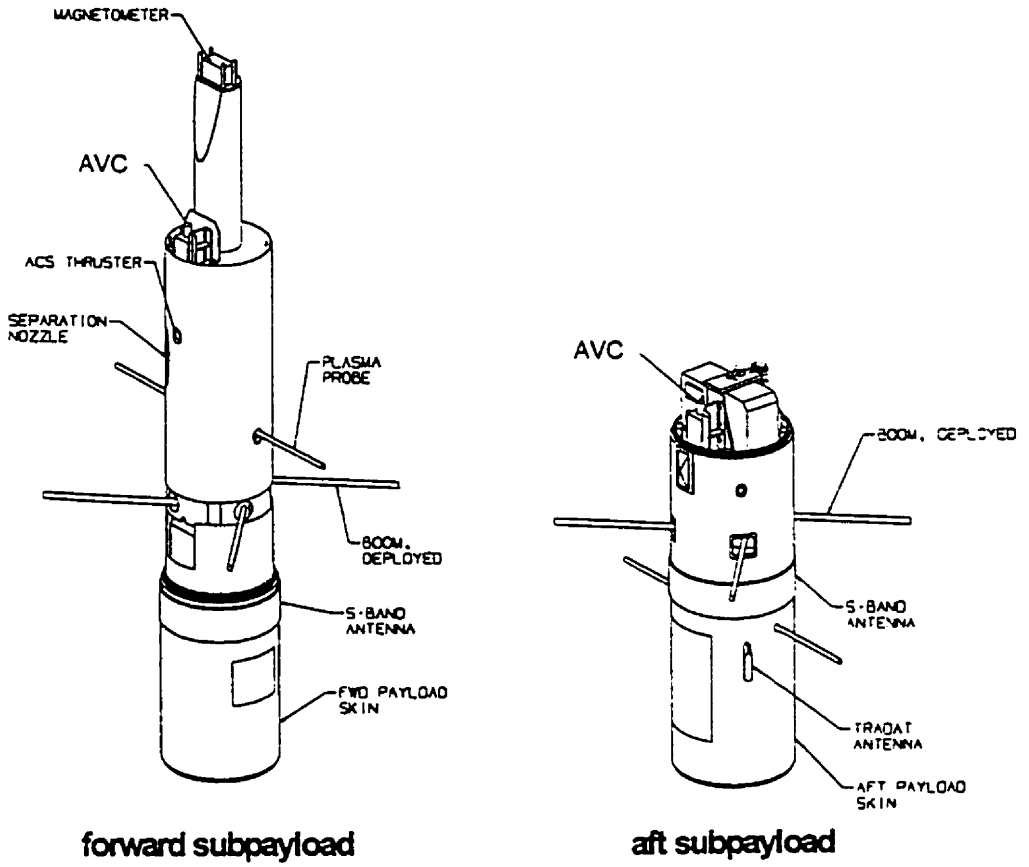

Figure 2.3: Configuration of OEDIPUS-C payloads

The flight is shown schematically in figure 2.2. The configuration of the payloads is shown in figure 2.3. Information from the aft payload was not included in this study, as the aft magnetometers returned unreliable data for a significant portion of the flight.

2.3 Instrument Details

Mounted on the nose of each payload, the three-axis fluxgate magnetometers were used to determine the perturbations in the local geomagnetic field, as well as to aid in determining payload attitude for the flight. The magnetometers operated with a sampling rate of 854.16 Hz, capable of measuring magnetic field strengths up to 65536 nT at a resolution of 7 nT. The operational principles of fluxgate magnetometers are discussed in appendix A. The magnetometers were provided by Dr. D. Wallis of the Herzberg Institute of Astrophysics.

The electron detectors on board were placed in the payload body, with openings in the payload skin for the detector entrance apertures. Two electron detectors were aboard, with fixed apertures oriented at 45° and 90° to the payload axis. These electrostatic analyzers were capable of determining the flux for electrons ranging in energy from 50 eV to 18000 eV, with fluxes up to 10^9 keVcm^{-2}ster^{-1}s^{-1}keV^{-1} . Appendix B contains further information on the electron detectors used in this experiment.

A bi-static high frequency experiment for measuring electron densities and wave propagation modes in the ionosphere, denoted HEX/REX, was also on board. Electron densities and other parameters were calculated using this instrument [*James and Calvert*, 1998].

The attitude of the payloads during flight was determined using a video camera system. Information on the position and direction of the payload was used in the magnetometer analysis. This is discussed in detail in chapter 3.

2.4 Conditions

The auroral conditions during the flight are described using ground-based instruments that measured the optical properties and the magnetic perturbations from the auroral structures as they progressed the evening of the flight.

2.4.1 Optical Conditions

Figure 2.4 is a keogram produced from a meridian scanning photometer at the Poker Flat Rocket Range in Alaska.

The 557.7 nm wavelength is produced in atomic oxygen, with the transition of an electron from the second to the first excited state [*Davis*, 1992]. This is the most dominant emission line in the aurora.

This particular image displays the view from the northern horizon to directly overhead Poker Flat. The false color image represents auroral intensities, marked on the right from 1000 to 12000 Rayleighs. A Rayleigh is a unit of photon flux, and is equivalent to $10^6 h\nu cm^{-2} ster^{-1} s^{-1}$, with ν the frequency of the photons measured.

Auroral emission typically occurs above $\sim$ 100 km altitude. Therefore, an estimate of the distance the aurora is from the photometer can be made, via:

$$x = \frac{100}{\tan\theta} \tag{2.1}$$

where x is the distance (in km) along the surface from the photometer station to the auroral arc, projected from the 100 km emission height, with θ the measured angle from the horizon.

As figure 2.4 shows, the most intense emissions measured at Poker Flat occurred between 5 and 30 degrees from the northern horizon. This corresponds to distances

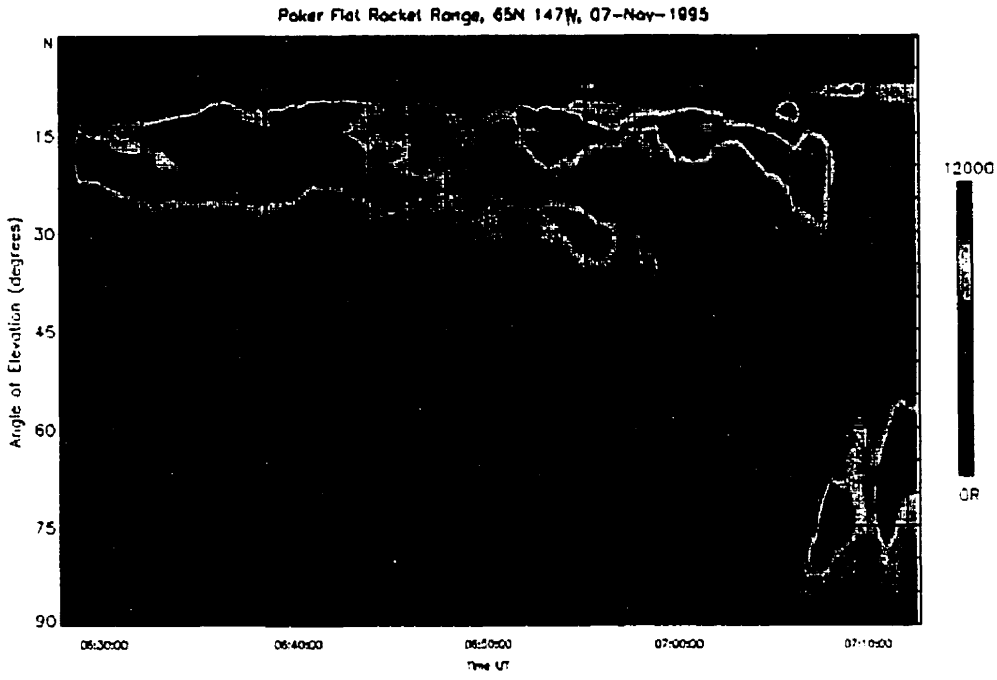

Figure 2.4: Keogram from Poker Flat, Alaska, showing the auroral conditions during the flight of OEDIPUS-C (Courtesy Roger Smith, [personal communication]). The image displays the northern half of the sky above Poker Flat. The red bars indicate the section of the plot coincident with the flight time of OEDIPUS-C. The false color image represents photon intensity in units of Rayleighs.

north of Poker Flat between 1100 and 175 km respectively.

The emissions shown in figure 2.4 represent a band of quasi-stable auroral arcs following a substorm initiated at 0430 UT. A second, more intense substorm followed at 0800 UT. Therefore, OEDIPUS-C flew through an arc system sustained through substorm recovery and growth phases.

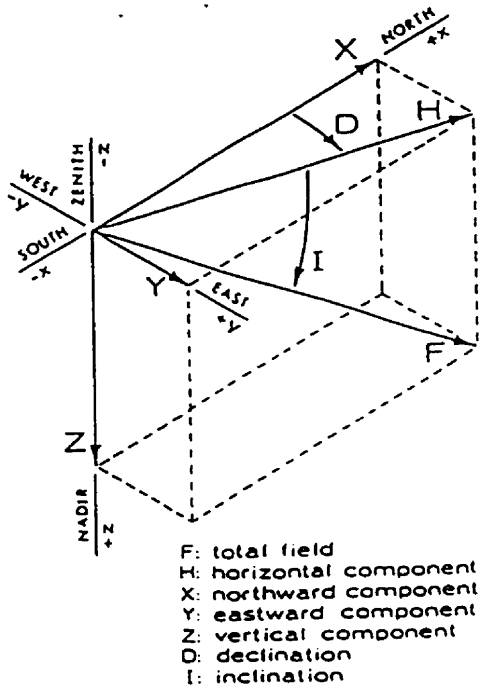

Figure 2.5: Coordinates used in ground-based magnetometers

2.4.2 Magnetometer Array Data

Auroral activity is accompanied by disturbances of the geomagnetic field, caused by currents in the ionosphere. Arrays of magnetometers at various locations under the auroral oval can record the development of magnetic field perturbations caused by auroral activity.

The intensity of the total field (figure 2.5) is described by the magnetic elements, which include the vertical component (Z), the horizontal component ($\vec{H}$), and the declination (D) [*Knecht and Shuman*, 1985]. The $\vec{H}$ component can be divided into north (X) and east (Y) components, as declination is the angle measured eastward between magnetic north and true north. D is considered positive when the angle measured is east of true north and negative when west. Plots can also show the total

magnitude of the field ($|\vec{F}|$), and the inclination (I), the angle between $\vec{H}$ and $\vec{F}$.

Perturbations in any or all of these components can signal electrodynamic activity in the ionosphere, such as a substorm.

The following figures are plots of the magnetic field components during the substorms of the evening of Nov. 7, 1995. The magnetometer arrays shown in the following diagrams are from the CANOPUS (Canadian Auroral Network for the OPEN Program Unified Study) project and the University of Alaska GIMA (Geophysical Institute Magnetometer Array) program.

Magnetometer data is shown in figures 2.6 (CANOPUS array), and figures 2.7 and 2.8 (GIMA sites). Following this (figure 2.9) is a map showing the locations of the magnetometer sites. Superimposed on this map is the projection of the flight path of OEDIPUS-C onto the surface of the earth.

CANOPUS magnetometers at Rankin Inlet observed a substorm onset at 0437 UT. Contwoyto Lake magnetometers show onset at 0441 UT, delayed from the Rankin site, indicating a westward surge. The deflection in the D-component of the Gakona station at 0445 UT is further evidence of this substorm.

The launch of OEDIPUS-C attempted to take advantage of auroral conditions that were related to this substorm. Limited launch window times forced the launch to be delayed until after 0630 UT, so that the onset phase had already passed.

The stable system of arcs seen in figure 2.4 produce no obvious or significant ground magnetic perturbations, indicating that, at best, a moderate strength auroral current system was associated with these arcs. A single magnetometer station north of the launch site of Poker Flat was recording that evening (Ft. Yukon). The fact that the arc system seen in figure 2.4 is generally northward of even the Ft. Yukon

station limits our ability to estimate the true strength of the associated auroral electrojet current.

The magnetometers show a return to prestorm levels by 0730 UT. indicating recovery had occurred. The larger substorm at 0800 UT is also recorded on both GIMA and CANOPUS magnetometers.

CANOPUS data is courtesy the Canadian Space Agency and the GIMA magnetometer data is courtesy the Geophysical Institute, University of Alaska Fairbanks and the United States Geological Survey.

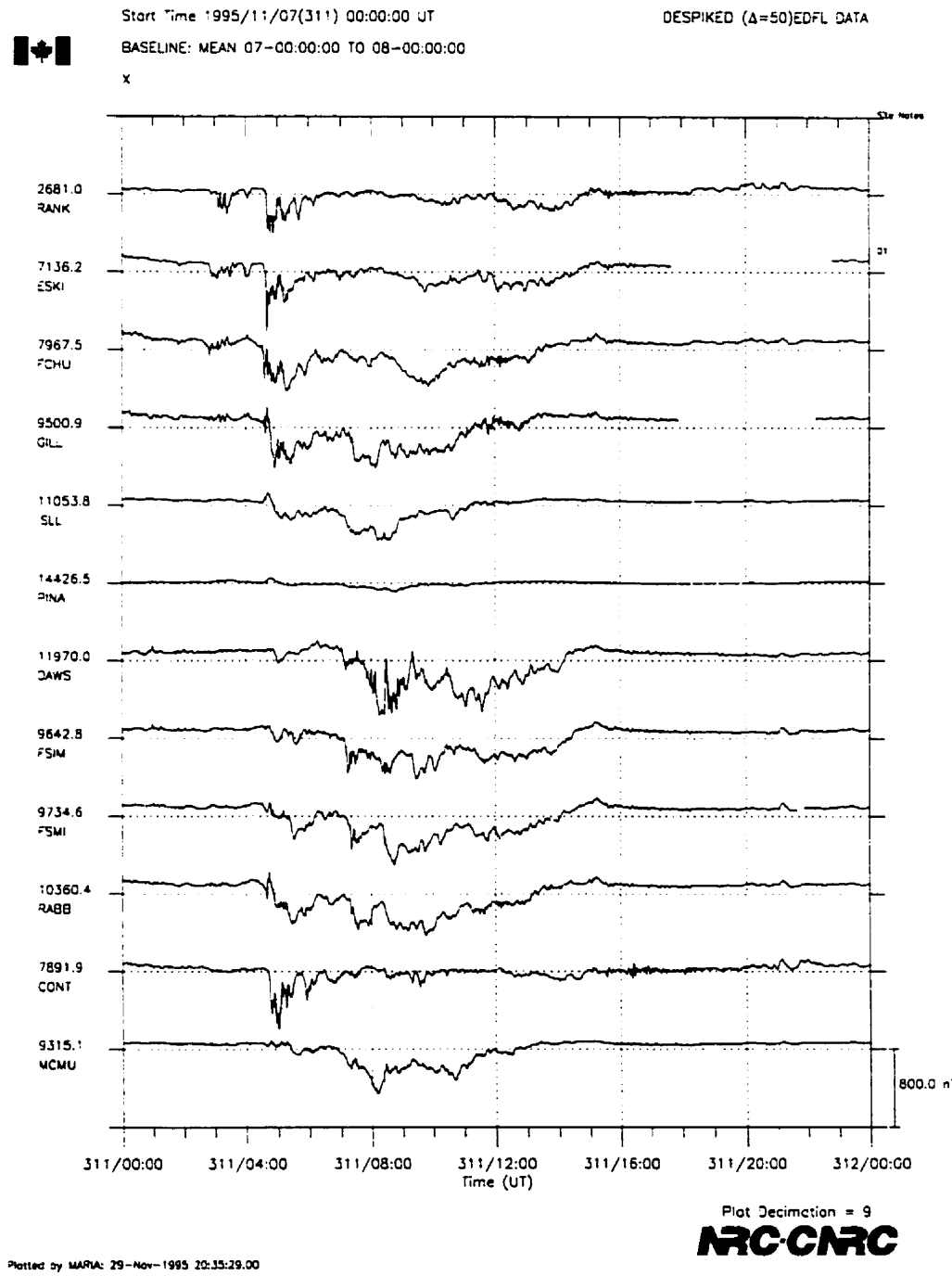

Figure 2.6: Northward (X) geomagnetic field component, CANOPUS Magnetometer Array, November 7, 1995.

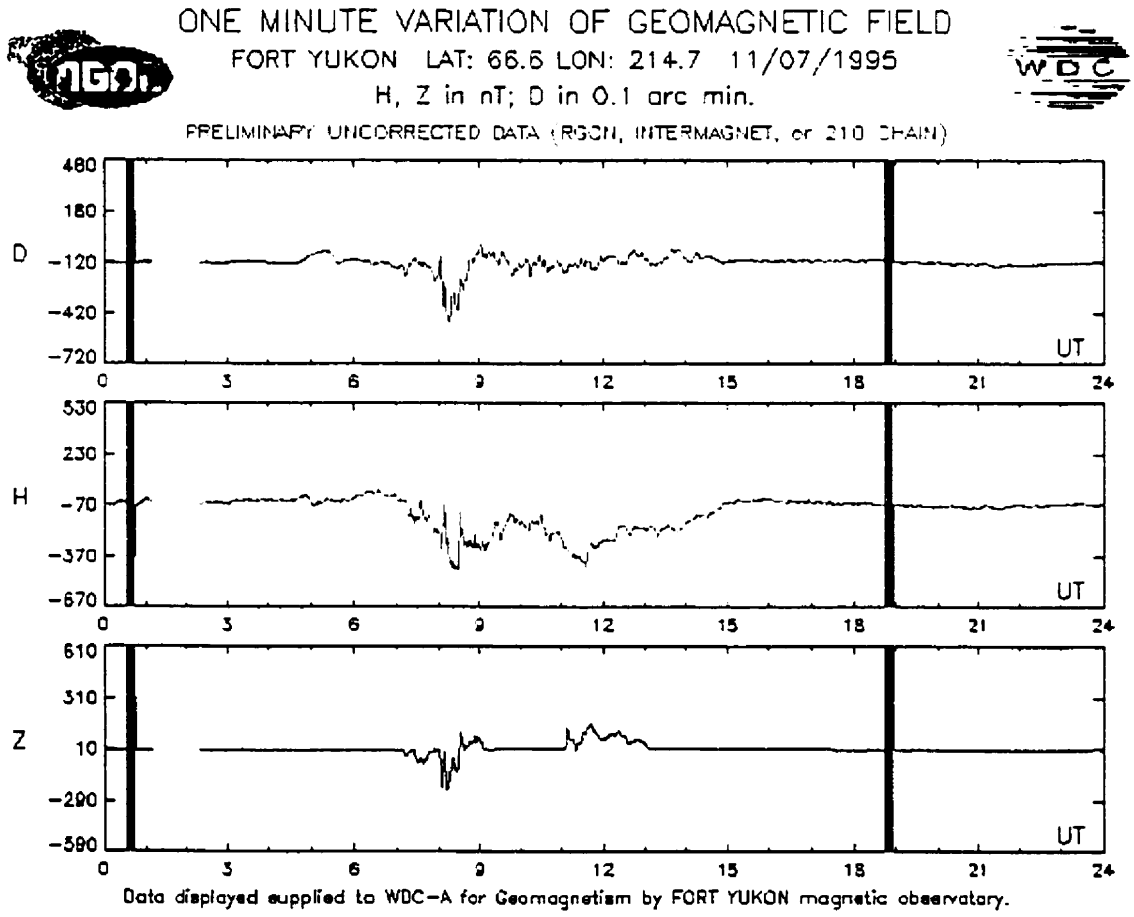

Figure 2.7: Ft. Yukon magnetometer data for Nov. 7, 1995. Vertical lines before 0100 and 1900 and data gap between 0100 and 0200 are errors caused by resetting the magnetometers.

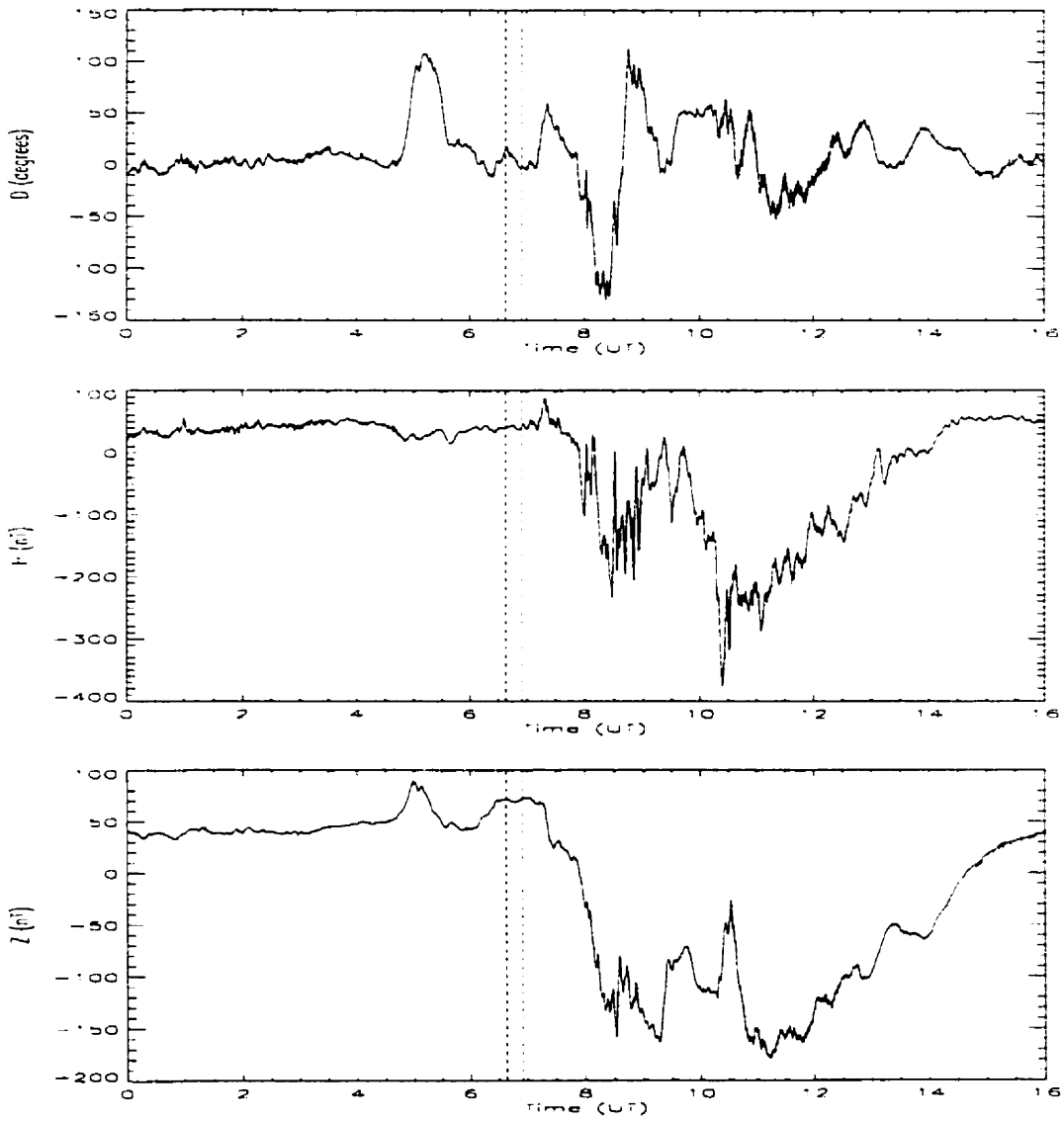

Figure 2.8: Magnetic elements of Gakona station. Dotted lines indicate flight time of OEDIPUS-C.

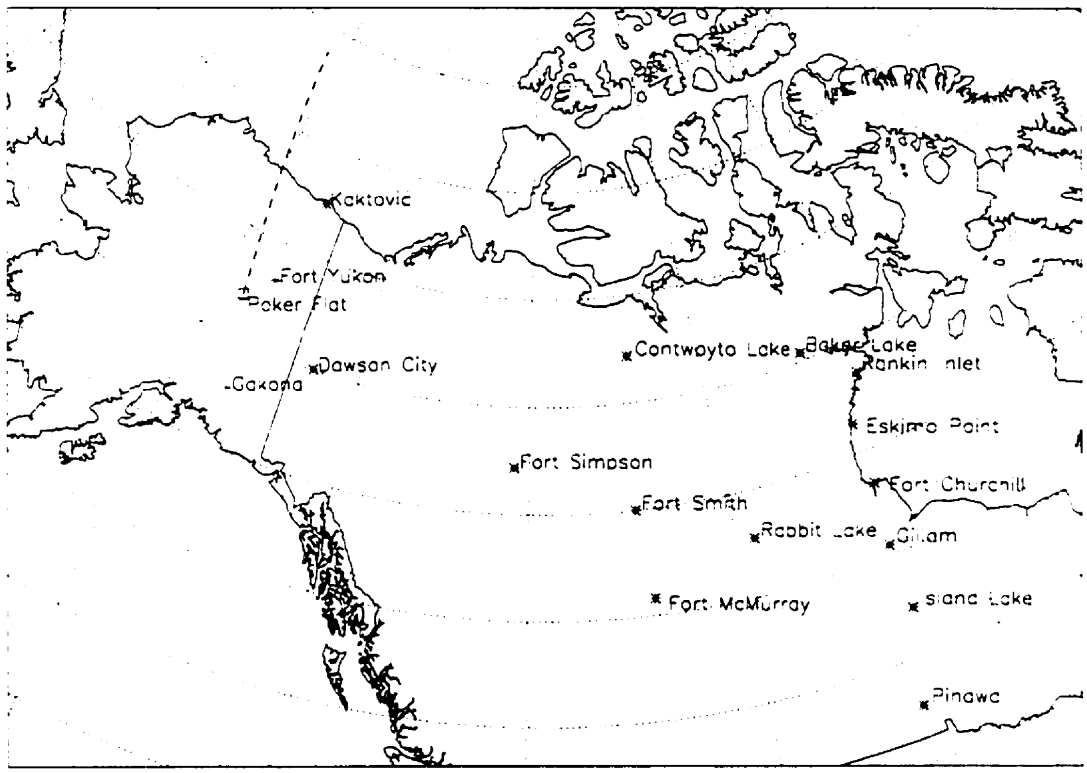

Figure 2.9: Map showing CANOPUS (*) and GIMA (+) magnetometer locations in North America. Dashed line is the ground projection of the OEDIPUS-C flight path.

Chapter 3

Attitude and Data Analysis

3.1 Introduction

This chapter will describe the steps taken to analyze the data from the OEDIPUS-C instruments. Analysis of magnetic field data requires accurate payload attitude information. In this experiment knowledge of the magnetic field was required to have an accuracy of greater than one part in ten thousand, in order to detect variations in the background geomagnetic field caused by field-aligned currents.

The process used to determine the position and orientation of the payload will be described in this chapter. This information is used to determine the magnetic field perturbations that existed along the flight path of the OEDIPUS-C payload.

3.2 Payload Attitude

A sounding rocket payload is typically stabilized by imparting a spin to it. Once the payload is "spun-up", booms are deployed, slowing the spin rate by conservation of angular momentum. As the craft proceeds, the spin keeps the orientation of the payload as constant and stable as possible.

For OEDIPUS-C, the payload stabilization method was successful, with the orientation kept within a few degrees of its intended direction, aligned with the geomagnetic field.

Before explaining the details of the attitude analysis, some explanation of the physical constraints will be discussed.

A spinning symmetric body can be analyzed by understanding the nature of the constants of motion associated with it. The motion of such a body can be described as a combination of the spin about the axis of symmetry and the precession of that axis about the total angular momentum vector $\vec{\mathbf{L}}$, which is a conserved quantity over the unpowered portion of the flight. As the body progresses, the motion of the body axis about $\vec{\mathbf{L}}$ traces out a cone in space (Figure 3.1). Therefore, the angle between $\vec{\mathbf{L}}$ and the payload symmetry axis is known as the coning angle. In the case of a torque-free symmetric body, the coning angle is a constant of motion [*Goldstein*, 1950]. However, if the body is not axisymmetric, the coning angle will vary in time, producing periodic variations known as nutation.

In figure 3.1, the motion due to a symmetric coning body is shown, along with a body undergoing nutation due to its asymmetric structure. At the top of the first figure, a symmetric body is shown as it precesses about $\vec{\mathbf{L}}$. The coning angle ξ_1 is constant. If the spin axis of the payload is projected onto the plane perpendicular to $\vec{\mathbf{L}}$ the coning motion will trace out a circle in this plane. The plot next to the first figure shows the y-component of this motion ($y = \sin\theta$).

The second plot in figure 3.1 shows the asymmetric body, with the coning angle varying from ξ_1 to ξ_2 over time. As the payload nutates, the coning angle changes periodically. The plot of the y-component of the coning circle now displays the alternating coning radius as a function of time.

The OEDIPUS-C payload underwent spin balancing before flight to minimize nutation. However, finite nutation during the flight indicates that the balance was

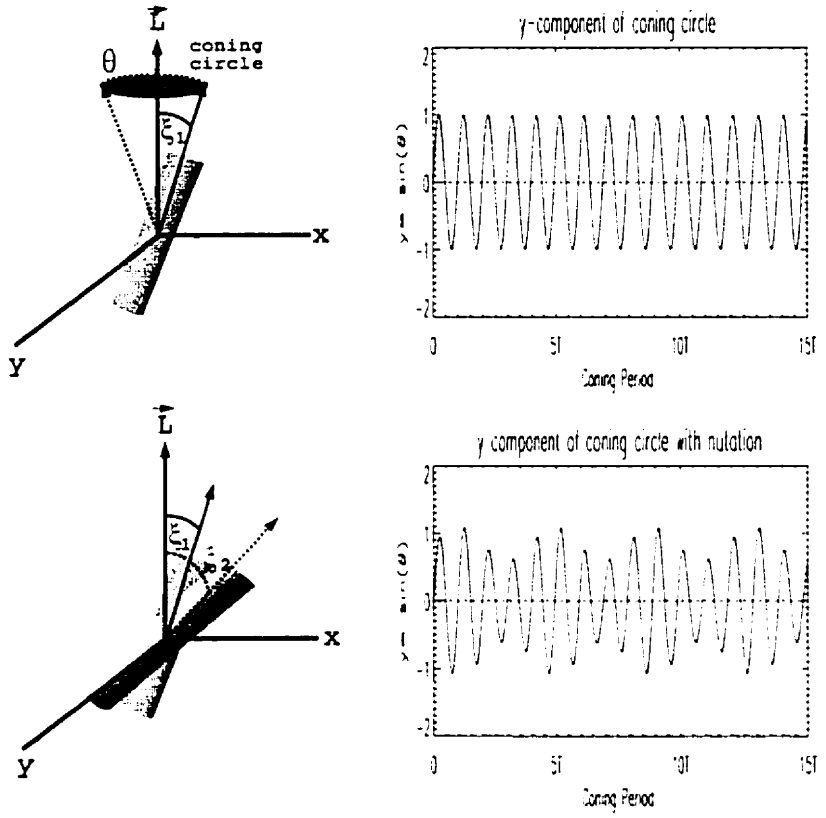

Figure 3.1: Coning and nutation examples

not perfect. Other effects on payload motion include boom flexing, which induced vibrations with frequencies on the order of 1 Hz. The booms also applied a damping force to the payload motion, which may have contributed to variation in the coning angle.

Analysis of the attitude of the OEDIPUS-C payload in terms of spin, coning and nutation was performed in detail by Tyc [1998]. The spin frequency was 0.087 Hz, the coning frequency was 0.110 Hz and the nutation frequency was 0.032 Hz.

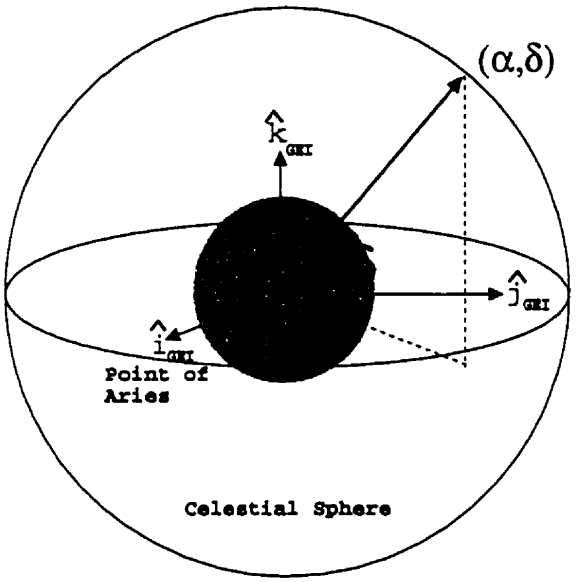

Figure 3.2: Celestial coordinate system. α = Right Ascension, δ = Declination. The Cartesian representation is the Geocentric Equatorial Inertial system.

3.3 OEDIPUS-C Attitude Analysis

The OEDIPUS-C attitude was determined using a video camera system (AVC). A camera was mounted on the front of each sub-payload, and imaged the star field ahead of the rocket. The images from the cameras were analyzed by Bristol Aerospace (the payload contractor) to identify the brightest stars in each frame, which allowed the orientation of the payload symmetry axis to be determined. This information was recorded in celestial coordinates (figure 3.2). The analysis produced attitude information at a data rate of 2 Hz for the forward payload, accurate to 0.25° (2σ).

In the case of the OEDIPUS-C forward payload, precautions to limit extraneous

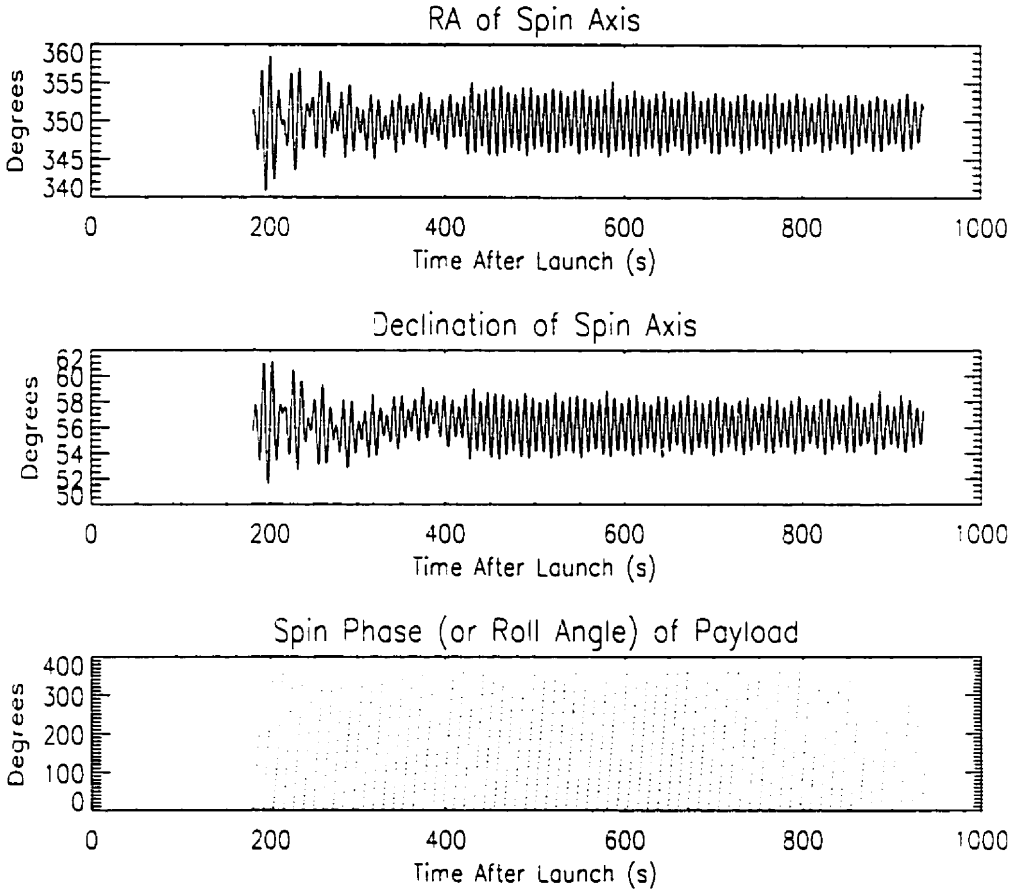

Figure 3.3: Attitude data from AVC camera

motion were not completely successful. During the flight there was definite nutation of the payload. After a period of roughly 200 s of rapid oscillation of the coning angle, the motion settled to a nearly uniform nutation rate with the coning angle varying between 2.5 degrees at minimum to nearly 4 degrees at maximum, with a period of 33 s.

The pointing direction of the long axis of the payload is shown in figure 3.3 in terms of celestial coordinates, Right Ascension (RA) and Declination.

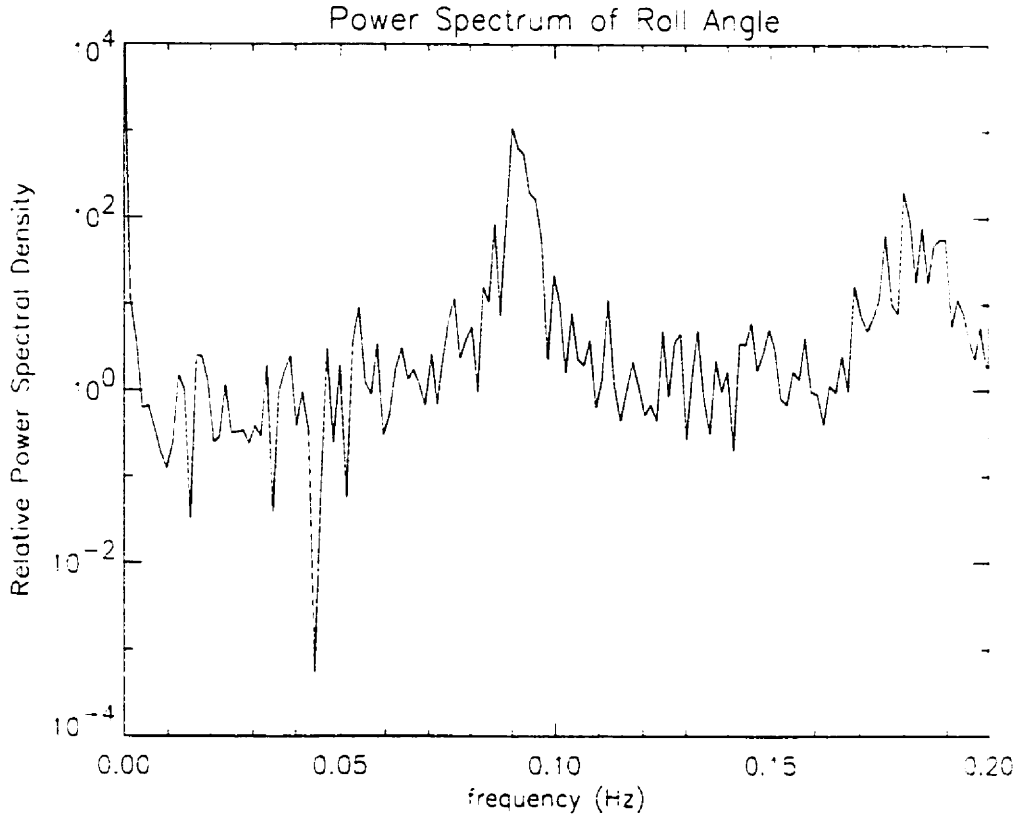

Figure 3.4: Power spectrum of the roll angle data

The celestial coordinate system is a spherical coordinate system where α is the angle in the equatorial plane measured eastward from the first point of Aries (figure 3.2), and δ the angle measured with respect to the celestial equator (the x-y plane). The Cartesian description of this celestial system is known as the Geocentric Equatorial Inertial (GEI) system.

The roll angle (ρ) data is defined as the angle between the projection of the Vehicle Data Axis (VDA) of the payload into the horizontal plane, and a vector pointing from the payload to geographic north. The VDA is a reference axis perpendicular

to the spin axis of the payload, fixed to the payload. The record of the roll angle is shown as the third plot in figure 3.3. For a payload spinning with constant frequency ω, the roll angle is given by:

$$\rho(t) = \omega(t - t_o) \tag{3.1}$$

where the frequency of the payload spin is ω, and t_o is a reference time when the VDA points northward.

Calculation of the average spin frequency $\omega = 0.089$ Hz is performed by taking the Fourier transform of the sine of $\rho(t)$ and plotting the power spectral density (figure 3.4). This result is similar to the value calculated by *Tyc* [1998] of 0.087 Hz. The spin rate was not exactly constant, as it varied somewhat due to the nutation of the payload.

Figure 3.5 shows the pointing direction of the payload spin axis in celestial coordinates, as recorded by the attitude video camera. The circle traced out by the coning payload is shown to vary, producing the circles of various radii in the figure. As the coning period was roughly 8.5 s, the camera sample rate of two frames per second produced only 17 frames per coning period, on average. The erratic nature of the plot in figure 3.5 is a result of this low sample rate.

Analysis of data from magnetometers requires accurate attitude information. For OEDIPUS-C the background magnetic field was of the order of 5×10^4 nT, and expected perturbations were of the order 10 nT. This translates to an angular deviation of roughly 0.05°. Since the raw attitude data was accurate to only 0.25°, it was not sufficient to resolve these perturbations directly.

Therefore, a method was needed to reduce the noise in the attitude data such that the accuracy was sufficient to detect the expected perturbations. This was done

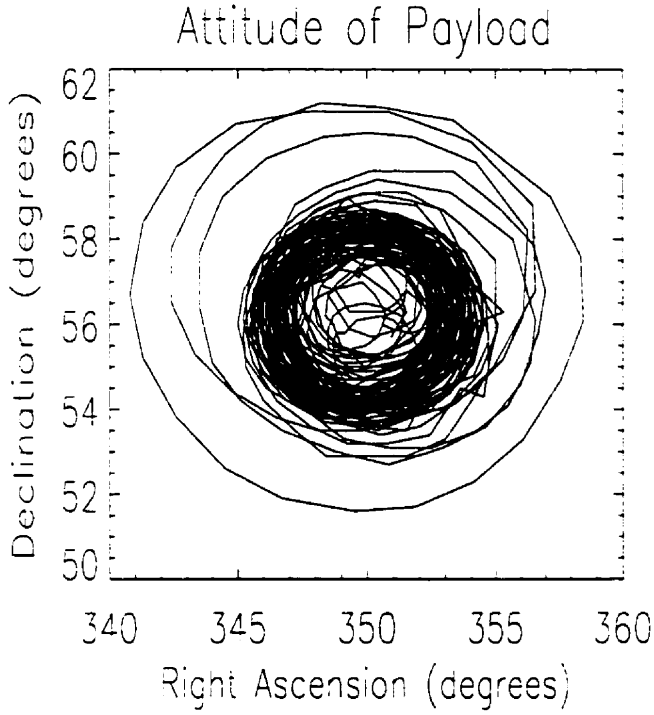

Figure 3.5: Plot of camera attitude (in degrees), showing the nutation of the payload as the variation in the radius of the coning angle.

by assuming that the actual motion of the spacecraft was periodic and smoothly varying in time, and that the data points from the camera data could be smoothed to reduce random errors.

Filtering was used to reduce noise associated with attitude determination errors. The filter passed frequencies of 0.5 Hz and below. The data were then interpolated using a spline. This spline routine fits a cubic polynomial curve between individual points, and interpolates from the original 2 points per second to 32 points per second, matching the averaged magnetometer data rate.

The result of the spline operation over a section of the flight is shown in figure

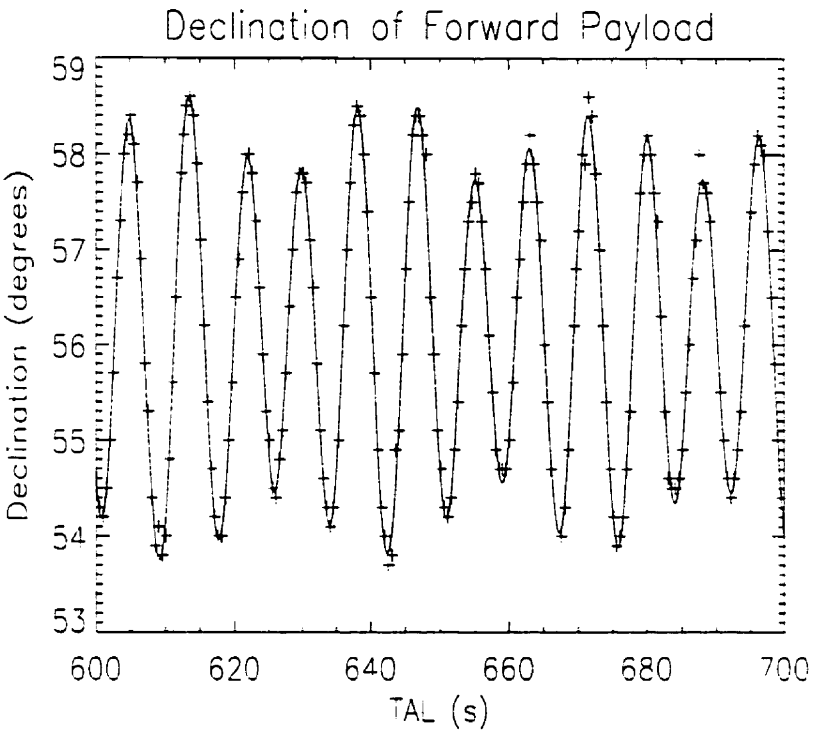

Figure 3.6: Processed attitude data, showing the variation in declination of the spin axis as a smoothly varying function of time. Raw data points are shown as crosses for comparison.

3.6. This approximation to the true payload motion is a smoothly-varying function retaining the coning and nutation of the payload over the flight.

3.4 Coordinate Transformation

Once an acceptable attitude data set is constructed from the video camera information, the magnetometer data can be rotated into an inertial frame.

Using the attitude data and the trajectory information, the position and location of the payload can be determined in a coordinate system that allows the subtrac-

tion of the background geomagnetic field. This leaves only the perturbations from external sources and any residual payload motion in the data set.

The techniques for coordinate transformation are derived from standard procedures, found in *Goldstein* [1950] and *Russell* [1971].

The three payload axes of OEDIPUS-C must be transformed from the celestial system, through a series of steps, to a geomagnetic system that describes the data in a geophysically useful coordinate system.

The first step is to recover the Cartesian representation of the payload attitude in GEI (Geocentric Equatorial Inertial) coordinates, including the spin of the payload.

The three payload axes will be denoted by the vectors $(\vec{X}, \vec{Y}, \vec{Z})$. The $\vec{Y}$ vector denotes the Vehicle Data Axis (VDA), perpendicular to the long (spin) axis of the payload. The $\vec{X}$ vector is perpendicular to the VDA and the long axis, and $\vec{Z}$ completes the set, parallel to the long axis, which is also the spin axis of the payload. Transforming the spin axis attitude vector $\vec{Z}$ from celestial coordinates (α, δ) to Cartesian GEI $(Z_x\hat{\mathrm{i}}_{\mathrm{GEI}} + Z_y\hat{\mathrm{j}}_{\mathrm{GEI}} + Z_z\hat{\mathrm{k}}_{\mathrm{GEI}})$ produces the following vector:

$$\vec{Z} = \cos\alpha\cos\delta\ \hat{\mathrm{i}}_{\mathrm{GEI}} + \sin\alpha\cos\delta\ \hat{\mathrm{j}}_{\mathrm{GEI}} + \sin\delta\ \hat{\mathrm{k}}_{\mathrm{GEI}} \tag{3.2}$$

The VDA, $(\vec{Y})$ depends on the roll angle ρ:

$$\begin{aligned}\vec{Y} = (-\sin\alpha\sin\rho - \cos\alpha\sin\delta\sin\rho)\ \hat{\mathrm{i}}_{\mathrm{GEI}} + \\ (-\cos\alpha\sin\rho - \sin\alpha\sin\delta\cos\rho)\ \hat{\mathrm{j}}_{\mathrm{GEI}} + \\ \cos\delta\cos\rho\ \hat{\mathrm{k}}_{\mathrm{GEI}}\end{aligned} \tag{3.3}$$

The $\vec{X}$ axis is the cross product of $\vec{Y}$ and $\vec{Z}$:

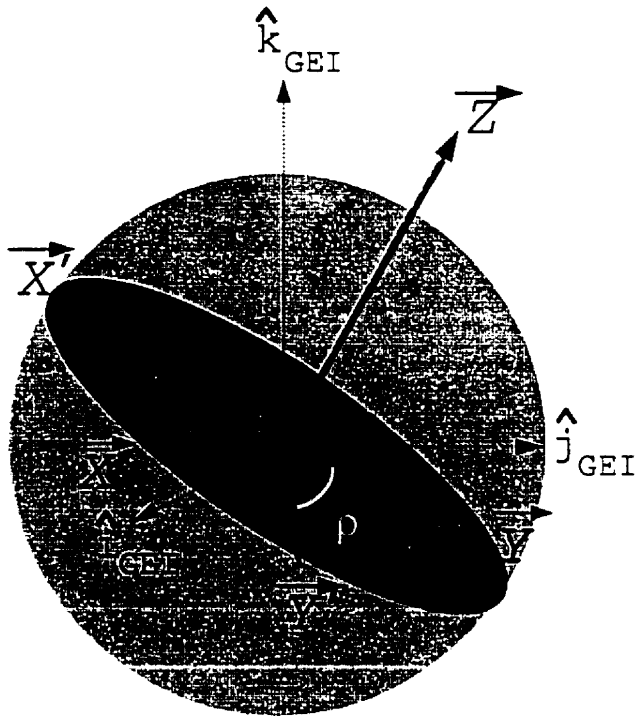

Figure 3.7: Rotation of payload axes due to payload spin. As the payload spins, $\vec{X}$ and $\vec{Y}$ rotate by the angle ρ, from primed ($\vec{X}'$,$\vec{Y}'$) to unprimed ($\vec{X}$, $\vec{Y}$) values.

$$\begin{aligned}\vec{X} = (-\cos\rho\sin\alpha - \sin\delta\sin\rho\cos\alpha)\ \hat{i}_{GEI} + \\ (\cos\rho\cos\alpha - \sin\delta\sin\rho\sin\alpha)\ \hat{j}_{GEI} + \\ \sin\rho\cos\delta\ \hat{k}_{GEI}\end{aligned} \tag{3.4}$$

As these equations are not intuitively obvious from the diagram in (figure 3.7), the matrix notation may give a clearer representation.

The payload attitude in GEI coordinates can be viewed as a series of three rotations.

The first rotation is about the $\vec{Z}$ axis, through an angle $90 + \alpha$ (since the $\vec{Y}$ axis

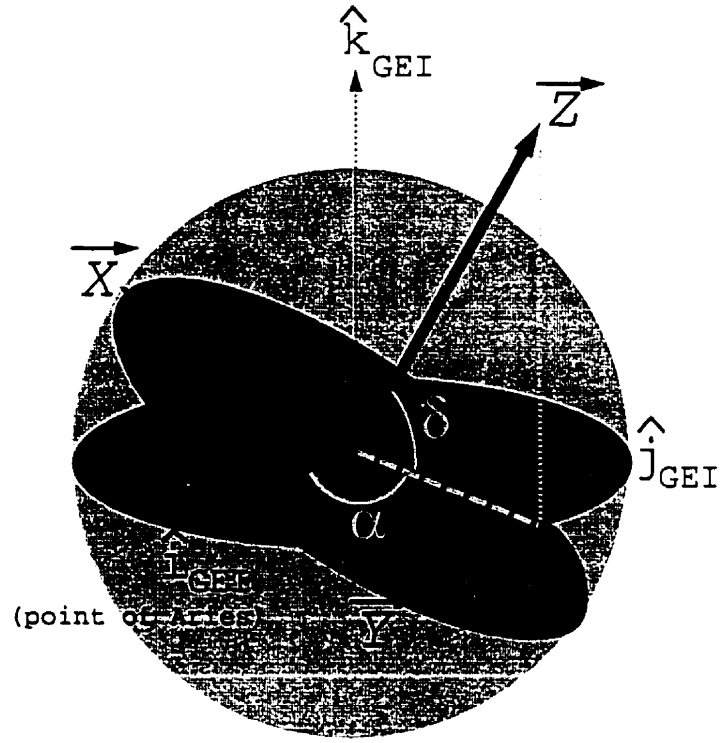

Figure 3.8: Conversion of payload vectors to GEI coordinates

is the primary axis) in a right-handed sense:

$$\mathbf{M}_{\alpha} = \begin{bmatrix} -\sin\alpha & \cos\alpha & 0 \\ -\cos\alpha & -\sin\alpha & 0 \\ 0 & 0 & 1 \end{bmatrix} \tag{3.5}$$

The second rotation is about the new $\vec{X}$ axis through $90 - \delta$.

$$\mathbf{M}_{\delta} = \begin{bmatrix} 1 & 0 & 0 \\ 0 & \sin\delta & \cos\delta \\ 0 & -\cos\delta & \sin\delta \end{bmatrix} \tag{3.6}$$

The final matrix shows a right-handed rotation about the payload spin axis through ρ:

$$\mathbf{M}_\rho = \begin{bmatrix} \cos\rho & \sin\rho & 0 \\ -\sin\rho & \cos\rho & 0 \\ 0 & 0 & 1 \end{bmatrix} \tag{3.7}$$

The product $\mathbf{M} = \mathbf{M}_\rho \mathbf{M}_\delta \mathbf{M}_\alpha$ will recover the three vectors:

$$\begin{bmatrix} -\cos\rho\sin\alpha - \sin\delta\sin\rho\cos\alpha & \cos\rho\cos\alpha - \sin\delta\sin\rho\sin\alpha & \sin\rho\cos\delta \\ \sin\rho\sin\alpha - \cos\rho\sin\delta\cos\alpha & -\sin\rho\cos\alpha - \cos\rho\sin\delta\sin\alpha & \cos\rho\cos\delta \\ \cos\alpha\cos\delta & \sin\alpha\cos\delta & \sin\delta \end{bmatrix} \begin{bmatrix} \hat{\imath}_{GEI} \\ \hat{\jmath}_{GEI} \\ \hat{k}_{GEI} \end{bmatrix} = \begin{bmatrix} \vec{X} \\ \vec{Y} \\ \vec{Z} \end{bmatrix}_{GEI} \tag{3.8}$$

which is the same result from equations 3.2, 3.3, and 3.4.

The next step is to rotate the vectors from GEI coordinates into the geocentric (GEO) coordinate system.

The x-axis of the GEO coordinate system extends from the center of the earth through the equator at the Greenwich Meridian. The z-axis is parallel to the spin axis of the Earth, and the y-axis is orthogonal to both. This system therefore differs from the GEI system by a rotation, by an angle θ, from the first point of Aries to the Greenwich Meridian. This rotation is about the GEI z-axis, eastward from the first point of Aries over the angle θ, as shown in the upper left diagram in figure 3.9, and for the payload $\vec{Z}$ axis is:

$$\begin{bmatrix} \cos\theta & \sin\theta & 0 \\ -\sin\theta & \cos\theta & 0 \\ 0 & 0 & 1 \end{bmatrix} \vec{Z}_{GEI} = \vec{Z}_{GEO} \tag{3.9}$$

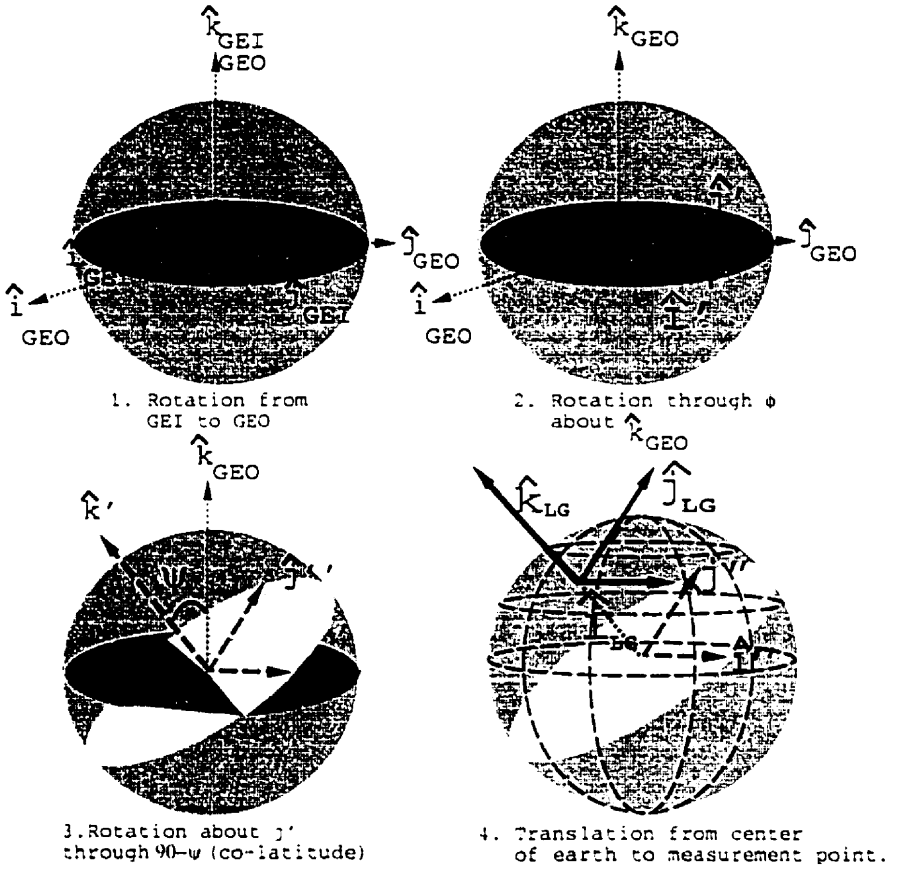

Figure 3.9: Transforming from GEI to the Local Geographic coordinate system: $\hat{i}_{LG}$= East, $\hat{j}_{LG}$ = North, and $\hat{k}_{LG}$ = Outward.

and follows for the $\vec{X}$ and $\vec{Y}$ payload vectors in a similar manner.

The local geographic (LG) coordinate system is the next coordinate system to be rotated into, and it has the axes directed eastward, northward and radially outward from the earth's surface. Rotation to local geographic coordinates from geocentric uses rotations through co-latitude $(90 - \psi)$ and longitude (ϕ). This system is measured with latitude at $\psi = 0°$ at the equator, and $\psi = 90°$ at the poles. Longitude is measured eastward from the Greenwich Meridian. Each payload axis vector trans-

forms via the same rotation matrix, with the example below for the $\vec{Z}$ payload axis:

$$\begin{bmatrix} -\sin\phi & \cos\phi & 0 \\ -\sin\psi\cos\phi & -\sin\psi\sin\phi & \cos\psi \\ \cos\psi\cos\phi & \cos\psi\sin\phi & \sin\psi \end{bmatrix} \vec{Z}_{\mathrm{GEO}} = \begin{bmatrix} Z_{East} \\ Z_{North} \\ Z_{Out} \end{bmatrix}_{\mathrm{LG}} = \vec{Z}_{\mathrm{LG}} \qquad (3.10)$$

The final rotation places the payload axes in the local geomagnetic coordinate system (GM). This system has its z-axis ($\hat{k}_{GM}$) antiparallel to the local geomagnetic field $\vec{B}$ in the northern hemisphere, so that it coincides with $\hat{k}_{L}G$ at the north magnetic pole where $\vec{B}_o$ points into to the earth. The geomagnetic field in LG coordinates is obtained in our case from the International Geomagnetic Reference Field (IGRF) model, which represents a spherical harmonic fit to measured fields.

The GM x-axis ($\hat{i}_{GM}$) coincides with geographic east. GM y ("geomagnetic north", $\hat{j}_{GM}$) is perpendicular to $\vec{B}_o$, and its projection into the geographic horizontal plane coincides with geographic north (see figure 3.10).

Transforming from local geographic to geomagnetic coordinates therefore amounts to a rotation about GEO east through the complement of the magnetic inclination angle I.

$$\begin{bmatrix} 1 & 0 & 0 \\ 0 & \cos I' & \sin I' \\ 0 & -\sin I' & \cos I' \end{bmatrix} \vec{Z_{LG}} = \vec{Z_{GM}} \qquad (3.11)$$

where the angle $I' = 90° - I$.

The rotation into geomagnetic coordinates should normally also include a rotation through the magnetic declination angle "D", so that geomagnetic east is perpendicular to the projection of $\vec{B}_o$ into the horizontal plane. However, in our case we forgo

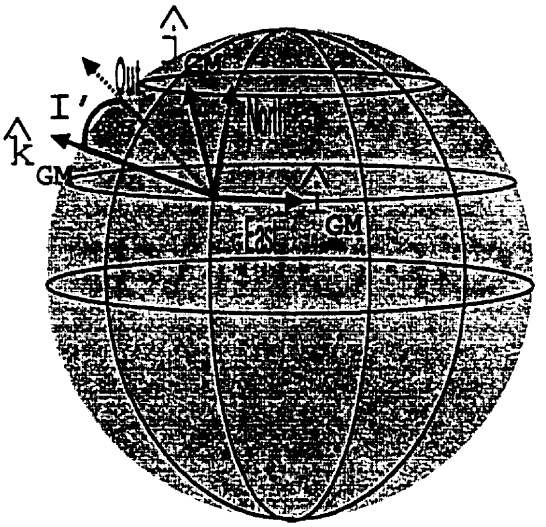

Figure 3.10: Rotation from Local Geographic to Local Geomagnetic coordinates

this final rotation for the following reason. The payload trajectory was nominally northward in geographic coordinates. In computing one component of the curl of $\vec{B}$ (equation 1.5), it is preferable to have a component of $\vec{B}$ nearly perpendicular to the spacecraft trajectory. For this reason, what are termed "geomagnetic coordinates" below are in fact aligned with geomagnetic north but geographic east.

Through the above series of rotations, the three payload axes can be represented in local geomagnetic coordinates. At this point we are ready to include magnetic field information measured along the three payload axes $\vec{X}$, $\vec{Y}$, and $\vec{Z}$. Representing the fields measured along these three components as B_x, B_y, and B_z respectively, the measured field in geomagnetic coordinates is then

$$\vec{B}_{GM} = B_x\vec{X}_{GM} + B_y\vec{Y}_{GM} + B_z\vec{Z}_{GM}. \tag{3.12}$$

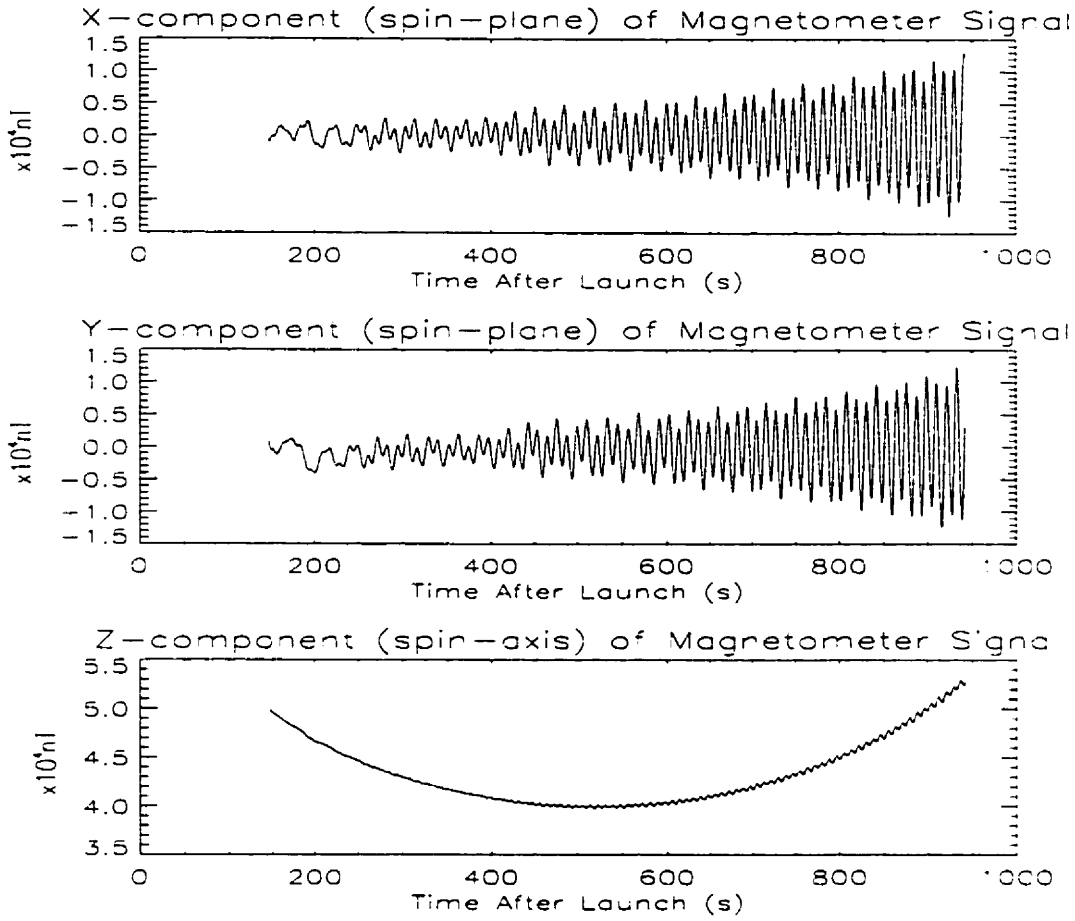

Figure 3.11: Magnetometer data from OEDIPUS-C, in payload coordinates. Data courtesy of Dr. D. Wallis.

3.5 Magnetic Field Data

Figure 3.11 shows the magnetometer data from the forward payload of OEDIPUS-C. The magnetometer data was initially sampled at 854.16 Hz. This was then averaged to 32 samples per second by binning the raw data into 27 point bins and taking the mean of each bin as a single data point. This was done to reduce signal noise and to simplify analysis. The fastest periodic variation in the data is caused by the motion

of the payload as it spins on its axis, and the variation in the amplitude of the signal is due to the coning and nutation of the payload.

The spin axis ($\vec{Z}$) component shows the expected variation of the magnetic field due to the variation of $\vec{B}_o$ over the trajectory of the payload. Figure 3.11 shows the coning motion appearing as the sinusoidal variation in the spin axis magnetometer signal. The large scale variation is due to the magnetic field decreasing as a function of increasing altitude.

The gradual net increase in the magnitude of the spin-plane signals is caused by the payload drifting off the original alignment along the geomagnetic field direction. As the payload drifts away from alignment, the amplitude of the oscillations will increase as the spin-plane-aligned magnetometers are exposed to the strong geomagnetic field as well as any perturbations in the background. This is shown in figure 3.12 as a plot of the angle θ between the spin axis ($\vec{Z}$) and the total magnetic field vector $\vec{B}_o$, calculated as:

$$\cos\theta = \frac{B_z}{\sqrt{B_x^2 + B_y^2 + B_z^2}} \tag{3.13}$$

where B_x, B_y, and B_z are the components of the magnetic field along the three payload axes. As the figure shows, the payload drifted to nearly 14 degrees off alignment with the geomagnetic field, due to the uncontrolled nature of the flight.

3.6 De-spin and smoothing routines

Figure 3.13 shows the eastward and northward components of the magnetometer signal rotated into geomagnetic coordinates. The large residual variation in the data shows that the transformation routine leaves large oscillations due to the fact

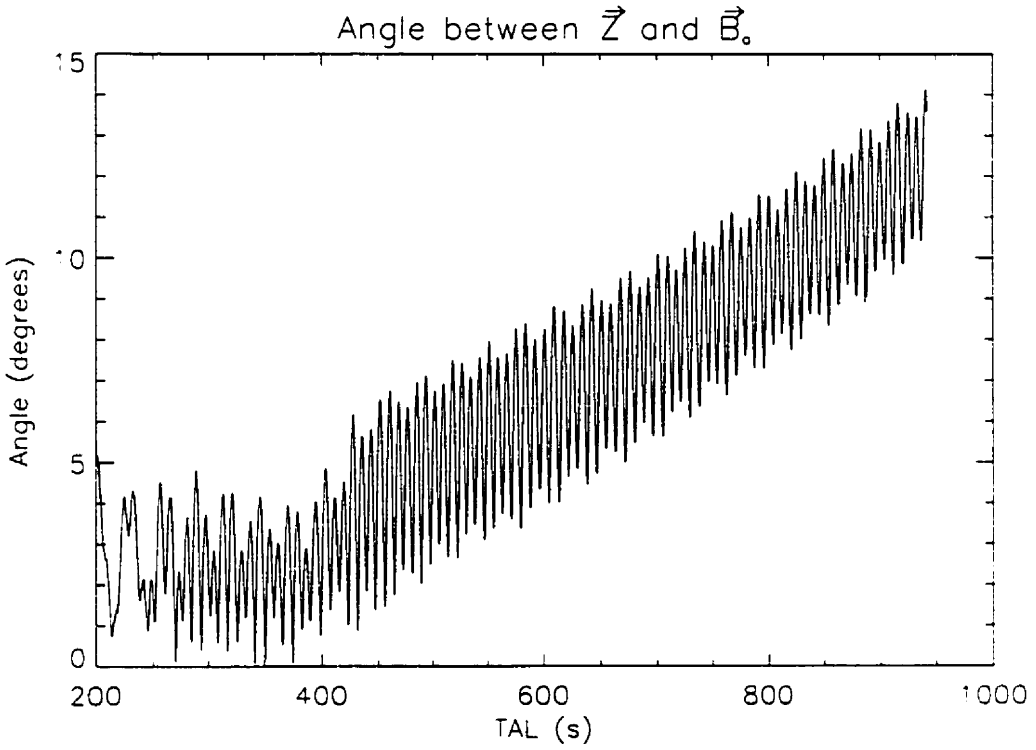

Figure 3.12: Angle between spin axis and magnetic field vector $\vec{B}_o$.

that the smoothed camera attitude data was not sufficiently accurate. The periodic component of the residual signal can be eliminated using low-pass filtering routines.

The residual oscillations are at the spin, coning, and nutation frequencies of 0.084 Hz, 0.110 Hz, and 0.032 Hz, respectively. In order to suppress these oscillations, a digital low-pass filter was applied with a cutoff at the nutation period of 33 s. This limits the resolution to 40 km, due to the average rocket velocity of 1.2 km/s.

The result of the filtering can be seen in figure 3.14. The variation in the data is of the order of 10's of nT embedded in an offset of hundreds of nT. The offset is in part due to the baseline problem, explained below. The convolution technique

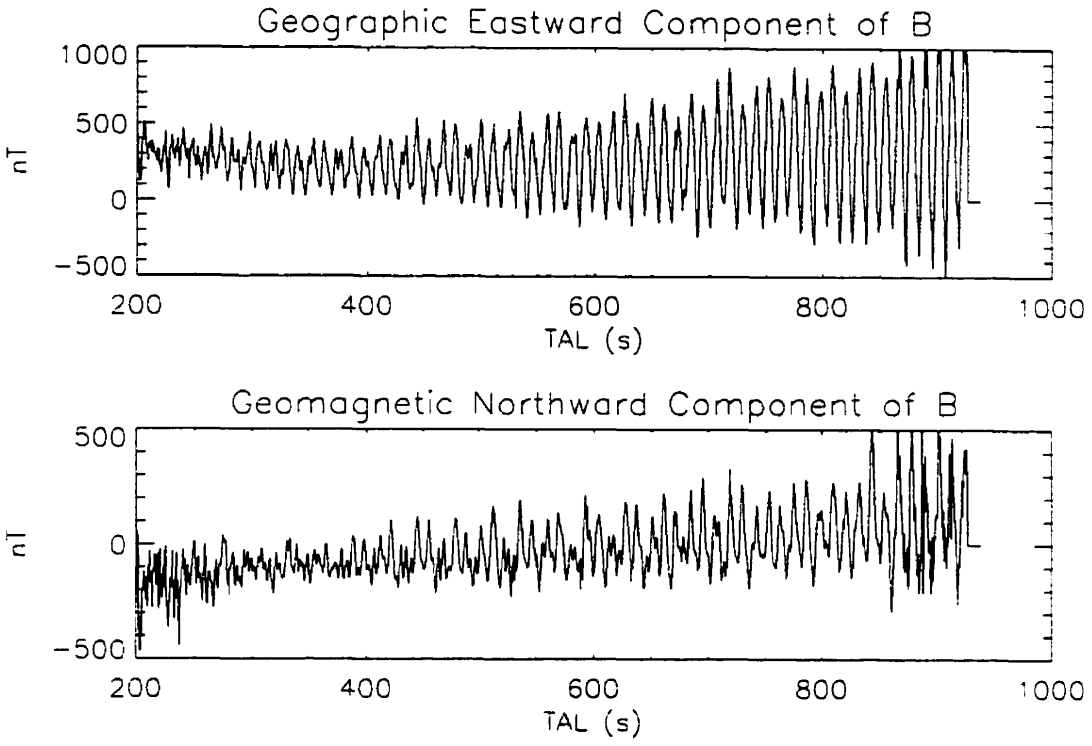

Figure 3.13: Residual components of magnetic field

used to filter the data produces large errors at the ends of the data sets, rendering the information for the first and last 30 seconds or so meaningless. This reduces the available data but has no further effect on the rest of the information.

3.7 Baseline problem

According to *Primdahl and Marklund* [1986], there is no way to uniquely determine the value of currents that have spatial scale sizes similar to the distance spanned by the data set.

Large-scale spatial currents can appear in magnetometer readings as an overall offset in the data, displacing the entire plot and introducing a slope or curve to the

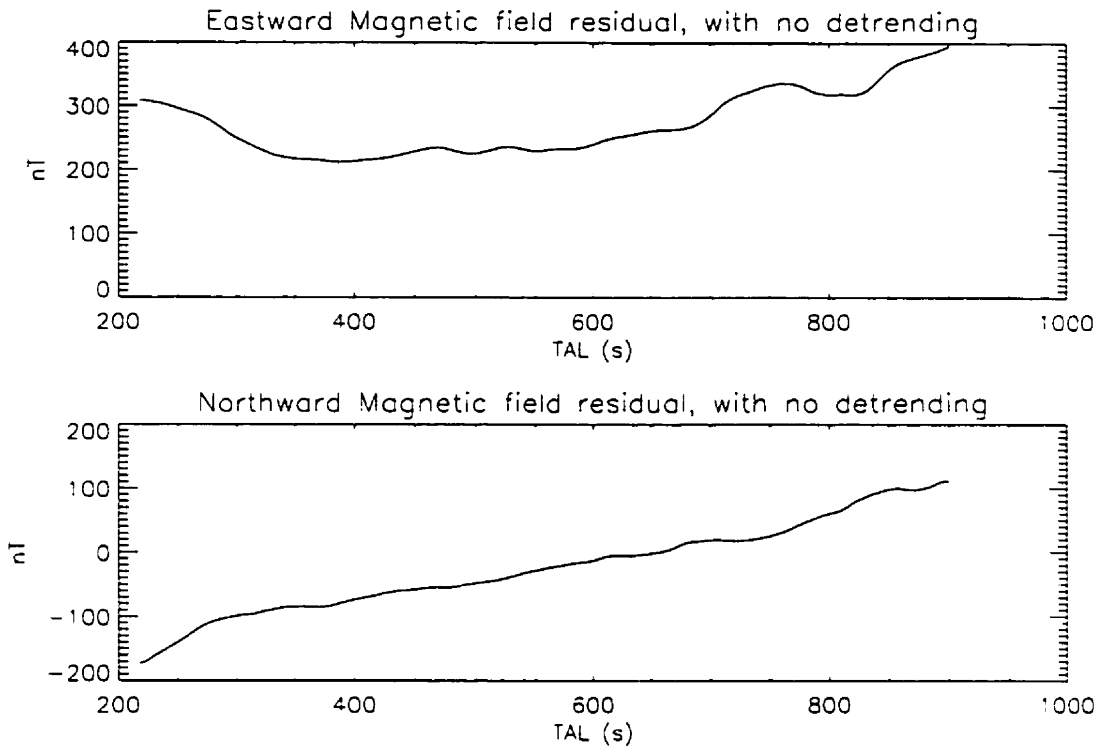

Figure 3.14: Residual magnetic perturbation including offset

B-vs-time plot. The magnetic deviation caused by these currents cannot be identified independently from other effects, such as offsets due to deviations in the subtracted geomagnetic field model [*Primdahl et al.*, 1979]. As a goal of this thesis is to identify structures at the smallest scales resolvable, the elimination of these large-scale offsets does not compromise this goal.

The baseline offset is removed by fitting a low-order polynomial to the perturbation magnetic field. For the data shown in figure 3.14, a 2nd order polynomial was fitted to the north and east components of the magnetic field. As there appeared to be little smaller-scale structure in the anti-parallel component, no offset was applied to this data. What remain are magnetic perturbations with scale sizes of forty to

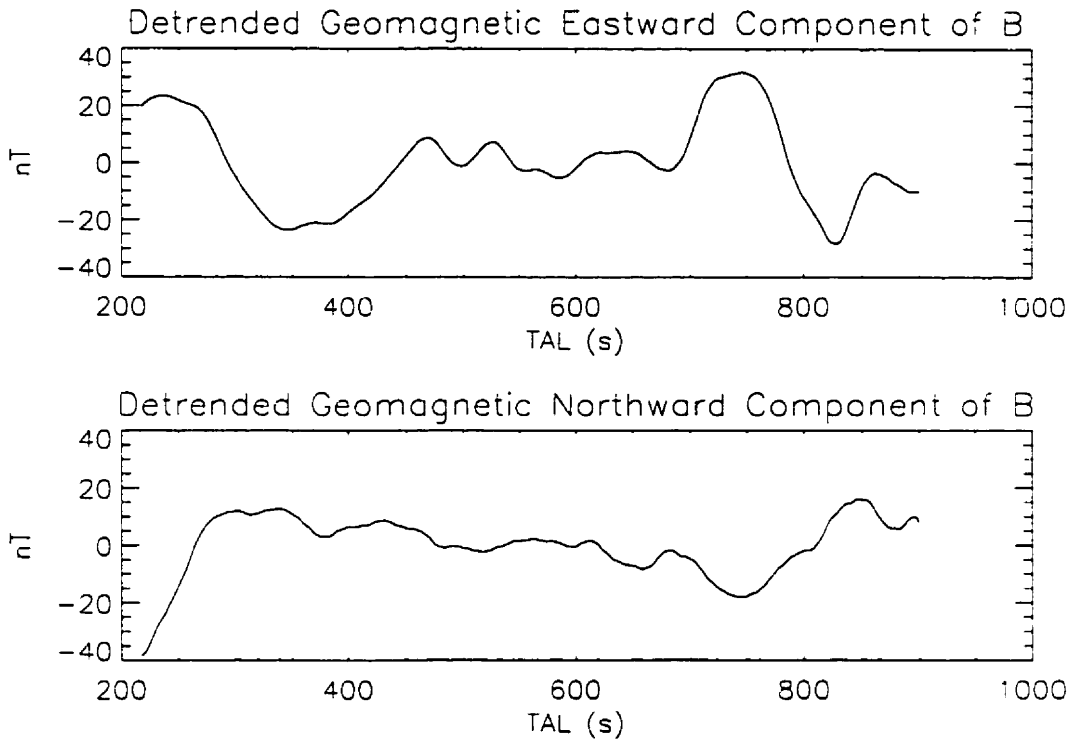

Figure 3.15: Smoothed and detrended components of magnetic perturbation vector

several hundred km (figure 3.15).

In the next chapter, derivatives of these smoothed, detrended data sets are taken in order to determine the properties of field-aligned current systems in the 40-1000 km scale regime.

Chapter 4

Results

This chapter will include descriptions of the geophysically significant results from the OEDIPUS-C magnetometers and electron detectors. These results will be analyzed in conjunction with measurements of total electron density and with ground based auroral observations. Interpretation of the results from this data will be presented.

4.1 Perturbation Magnetic Field

The results shown in figure 4.1 are the completed results of the analysis of the OEDIPUS-C forward payload magnetometers, described in the previous chapter. Shown are all three components of the perturbation field $\Delta\vec{B}$ with the geomagnetic background field subtracted. The perturbations in the eastward component will be attributed to field aligned and east-west oriented current sheets. The degree of deviation from east-west alignment will be discussed below. The antiparallel component shows little structure that can be identified with geophysical phenomena, and is assumed to be an artifact of the analysis.

As this figure shows, the magnetic field perturbations along the flight path of the spacecraft are of the order of tens of nT over scales of tens of kilometers. This corresponds to electrical currents of the order of microamps per square meter ($\mu A/m^2$). Currents of this magnitude are common in similar experiments ([*Park and Cloutier* 1971; *Berko et al.* 1975; *Klumpar et al.* 1976; *Theile and Wilhelm* 1980; *Primdahl*

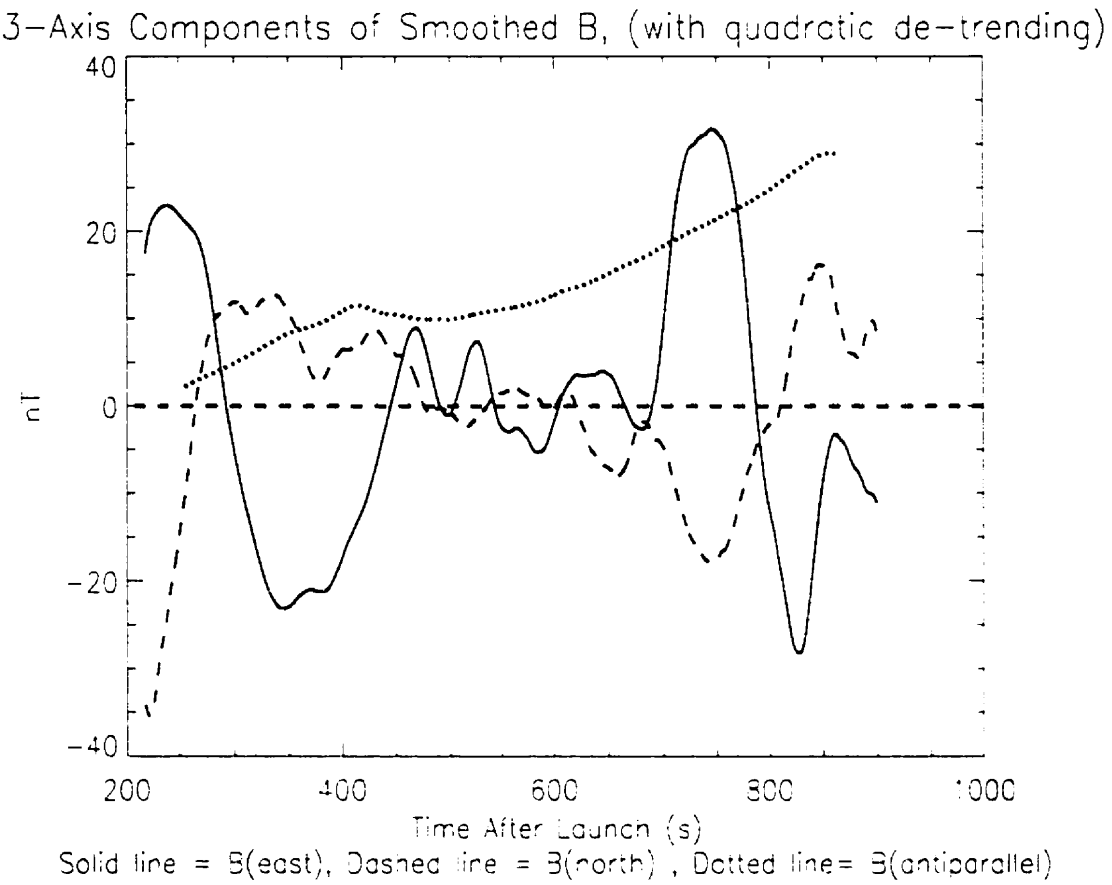

Figure 4.1: Diagram showing detrended perturbation magnetic field components.

and Marklund 1986; *Elphic et al.* 1998] (see section 1.10).

4.2 Shear

In figure 4.2 the magnetic perturbation vector is plotted along the trajectory of OEDIPUS-C. The resultant diagram can show the orientation of field-aligned current sheets along the flight path of OEDIPUS-C.

For upward current sheets aligned perfectly in the east-west plane, magnetic perturbations (the series of blue lines) would be directed in the positive x-direction

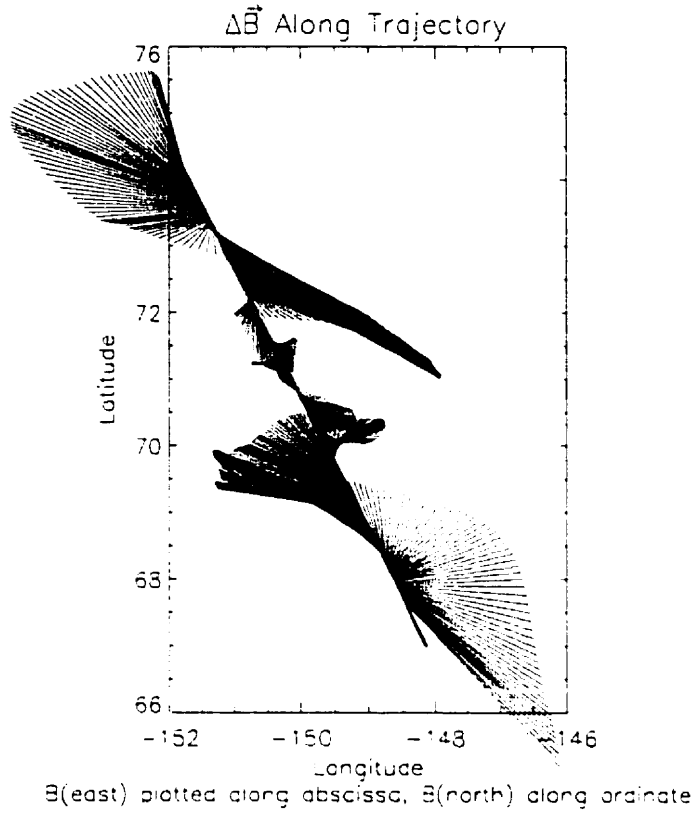

Figure 4.2: Magnetic perturbation vectors along flight path. One degree of latitude is equivalent to 10 nT, and 100 seconds of flight time, starting at 67° = 200 s TAL. Each line extending from the flight path represents a measurement of the magnetic field in eastward (right) and northward (up) coordinates.

of the diagram south of the sheet, and in the negative x-direction north of the sheet. Figure 4.2 shows a series of these polarity switches, as well as evidence of sheets oriented off the strictly east-west plane. The orientations cause north- or south-directed components of the perturbation field to appear on the diagram, so that each blue line in the diagram represents the vector field in the east-north (x-y) plane.

At the beginning of the flight (bottom of figure 4.2), a broad deflection mean-

ders from southeast orientation at 67° north latitude, to an eventual shear centered at approximately 68°. This is followed by a broad deflection, directed essentially westward, suggesting a broad current sheet centered near 69°.

The region between 69.5° and 72.5° contains a series of rapid deflections in the magnetic field, at various angles. What appears as a rotation in the field at roughly 70° latitude suggests a structure other than an infinite current sheet is responsible. If a sheet is truncated to one side of the flight path, one would expect a similar pattern to emerge, such as a rotation. However, with a single series of measurements, there is no way to determine this structures morphology independently.

The large (40 nT) eastward perturbation after 72.5° is accompanied by a deflection southward of nearly 20 nT. The magnetic field switches direction to a northwest heading when the payload passes 73° north latitude, and this northwestward deflection is of similar magnitude and direction to the earlier southeast perturbation. this suggests the presence of a current sheet, oriented $\sim 27°$ north of east.

These sheets appear rotated from the east-west geographic plane, but are, in fact, aligned along geomagnetic latitude. The geomagnetic coordinates are rotated from geographic north through the declination angle D, where D is approximately 27° at the latitudes involved. The structures that appear in the auroral oval are typically aligned on these, rather than geographic, coordinates.

These measurements tell us the current structures encountered by OEDIPUS-C were generally consistent with the infinite current sheet approximation, with the exception of several structures that suggest truncated sheets. These truncated sheets exhibit a smaller magnetic deviation than those associated with the larger, geomagnetically aligned sheets.

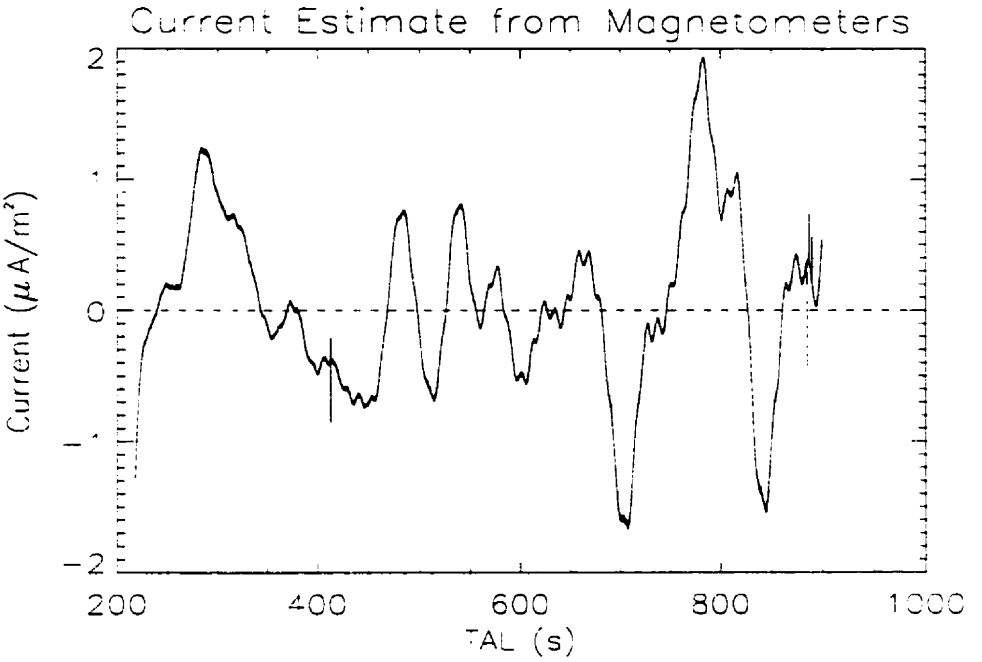

Figure 4.3: Field-aligned current estimate from OEDIPUS-C magnetometers.

4.3 Electric Currents from Magnetic Fields

Field-aligned currents are estimated using the infinite sheet current approximation:

$$j_{up} = -\frac{1}{\mu_o}\frac{\partial B_{\text{East}}}{\partial x_{\text{North}}} \tag{4.1}$$

where x_{North} is the component of the OEDIPUS-C flight path along the geographic northward direction. Therefore, the currents are assumed to be extending along the magnetic field direction and oriented along the east-west axis. The result of the calculation appears in figure 4.3.

The evidence in section 4.2 that sheets are geomagnetically aligned implies that calculating the curl in geographic coordinates underestimates the magnitude of the

current by a factor of $\frac{1}{\tan D} \approx 2$, assuming a declination D of $\approx 27°$.

Figure 4.3 clearly shows a number of positive and negative currents with scale sizes ranging from 120 km down to the resolution limit of 40 km, and with magnitudes of 2 $\mu A/m^2$ and below. Many of the currents shown are paired with oppositely directed currents with similar intensity and extent. Only the single large current structure at the beginning of the data set appears to be unmatched. This current could well have its matching downward current south of the rocket trajectory. A more detailed analysis of the currents will be shown in conjunction with electron measurements.

4.4 Electrostatic Analyzer Data

Figure 4.4 shows the measured differential energy flux from the forward payload electron detectors, for the entire flight of OEDIPUS-C. From this figure, locations of inverted V's (see section 1.9) and regions of inhibited electron precipitation can be found. The figure displays electron flux for the two detectors on the forward payload. The plots show the electron flux at 45° and 90° magnetic pitch angle. The 90° detector will detect primarily electrons mirroring at the payload altitude, whereas the 45° detector samples a range of electron pitch angles moving in the downward hemisphere of velocity phase space. The diagram shows the measured electron precipitation for each of the 16 energy bins in the detector.

The similarities in the two detector results show that for the region of the ionosphere studied, the electron populations were mostly isotropic over the downward hemisphere.

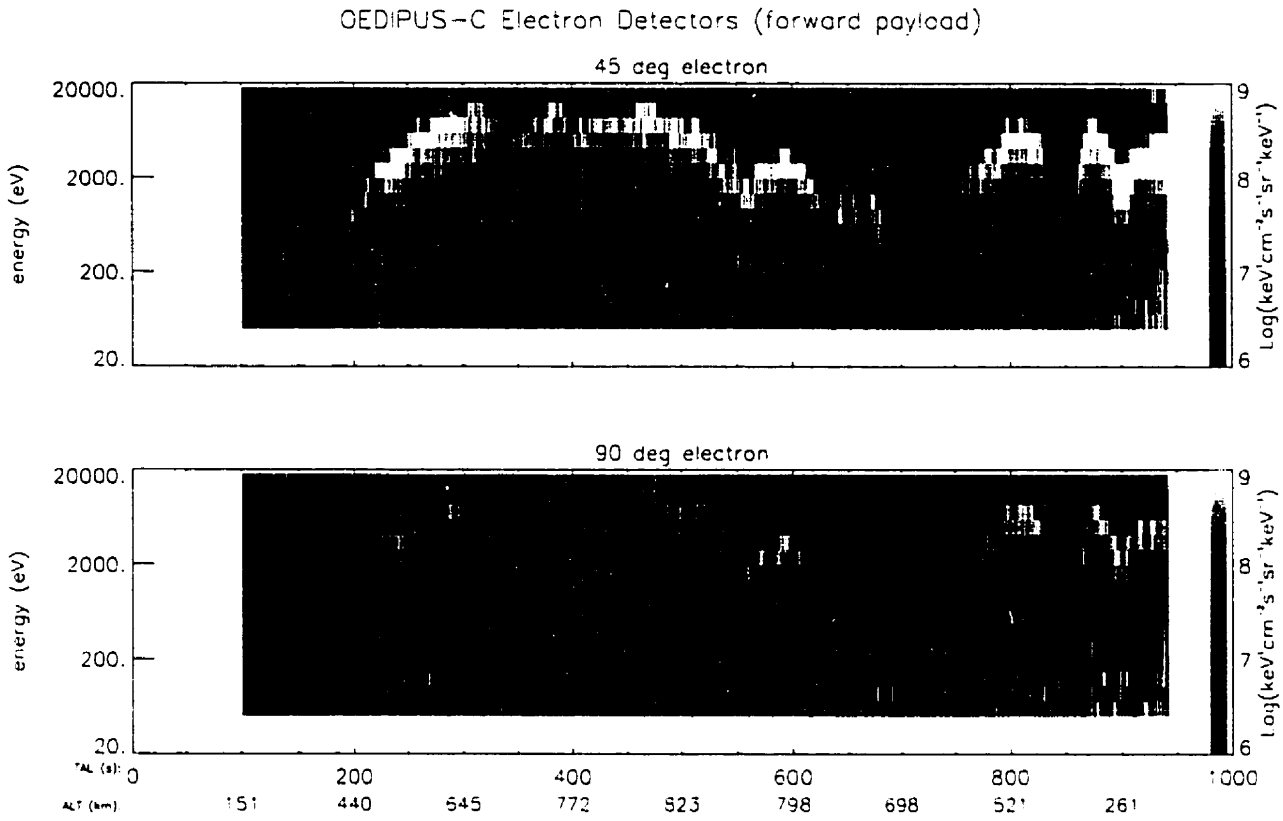

Figure 4.4: Electron spectra from the forward payload electrostatic analyzers. Energy is displayed on the left side in eV (electron-Volts), with the energy flux in units of $keVcm^{-2}ster^{-1}s^{-1}keV^{-1}$.

Figure 4.5 on page 66 shows the flux of electrons for three different energy ranges. There is a very low flux of low-energy (50-500 eV) electrons for most of the flight, with the exception of the final 100 seconds. The medium-energy electrons (500 eV-2 keV) show some structure but it is clear the majority of the flux is contained in the 2 keV-18 keV electrons.

This display of energy-dependent flux provides important information on the distribution of electrons in the region overflown by OEDIPUS-C. The structure apparent

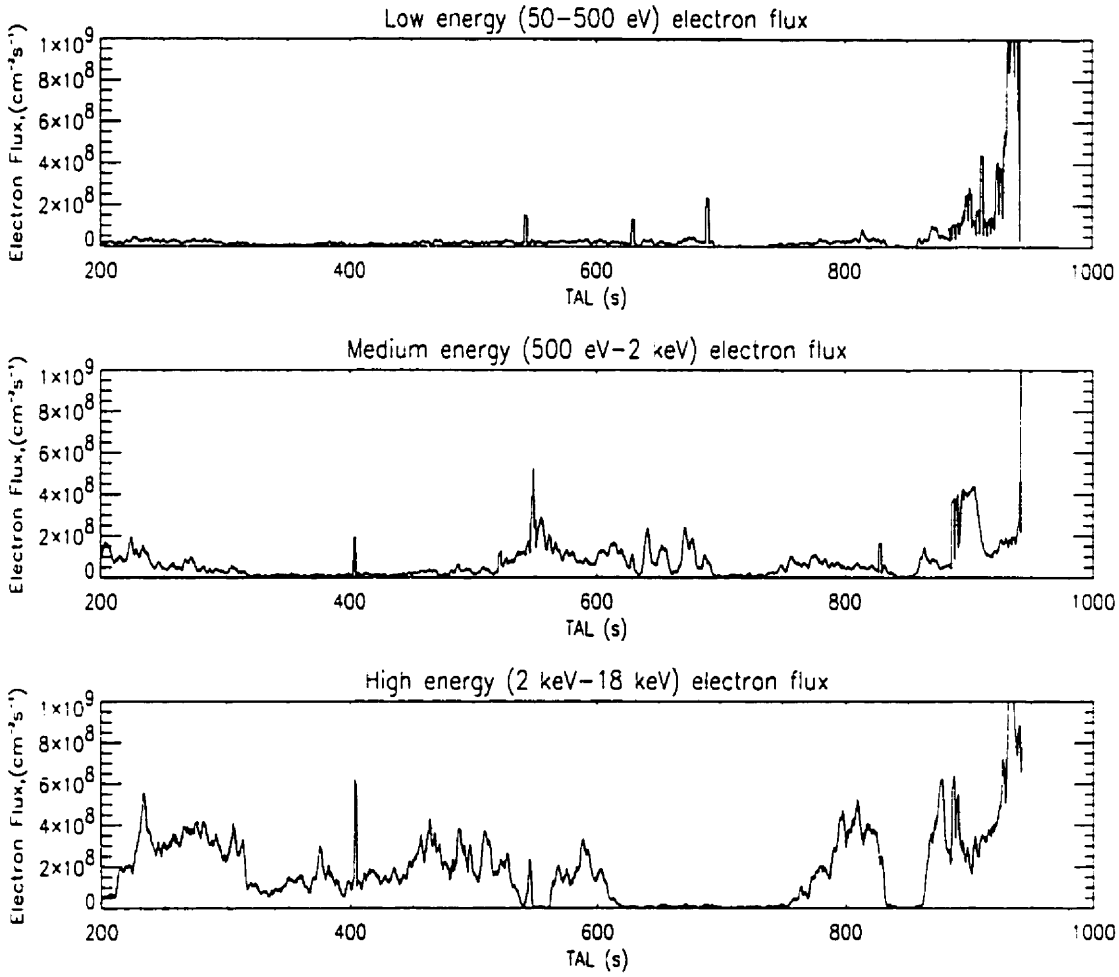

Figure 4.5: Electron flux separated into high, medium, and low energies

in the higher-energy electrons is notably absent in the lower-energy data. Also, at the end of the flight, a large flux of electrons over the entire 50 eV-18 keV spectrum appears in the data.

4.5 Electron Current

The electric current carried by the electrons in the 50 eV - 18 keV energy range measured by the electron detectors can be estimated. Electron energy flux is converted to field-aligned current by the following formula (see Appendix B):

$$J_{||} = q_e \pi \frac{\Delta E}{E} \sum_{i=0}^{15} j_{E_i} \tag{4.2}$$

j_E is the differential energy flux and represents the kinetic energy per unit area, solid angle and energy carried by the electrons in the ith energy bin.

The charge of the electron is of course $q_e = -1.6 \times 10^{-19}$ C.

$\frac{\Delta E}{E}$ is the energy resolution for the detector (a constant for all energy steps, equal to 0.05).

The result of equation 4.2 applied to both forward payload detectors appears in figure 4.6. As the configuration of the experiment limited the detectors to measuring only those electrons with net downward motion, no downward electrical currents (upflowing electrons) could be measured with the electron detector experiment.

The energy fluxes measured by the 90° detector were considerably smaller than those found by the 45° detector. This suggests the isotropy of flux breaks down near 90° pitch angle, and therefore the current implied by the 45° detector will be assumed to be more accurate.

The current determined by the magnetometers will be compared to the current measured by the 45° electron detector. This comparison will be done in three sections, corresponding roughly to arbitrary regions of high- ($> 1\mu A/m^2$) and low-strength ($< 1\mu A/m^2$) currents as measured by the magnetic perturbations. There-

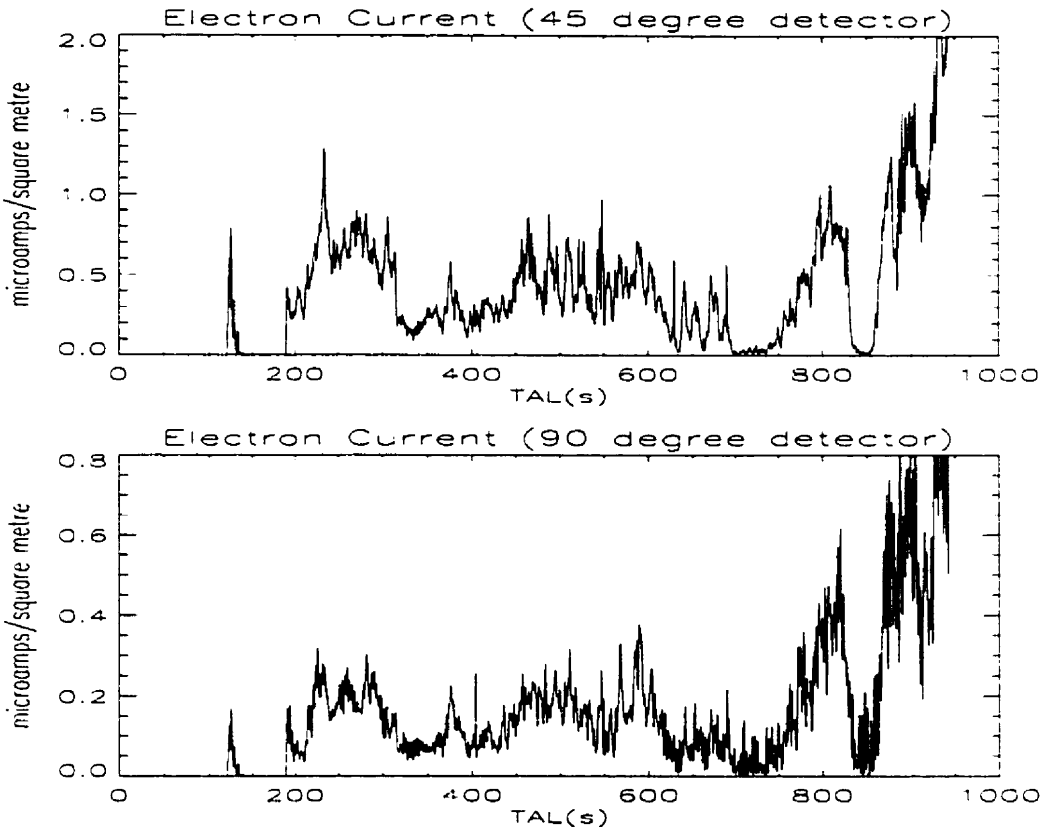

Figure 4.6: Current derived from electron measurements

fore, there are three regions to study. Section I starts at the 200 seconds to 350 seconds. Section II spans 350-675 seconds, and Section III covers the remainder of the flight.

4.6 Magnetometer Current Description

Field-aligned currents calculated according to equation 4.1 and 4.2 are compared in figure 4.7.

Section I in figure 4.7 shows a single current structure with a peak of 1.2 $\mu A/m^2$. This positive current region is the result of a 50 nT drop in the eastward component

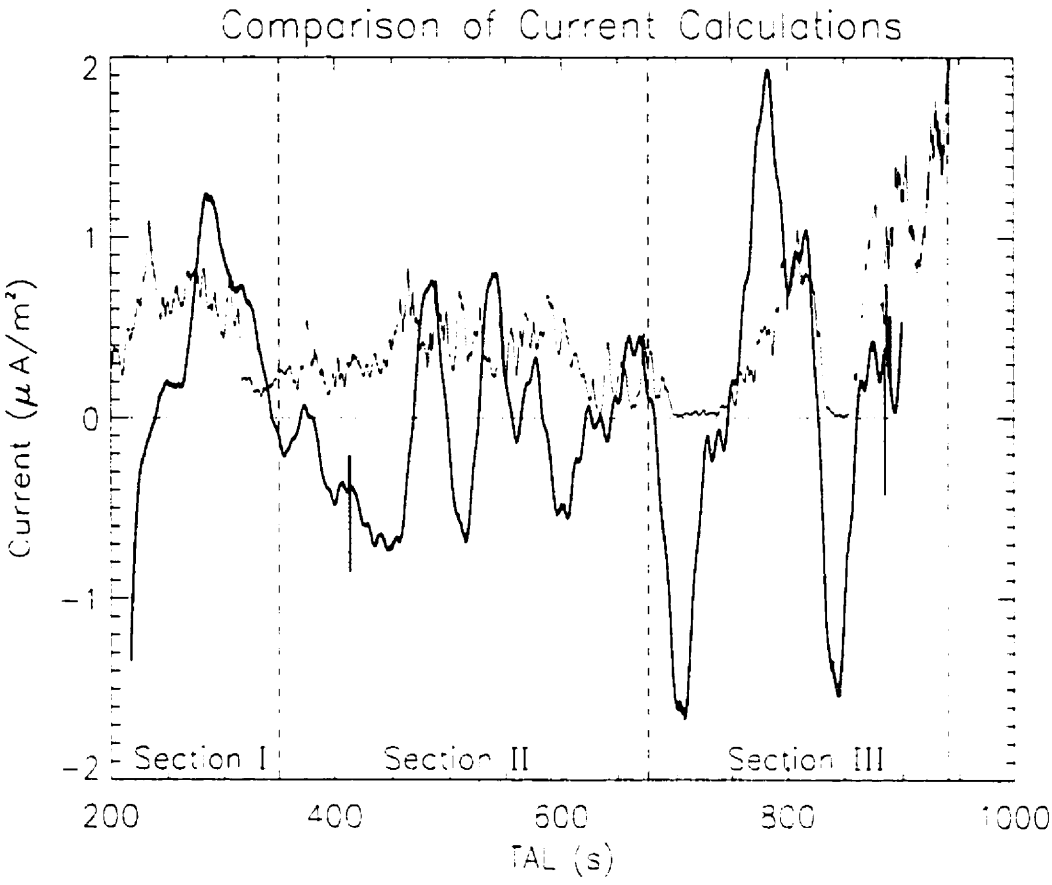

Figure 4.7: Field aligned currents derived from electron flux (red line) and from Ampere's law using magnetic perturbation data (black line)

of the magnetic field.

Section II shows a great deal of smaller-scale structure. Multiple pairs of oppositely directed current sheets appear, with forms appearing at scales down to the resolution limit of 40 km. This region corresponds to the highest portion of the flight, with the payload ranging from 700 km to the 824 km apogee.

The third Section shows 3 large (-1.7, 1.9, and -1.6μA/m^2 respectively) currents alternating from negative to positive and back. At the final seconds of the flight, a

positive trend appears, but the data set ends before it can be revealed. If a second large positive current exists after 950 seconds, it would indicate that there were two sets of oppositely directed current sheets in the region covered during the final 200 seconds of the flight. The observation that the intensities of the three currents measured in this region are nearly equal in magnitude lends support to this reasoning, since the net current into the ionosphere must be zero.

4.6.1 Electron current analysis

Section I (figure 4.7) appears to show an inverted V structure with definite truncation at 300 seconds. Section II shows a diffuse inverted V spanning the entire length. At scales of tens of seconds or less there appear smaller fluctuations in the measurements, but the current remains between 0.2 and 0.7 $\mu A/m^2$ throughout. The third Section shows intense inverted V's as well as two dropouts in precipitation at 700-750 seconds and at 830-860 seconds. At the end of the flight a large flux of electrons across all energy ranges appears, carrying more intense currents ($> 2\ \mu A/m^2$). This is the result of the payload entering the atmosphere below 200 km, where more dense populations of charged particles exist.

4.7 Comparison of Current Estimates

Figure 4.7, along with figures 4.8, 4.9, and 4.10, show the two current estimates according to the three sections discussed above. The current derived from analysis of the magnetic field perturbations (labeled "perturbation current", or $J_{pert.}$) shows both directions of current flow, whereas the current from the electron detectors

("electron current", $J_{||}$) is limited to upward current (downward electrons) only.

Table 4.1 shows the average current strength over the three regions for both electron current and perturbation current.

Table 4.1: Average current strength

Section	$J_{||}(\mu A/m^2)$	$J_{pert.}(\mu A/m^2)$
I	0.52	0.40
II	0.37	-0.08
III	0.41	0.04

As the table shows, there are considerable differences in average current density in the last two sections. This is due in part to the electron current only measuring upward current, whereas the perturbation current measured current in both directions. It is interesting to note that the average current in the final two sections is nearly zero, which is as expected, as most of the currents in this region appear in oppositely directed pairs. The measurement of average current shows that these pairs are closely matched in intensity and mean strength.

4.7.1 Section I

The first section shows an inverted V and, offset by some 30 seconds, a $1.2\mu A/m^2$ upward current. Although the correlation of two signals is not strong for this portion, the large-scale characteristics of the region seem to be the same for both detector results. The general trend suggests a single broad current structure/inverted V covering roughly two-thirds of the 150 second interval. Although not spatially coincident,

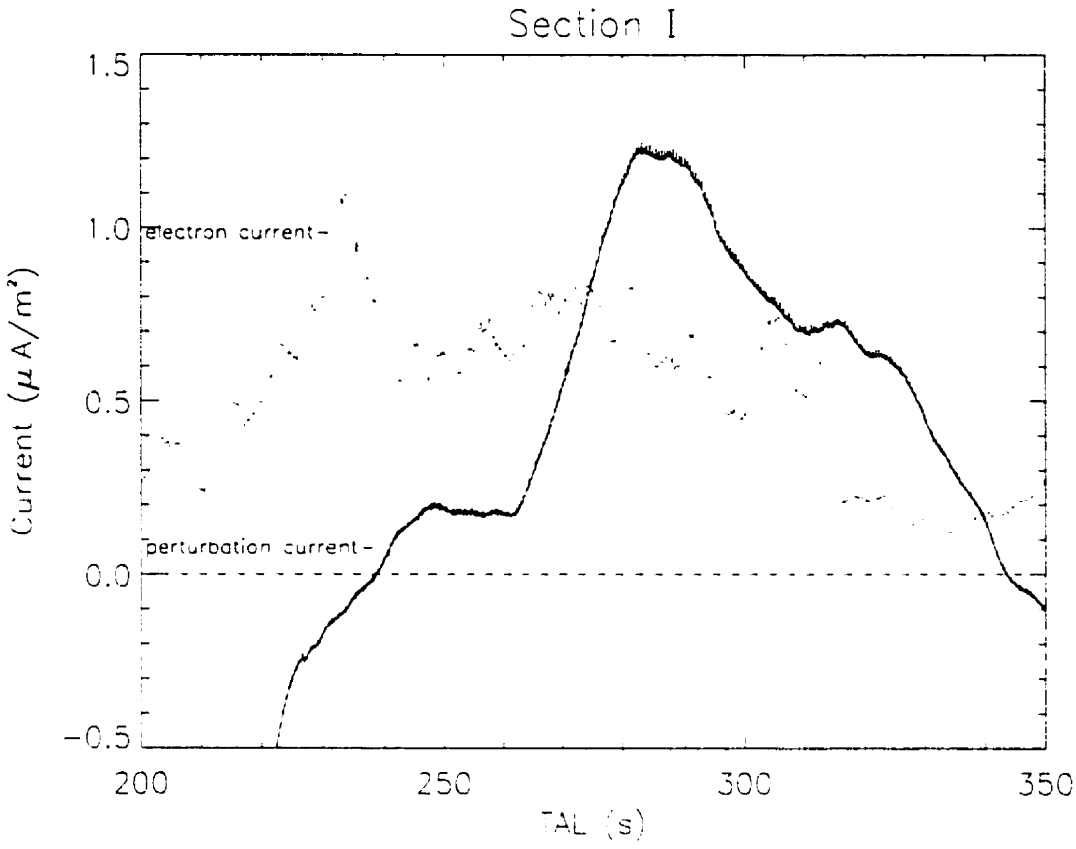

Figure 4.8: Section I: 200-350 s

the net upward current sheet strength derived from both detectors is roughly 1.0 μA/m^2.

4.7.2 Section II

This section shows clearly that here no correlation exists between the two data sets. Clearly, the electrons detected by the instruments aboard OEDIPUS-C are not responsible for carrying the currents observed. The diffuse inverted V that spans this section suggests the presence of a weak downward current of near-uniform density,

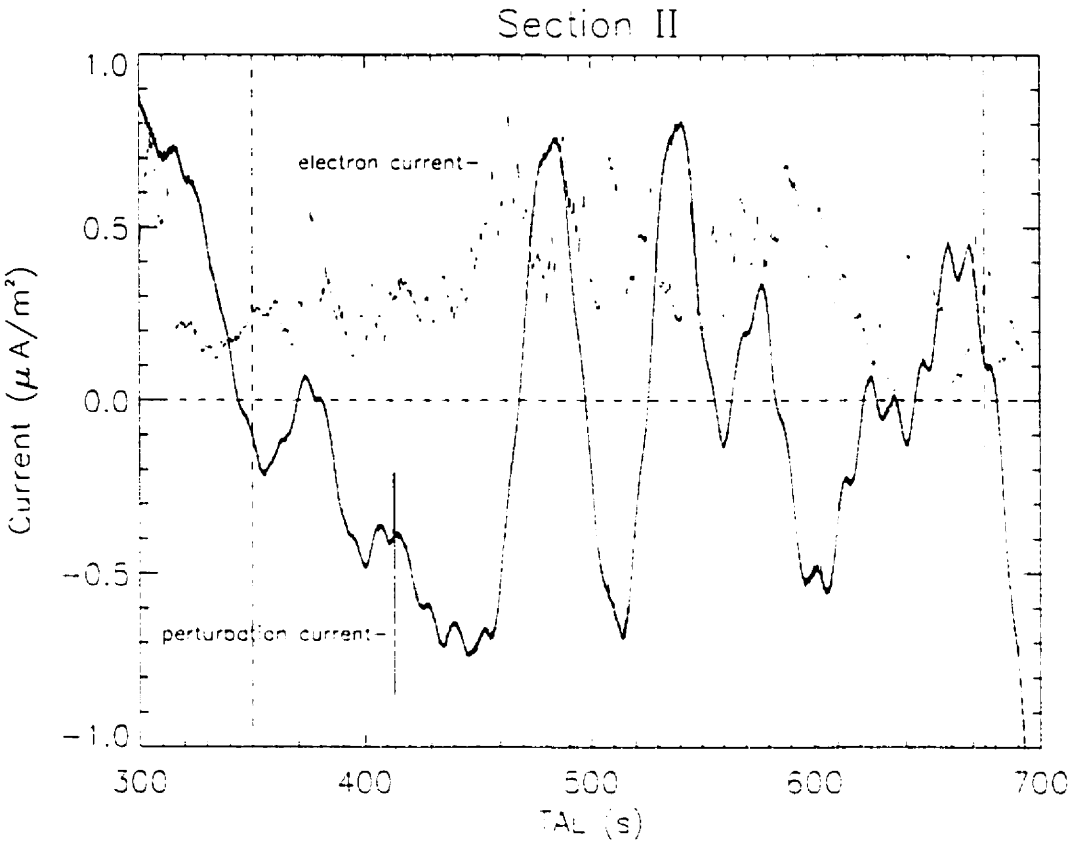

Figure 4.9: Section II: 350-675 s

yet the current measured from the magnetic perturbations shows highly-structured currents, including upward- and downward-directed regions.

4.7.3 Section III

This region, containing the strongest currents over the flight and the highest net electron densities (see figure 4.5), also shows the strongest correlations. The two downward currents are matched almost identically with dropouts in measured precipitation in the electron data, as would be expected. The large upward current is

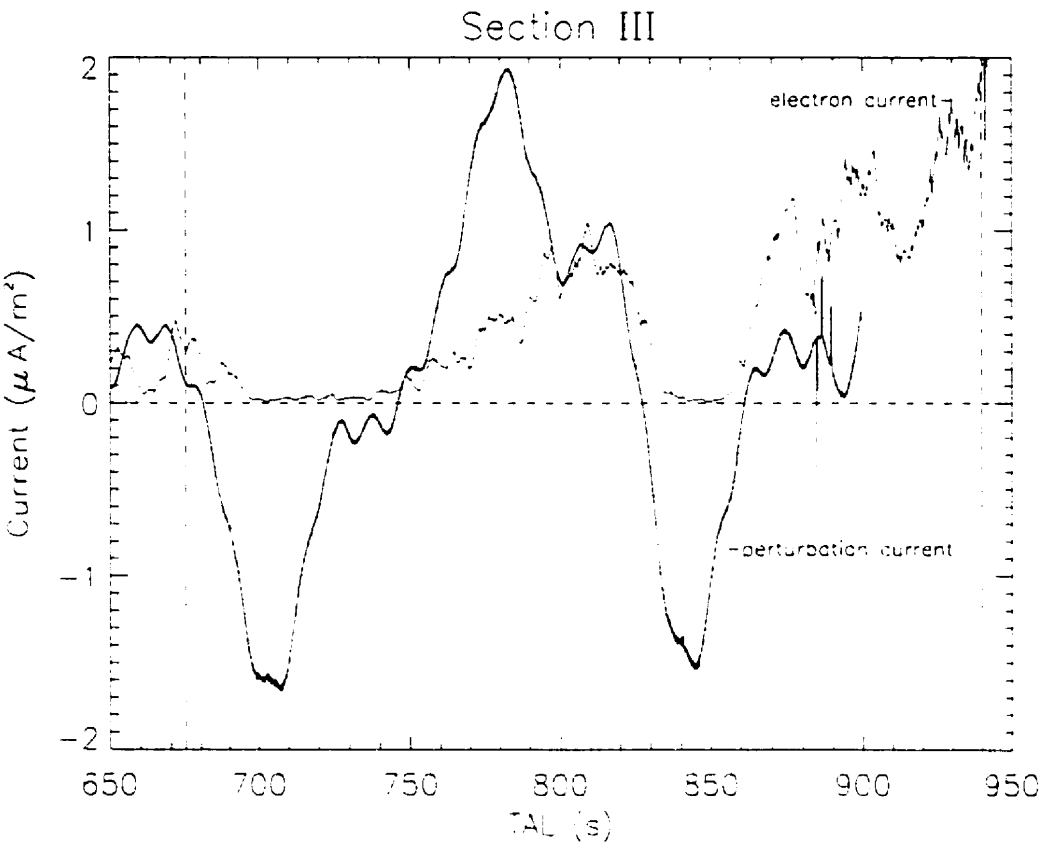

Figure 4.10: Section III: 675-957 s

matched with an inverted V, as seen in figure 4.4. Although the intensity of the electron current is approximately half that of the current inferred from $\Delta\vec{B}$, the widths of the two structures are very similar. At the truncation of the $\Delta\vec{B}$ current data, there appears to be an upward current developing in the region that has the strongest inverted V's over the flight. It is easy to imagine the correlations would continue for the portion of the flight not covered by the truncated magnetic field data.

As the electron detectors were not subject to the truncation resulting from filter-

ing routines as the magnetometer data, there is an additional 40 seconds of electron data after 900 seconds.

4.8 Discussion

Lack of similarity in current structure between electron flux and magnetometer-derived current in Section II could be the result of one or more of the following effects:

1. Electrons outside the 0.1-18 keV energy range were carrying the current, or
2. The distribution of electrons in this region was highly anisotropic, as strongly field-aligned fluxes would be underestimated by the fixed electron detectors.
3. The magnetometer results do not accurately show legitimate current structures, and are merely artifacts of the analysis.

The fact that the electron detectors have a finite energy range and a limited field of view prevents the sampling of the entire electron population over the flight. Highly structured electron distributions beyond the range of the detectors in energy or alignment cannot be ruled out. However, the results appear to show structures well within the energy range of the detectors.

As the 45° electron detector measured three times as much energy flux as the 90° electron detector, it is likely that the distribution of electrons was anisotropic, with greater fluxes at smaller pitch angles. The setup of the experiment did not allow for all pitch angles to be measured, so it was not possible to accurately determine

the contribution of strongly field-aligned or anti-field-aligned electrons to the total current.

If the magnetometer results are merely artifacts of the analysis, one would not expect the results in Section III to be so similar. The colocation of downward perturbation current with gaps in precipitating electron flux is not likely to be due to coincidence. Although the resolution of the magnetometer results is not as fine as one would hope, these similarities suggest that the structures present are real geophysical phenomena.

The results of the current measurements appear in *Prikryl et al.* [2000], and are used in the identification of structures in the ionosphere. The locations of downward currents, matched with gaps in electron precipitation, were seen to occur in regions of density depletions located by ionospheric sounding using the HEX/REX instrument on board OEDIPUS-C. The ionogram results also show a thick, structured E-layer and the absence of an ionospheric F-layer peak, with very low electron densities ($\sim 100/\text{cm}^3$) reported near apogee.

4.9 Auroral Structures

Figure 4.11 shows the OEDIPUS-C trajectory mapped to 100 km altitude, and plotted over the Poker Flat keogram. A description of the auroral structures in comparison to current structures helps in determining the connection between these phenomena. The photometer image from Poker Flat, Alaska allows the identification of the brighter auroral forms, despite a somewhat low resolution resulting form the oblique viewing angle. The brightest auroral structures are catalogued in relation

to the position of OEDIPUS-C mapped to 100 km (figure 4.11), and the results are shown in table 4.2.

Table 4.2: Comparison of auroral currents derived from electron and magnetometer data

Time	Rocket position relative to aurora	Current structure	Peak(μA/m^2) strength
180-240s	entry into large arc	broad,upward	1.2
330s	arc dims	zero current	0
540s	exit arc region	narrow, alternating	+/- 0.5
600s	2° north of bright arc	downward	-0.5
660s	dark spot 5° south	upward	0.5
780s	thin faint arc appears	upward	1.9
850s	arc splits in two, spreads south	downward	-1.7
960s	5° north of intensified north arc	upward	>0.5

Along with the photometer from Poker Flat, *Prikryl et al.* [2000], in a paper described in the following section, identify arcs that were measured by a photometer at Kaktovic, Alaska during the OEDIPUS-C flight (figure 4.12). Kaktovic is situated under the flight path of OEDIPUS-C and is better situated to enable resolution of auroral structures in this region, with less distortion from oblique viewing angles.

This data is presented as a series of auroral intensities with the OEDIPUS-C invariant latitude position superposed. Invariant latitude is calculated from the intersection of the geomagnetic field lines with the surface of the earth. For a given distance L from the center of the earth in the equatorial plane (in units of earth radii), the invariant latitude θ can be found on the surface of the earth via:

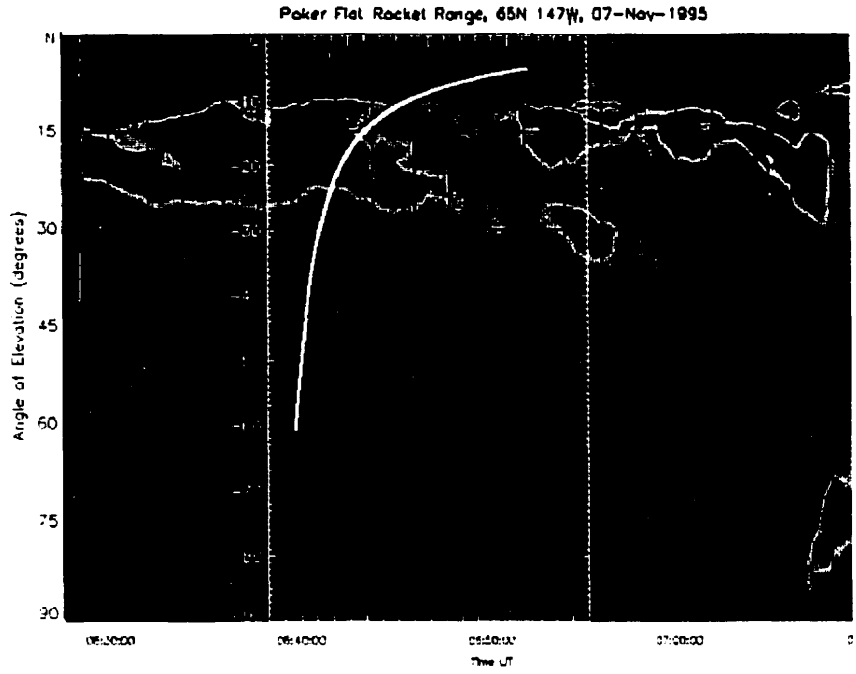

Figure 4.11: Downrange projection of OEDIPUS-C flight onto Poker Flat keogram, to 100 km altitude.

$$r = \mathrm{L}\cos^2\theta \tag{4.3}$$

with r being the distance from the center of the earth to the surface. Since the dipole field of the earth is tilted with respect to the planet, the invariant latitude is offset from geographic latitude towards North America by roughly 11.5° [*Russell*, 1971]. The photometer viewing angles were converted to invariant latitudes, assuming auroral emission height of 100 km.

According to this data, OEDIPUS-C flew through a broad arc between 150 and 350 seconds, another from 375 to 500 seconds, and passed along the equatorward edge

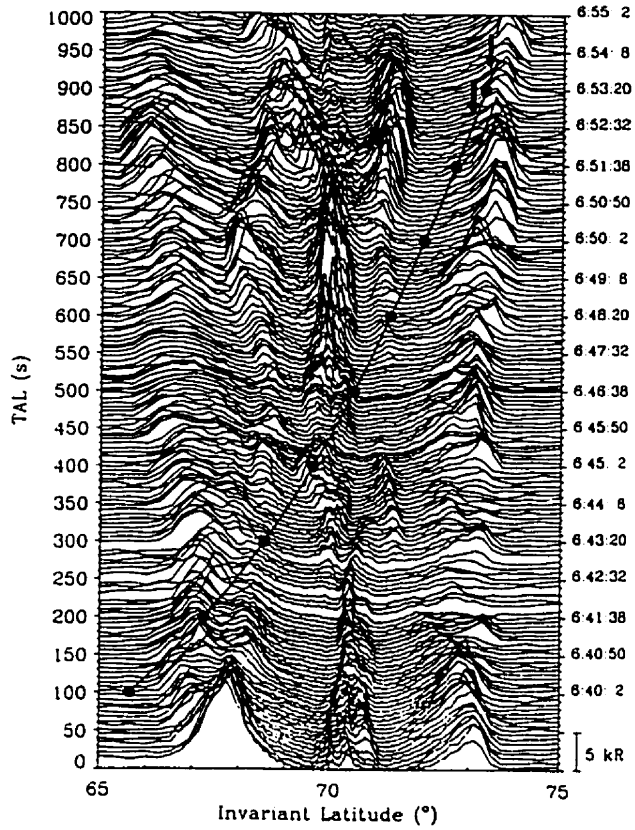

Figure 4.12: A stacked plot of the Kaktovic meridian scanning photometer scans of the auroral 557.7 nm emission intensity on November 7, 1995 mapped on the invariant latitude grid. The OEDIPUS-C invariant latitude is plotted versus time after launch (TAL). From *Prikryl et al.* [2000] (His figure 1.)

of another arc between 850 and 920 seconds. The first arc is also measured at Poker Flat, and the northward half of the arc is coincident with the inverted V measured by OEDIPUS-C that spans 260-350 seconds. The other arcs seen from Kaktovic are washed out in the Poker Flat image, due to the intensity of the arcs that appear closer to the Poker Flat station. The second (375-500s) arc does not correspond to electron precipitation structures, but a downward current calculated from the magnetometer data appears coincident with the payload passing along the poleward

boundary of the arc at 510 seconds (figure 4.9). The equatorward crossing of the third arc at 850 seconds corresponds to the region of zero precipitation and strong (-1.5μA/m^2) downward current. This matches findings in experiments detailed in section 1.10.

These results suggest that it would be valuable to design a future dedicated experiment, using high resolution imaging equipment such as described in *Trondsen and Cogger*, [1998] and a simultaneous rocket flight, in order to identify auroral structures and current sheets to a higher degree of accuracy than shown here. Experiments such as OEDIPUS-C show that these type of missions are viable and capable of producing valuable information, even if optimal conditions are not possible.

4.10 Conclusions

Field-aligned current structures as determined by *in situ* magnetic field observations were analyzed in conjunction with measurements of electron flux. Near apogee, magnetometer current measurements appear to be more structured than the electron flux. Electrons outside the detection range (in energy, pitch angle distribution, or both) may be responsible for carrying these smaller-scale currents. Intense currents in the early stages and near the end of the flight were matched more closely with regions of depleted electron precipitation (downward current) and inverted-V events (upward current).

Analysis of optical (557.7 nm) auroral structures was compared to the positions of currents along the flight path of OEDIPUS-C. Results from this comparison show some correlation between arc edges and upward currents, as expected.

The narrow current sheets not accompanied by related precipitation during the 350-675 s section of the flight are evidence of a complex interaction between the electrical currents and the auroral particles that requires further study to understand.

The evidence collected in this thesis shows that there is substantial spatial structure in the electric currents that flow in the ionosphere. The structure of these currents appear at times to be distinct from the electron precipitation responsible for the aurora.

These currents are embedded in the large-scale auroral currents that make up the Birkeland current system. Such structure is further evidence that the behaviour of the ionosphere-magnetosphere system is capable of supporting highly structured forms that persist over the large distances and dynamic environments that define this region.

Bibliography

Ackerson, K. L. and L. A. Frank, Correlated Satellite Measurements of Low Energy Electron Precipitation and Ground-Based Observations of a Visible Auroral Arc. *J. Geophys. Res.*, 77, 1128, 1972.

Acuña, M. H. and C. J. Pellerin, A miniature two-axis fluxgate magnetometer. *IEEE Trans. Geosci. Electron.*, GE-7 252, 1969.

Alex, T. K. High-precision magnetometer using COS-MOS circuits, *Electron. Engng*, 49, 27, 1977.

Anderson, H. R. and R. R. Vondrak, Observations of Birkeland Currents at Auroral Latitudes, *Rev. Geophys. Space Phys.*, 13, 243, 1975.

Arnoldy, R. L., Auroral Particle Precipitation and Birkeland Currents, *Rev. Geophys. and Space Phys.*, 12, 217, 1974.

Berko, F. W., Hoffman R. A., Burton R. K., and R. E. Holzer, Simultaneous Particle and Field Observations of Field Aligned Currents, *J. Geophys. Res.* 80, 37, 1975.

Boström, R. A., A model of the Auroral Electrojets, *J. Geophys. Res.*, 69, 4983, 1964.

Boyd, J. S., Rocket-Borne Measurements of Auroral Electrons, *Rev. Geophys. Space Phys.*, 13, 735, 1975.

Burke W. J., D. A. Hardy, and R. P. Vancour, Magnetospheric and High Latitude Ionospheric Electrodynamics, in *Handbook of Geophysics and the Space Environment*, ed. A. S. Jursa, Air Force Geophysics Laboratory, Air Force Systems Command, United States Air Force, 1985.

Calvert, W. and D. A. Hardy, Local Increases in Auroral Electron Precipitation Which Were Not Accompanied by a Corresponding Increase in the Electric Potential of the Auroral Electron Acceleration Region, *Geophys Res. Lett.*, 24, 2933, 1997.

Carlson, C. W., R. F. Pfaff, and J. G. Watzin, The Fast Auroral SnapshoT (FAST) mission, *Geophys Res. Lett.*, 12, 2013, 1998.

Chen, F. F. Introduction to Plasma Physics and Controlled Fusion. Plenum Press, New York, NY, 1984.

Davis, N. The Aurora Watcher's Handbook. University of Alaska Press, Fairbanks, Alaska, 1992.

Elphic, R. C. *et al.*, The Auroral current circuit and field aligned currents observed by FAST, *Geophys. Res. Lett.*, 12, 2033, 1998.

Feldstein, Y. I. Substorm current systems and auroral dynamics, in *Magnetospheric Substorms*, eds. Kan, J. R., T. A. Potemra, S. Kokubun, and T. Ijima. American Geophysical Union, 1991.

Frank, L. A. and K. L. Ackerson, Observations of charged particle precipitation into the auroral zone, *J. Geophys. Res.*, 76, 3612, 1971.

Goldstein, H. Classical Mechanics. Addison-Wesley Publishing Co. Inc., Don Mills, Ontario, 1950.

Griffiths, D. J. Introduction to Electrodynamics. Prentice-Hall, upper Saddle River, New Jersey, 1989.

Hargreaves, J. K. The solar-terrestrial environment. Cambridge University Press, Cambridge, United Kingdom, 1992.

Ijima, T. and T. A. Potemra, Field Aligned Currents in the Dayside Cusp Observed by Triad, *J. Geophys. Res.* 81, 5971, 1976.

James, H. G. and W. Calvert, Interference fringes detected by OEDIPUS-C, *Radio Sci.* 33, 617, 1998.

Kamide, Y., and G. Rostoker, The Spatial Relationship of Field Aligned Currents and Auroral Electrojets to the Distribution of Nightside Auroras, *J. Geophys. Res.*, 82, 5589, 1977.

Kelley, Michael C. The Earth's ionosphere : plasma physics and electrodynamics. Academic Press, San Diego, California, 1989.

Klumpar, D. M., J. R. Burrows, and Margaret D. Wilson, Simultaneous Observations of Field-Aligned Currents and Particle Fluxes in the Post-Midnight Sector, *Geophys. Res. Lett*, 3, 395, 1976.

Klumpar, D. M. and W. J. Heikkila, Electrons in the Ionospheric Source Cone: Evidence for Runaway Electrons as Carriers of Downward Birkeland Currents, *Geophys. Res. Lett.*, 9, 873, 1982.

Knecht, D. J. and B. M. Shuman, The Geomagnetic Field, in *Handbook of Geophysics and the Space Environment*, ed. A. S. Jursa, Air Force Geophysics Laboratory, Air Force Systems Command, United States Air Force, 1985.

Lin, C. S. and R. A. Hoffman, Characteristics of the Inverted-V Event, *J. Geophys. Res.* 84, 1514, 1979.

McPherron, R. L., Magnetospheric Substorms, *Rev. Geophys. Space Phys.*, 17, 657, 1979.

Marklund, G. R. A. Heelis, and J. D. Winningham, Rocket and satellite observations of electric fields and ion convection in the dayside auroral ionosphere, *Can. J. Phys.*, 64, 1417, 1986.

Minow, J., Description of the MSP instruments, University of Alaska Optical Institute homepage (http://photon.gi.alaska.edu/home.html), 1995.

Ness, N. F., Magnetometers for Space Research, *Space Science Review*, 11, 459, 1970.

Park, R. J. and P. A. Cloutier, Rocket-based measurements of Birkeland currents related to an auroral arc and electrojet, *J. Geophys. Res.* 76, 7714, 1971.

Parks, G. K., Physics of Space Plasmas – An Introduction. Addison-Wesley Co. Inc., Don Mills, Ontario, 1991.

Pazich, P. M. *Rocket-based Measurement of Auroral Particle Fluxes Associated With Field-aligned Currents*, Ph.D. Thesis, Rice University, Houston, Texas, 1972.

Potemra, T. A., Current Systems in the Earth's Magnetosphere, *Rev. Geophys. Space Phys.*, 17, 640, 1979.

Prikryl, P., H. G. James, D. J. Knudsen, S. C. Franchuk, H. C. Stenbaek-Nielsen, and D. D. Wallis, OEDIPUS-C topside sounding of a structured auroral *E* region, *J. Geophys. Res.* 105, 193, 2000.

Primdahl, F. The fluxgate magnetometer, *J. Phys. E: Sci. Instrum.*, 12, 241, 1979.

Primdahl, F. and G. Marklund, Birkeland currents correlated with direct-current electric fields observed during the CENTAUR Black Brant X rocket experiment, *Can. J. Phys.*, 64, 1412, 1986.

Primdahl, F., J. K. Walker, F. Spangslev, J. K. Olesen, U. Fahleson, and E. Ungstrup, Sunlit Cleft and Polar Cap Ionospheric Currents Determined From Rocket-Borne Magnetic Field, Plasma, and Electric Field Observations, *J. Geophys. Res.* 84, 6458, 1979.

Russell, C. T., Geophysical Coordinate Transformations, *Cosmic Electrodynamics* 2, 184, 1971.

Sandel, B. R., *Electric Currents Associated With An Auroral Arc* Ph.D Thesis, Rice University, Houston, Texas, 1972.

Spjeldvik,W. N. and P. L. Rothwell, The Radiation Belts, in *Handbook of Geophysics and the Space Environment*, ed. A. S. Jursa, Air Force Geophysics Laboratory, Air Force Systems Command, United States Air Force, 1985.

Sugiura, M., A Fundamental Magnetosphere-Ionosphere Coupling Mode Involving Field Aligned Currents as Deduced from DE-2 Observations, *Geophys. Res. Lett.*, 9, 877, 1984.

Swift, D. W. Auroral Mechanisms and Morphology, *Rev. Geophys. Space Phys.* 17, 681, 1979.

Theile, B. and K. Wilhelm, Field Aligned Currents Above an Auroral Arc, *Planet. Space Sci.*, 28, 1980.

Ting, F., *OEDIPUS-C Sounding Rocket Calibration Data*, Unpublished Technical Report, University of Calgary, Calgary, Alberta, 1996.

Trondsen, T. S. and L. L. Cogger, A survey of small-scale spatially periodic distortions of auroral forms, *J. Geophys. Res.*, 103, 9405, 1998.

Tyc, G. *Dynamics and stability of spinning flexible space tether systems.* Ph.D. Thesis, University of Manitoba, Dept. of Mechanical and Industrial Engineering, Winnipeg, Manitoba, 1998.

Vo, H. B. *Implications of Viking Dayside Auroral Measurements*, Ph.D. Thesis, University of Calgary, Calgary, Alberta, 1992.

Vondrak, R. R. *Rocket-borne Measurement of Auroral Particle Currents*, Ph.D. Thesis, Rice University, Houston, Texas, 1970.

Zmuda, A. J. and J. C. Armstrong, The diurnal pattern of field aligned currents, *J. Geophys. Res.*, 79, 4611, 1974.

Appendix A

The Fluxgate Magnetometer

This appendix will give details on the operation of the fluxgate magnetometer. First there will be a description of the physical principles involved. then the details of basic magnetometer operation will be discussed.

A.1 Hysteresis

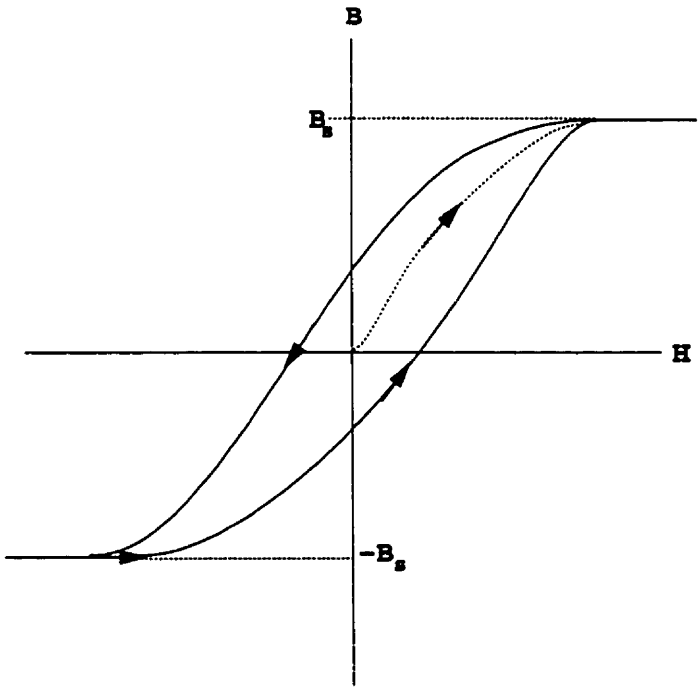

Figure A.1: A hysteresis loop showing the non-linear nature of μ in a ferromagnetic substance.

The magnetic field $\vec{H}$ is a quantity that can only be measured indirectly. What

can be measured is the quantity $\vec{B}$, which is also known as the magnetic field, but may more accurately be considered the magnetic flux density. These two values are connected by the equation $\vec{B} = \mu\vec{H}$, where μ is the magnetic permeability. In a vacuum, this is a constant, μ_o , equal to $4\pi \times 10^{-7}\mathrm{N/A^2}$.

For the calculation of magnetic fields within matter, the concept of permeability becomes more complicated. The interaction of the magnetic field lines with the structure of the material it passes through affects the response of the material to the magnetic field in feedback. For so-called non-magnetic materials and for relatively weak field strengths ($<$ mT), this feedback is minimal, and μ is nearly constant. In other cases the value of μ is dependent on the value of $\vec{H}$, the sign of $\frac{d\vec{H}}{dt}$, and the previous values of $\vec{H}$ [*Primdahl*, 1970].

The largest effect of this feedback occurs in ferromagnetic material. For some ferromagnetic substances like iron, even relatively weak fields can produce the non-linear hysteresis effect (figure A.1). As the magnetic field $\vec{H}$ increases, the lattice structure of the metal allows the internal dipoles to shift in response, until the maximum number of dipoles are aligned in the metal, producing saturation (B_s). If the field is decreased, the dipoles will not return to their previous alignment exactly, but some will remain in the induced configuration [*Griffiths*, 1989].

A.1.1 Induced B from currents

To produce a magnetic field of nearly uniform strength, a solenoid is used. This is simply a loop of N wires per unit length wrapped around a core of magnetic susceptibility μ. The field generated inside the loop is simply $\vec{H} = NI\hat{i}$, with the response of the core as $\vec{B} = \mu NI\hat{i}$ (figure A.2), with $\hat{i}$ along the axis of the solenoid.

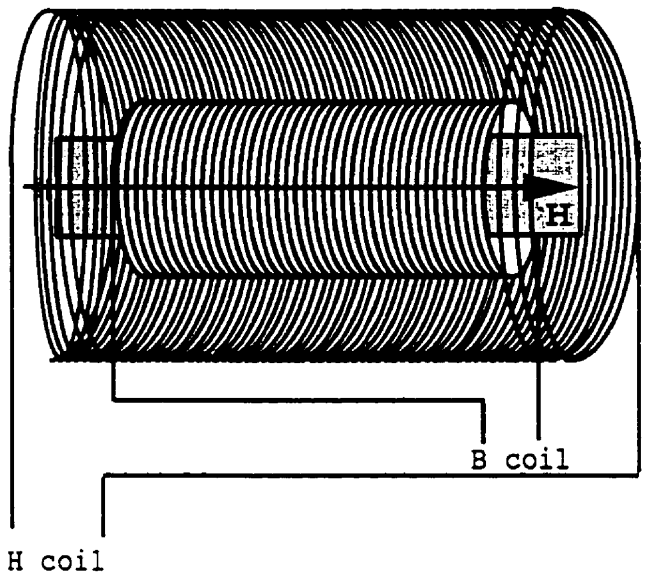

Figure A.2: Solenoidal magnetic field and currents. The primary (outer, shown in cutaway) winding produces $\vec{H}$ and the secondary (black) winding determines the response $\vec{B}$ (figure based on *Primdahl*, [1970].

Outside the field is essentially zero. The generated field can be detected using a secondary loop of wire around the core and measuring the emf produced by the magnetic field. Using an alternating current in the primary loop, one can trace out the response of the core as a hysteresis.

The voltage response across the B coil windings ε is measured to find the variation of the magnetic field in time:

$$\varepsilon = -\mathrm{NA}\frac{\partial B_x}{\partial t} \tag{A.1}$$

for N loops per unit length of wire around a core of cross-sectional area A.

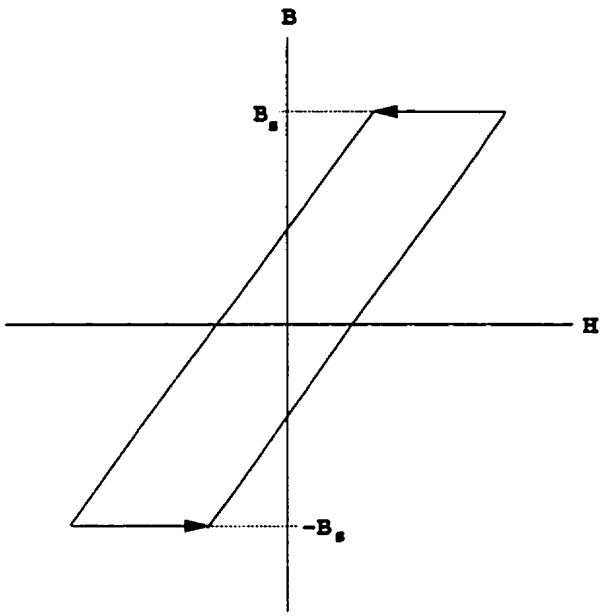

Figure A.3: Simplified hysteresis curve, valid for high drive frequencies and low saturation point cores.

In the presence of an external magnetic field, the core will spend more time in one saturated state, depending on the net direction of the external field. This will show up in the voltage response as an offset in the spacing of the voltage peaks.

This effect is shown in figure A.3 and A.4. The hysteresis curve A.3 is shown in a simplified approximation as a parallelogram, which for fast driving signals ($\sim$1 kHz) is a reasonable model [*Ness*, 1970].

The "gating" of the magnetometers is caused by the saturation of the hysteresis response. Once the core of the magnetometer is saturated, the output voltage will fall rapidly to zero, so the response will appear as pulses separated by periods of null voltage. A reasonably low saturation point allows for higher frequency signals to be used with lower voltage input.

The approximation of the hysteresis as a parallelogram is also a closer fit if the saturation point is low. Care must be taken, however, for if the natural fields encountered are of the order of the saturation level, the cores could conceivably spend the entire time in saturation regardless of the current, and the external field information will be lost. This is seldom an issue in instruments in near-earth space, as the geomagnetic field strength is well known, and perturbations are rarely more than a few percent of the background field.

The process of calculating the voltage response in shown in figure A.4 and is described below:

A triangular wave form is shown as the driving voltage with a period of T (figure A.4(2)). The procedure is identical for other types of alternating currents, such as sinusoidal signals. The use of a triangular function simplifies the analysis without compromising the theory.

The response in the magnetometer to this voltage will be a time-varying magnetic field $\vec{H}_D(t)$. This in turn will produce a magnetic flux B(t) in the core. If no external field $\Delta\vec{H}$ outside is present, the response will appear as in figure A.4(3). If, however, a constant external DC field exists, the response will appear as A.4(4), which shows the offset due to an external DC field positive relative to the magnetometer direction.

The voltage response V_s (figure A.4(5)) is the eventual output from the magnetometer. As shown in the next section, analysis of the voltage response signal can recover the information about the external magnetic field.

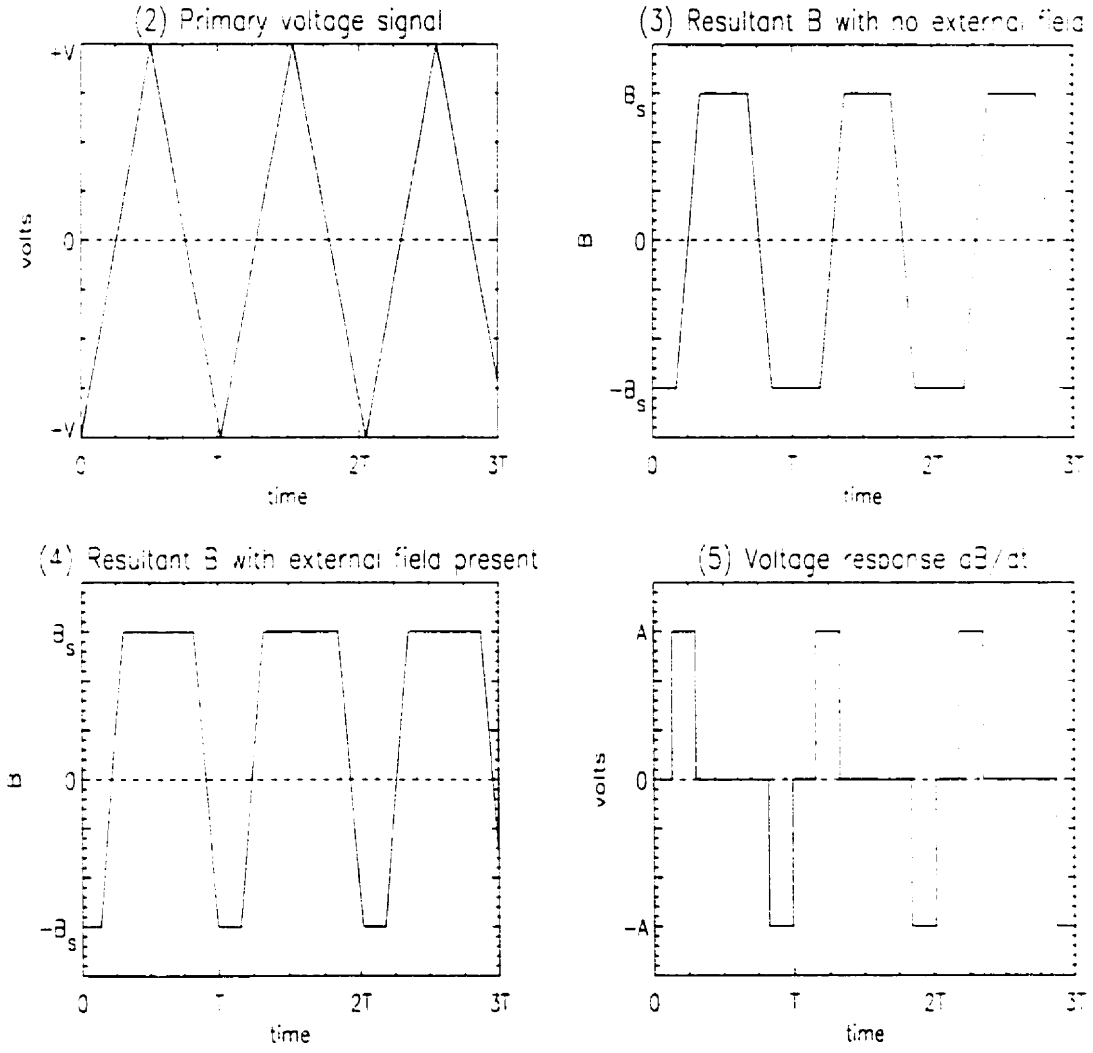

Figure A.4: Steps to calculating a fluxgate magnetometer signal (based on [*Vess*, 1970])

A.2 Harmonic Analysis

The output of a fluxgate magnetometer is analyzed by examining the Fourier series representation of the voltage response. Careful analysis can reconstruct the value of the component of the external magnetic field parallel to the solenoid axis using these methods.

The Fourier transform of the signal V_s in figure A.4(5) can be shown to be:

$$V_s = \frac{d\mathrm{B}}{dt} = \mathrm{A}\sum_{n=1}^{\infty} \cos\frac{2\pi \mathrm{nt}}{T}[1 - \mathrm{e}^{i2n\pi\beta}](\mathrm{e}^{i\pi n\alpha} - 1)\frac{\cos \pi n}{\pi n} \qquad (A.2)$$

with

$$\mathrm{A} = \tfrac{2\mathrm{B}_s}{\mathrm{T}\alpha} \quad \alpha = \tfrac{1}{4}\tfrac{\mathrm{H_D}}{\mathrm{H_C}} \quad \beta = \tfrac{1}{2}(1 - \tfrac{\Delta \mathrm{H}}{\mathrm{H_D}})$$

A = Amplitude of voltage wave form $\quad \mathrm{H_D}$ = Drive Field

$\mathrm{H_C}$ = field strength at saturation $\quad \mathrm{B_s}$ = core saturation

If $\Delta H = 0$, the term in square brackets gives:

$$1 - \cos(n\pi) = \begin{cases} 2 & \mathrm{n = odd} \\ 0 & \mathrm{n = even} \end{cases}$$

so that all even terms are zero and therefore there are no even harmonics when there is no external field. The presence of a nonzero outside field can then be studied by analyzing the even harmonics of the output signal. In practice, only the second harmonic term is studied, as the amplitude of the signal is inversely proportional to the order of the signal n.

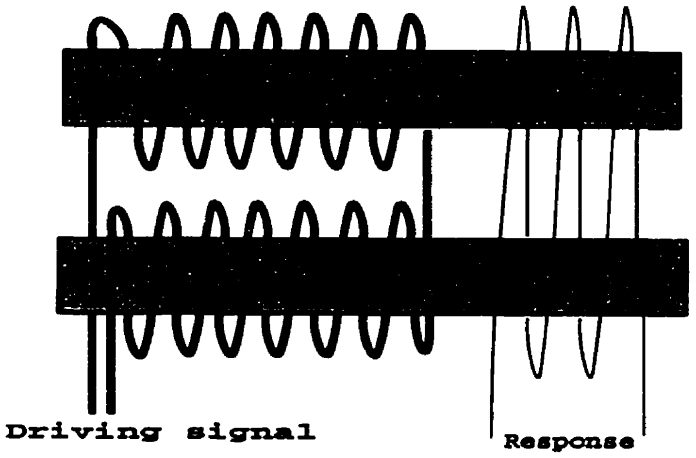

Figure A.5: Dual-core fluxgate magnetometer

One method to accurately detect the second harmonic signal over the much stronger first harmonic is to use two cores that allows the cancellation of the background primary signal [*Acuña et al*, 1969]. By winding the primary coil in opposing directions around either core and winding the secondary coil around both, the primary signal will cancel out, leaving only harmonics to be picked up in the secondary. Figure A.5 shows the geometry of this system. Once the second harmonic signal is recovered, the value of ΔH can be calculated and analyzed as required.

The magnetometers aboard OEDIPUS-C used a dual core design. In order to accurately measure the vector magnetic field, three mutually orthogonal detectors were mounted on the payload along a common axis. The sampling frequency was 854.16 Hz with a maximum (absolute) response of 65536 nT. The noise floor for these detectors was approximately 7 nT.

Appendix B

Electron Detector

Electrostatic analyzers are devices used to measure the flux and energy of incoming charged particles. Depending on the specific design, this type of detector is able to provide information on the range of energies of ions or electrons incident on the detector. Used in rocket research in the auroral zones, these detectors give valuable information about the environment that exists due to the interaction of the fields and particles in the upper atmosphere.

Figure B.1 shows a schematic of an electrostatic analyzer. These devices are designed to collect and analyze charged particles, sorting them by their incident energies. A particle entering along the center trajectory in figure B.1 enters between the curved plates, which are set at a specific voltage difference, creating a constant radial electric field. The electric field then causes the particle to be deflected. If the electric force supplies the correct centripetal acceleration to negotiate the curve, the particle will negotiate the curve and exit the electric field region and enter the remainder of the detector.

The equations for the electric fields and electron energy in a curved plate analyzer follow:

$$\vec{F}_{esa} = qE\hat{r}; \qquad \vec{F}_c = -\frac{mv_c^2}{R}\hat{r}; \qquad \vec{F}_c = \vec{F}_{esa}; \quad E_k = \frac{1}{2}mv_c^2 = \frac{qER}{2} \qquad (B.1)$$

With F_c the centripetal force the particle experiences, F_{esa} is force experienced

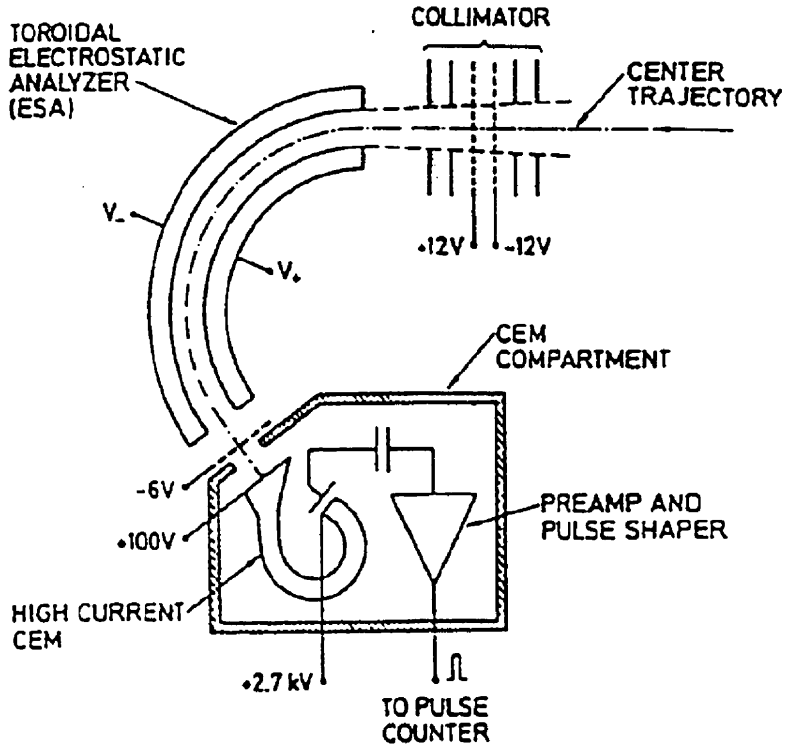

Figure B.1: Curved plate electrostatic analyzer, figure courtesy [*Vo*, 1992.]

by a particle with charge q in the curved plate region. The electric field $\vec{E} = E\hat{r}$ is the radial electric field in the curved plates, and E_k is the kinetic energy of the particle with velocity v_c.

Particles with kinetic energies (E_k) greater than $\frac{qER}{2}$ (in other words, $v > v_c$) will collide with the outer wall, whereas those with smaller energies ($v < v_c$) will be deflected into the inner wall. To collect a broad spectrum of energies, one need only to adjust the voltage, selecting for different energies as needed. The finite width of the gap determines the energy resolution of the detector. Once the electron exits

the deflection region, it enters the channel electron multiplier (CEM). This device creates an avalanche of electrons that are detected by the pulse counter.

Particle flux is the number of particles (N) passing through a unit area (ΔA) per unit time (Δt). The electric current density is then simply the charge of the individual particle multiplied by the flux.

The determination of flux and current requires analysis of the data from the electron detectors. Several quantities should be defined to allow for this analysis.

The differential energy flux j_E is measured over each energy bin in the electrostatic analyzer, and is the kinetic energy flux per unit solid angle (Ω) per unit energy, with units of $keVcm^{-2}ster^{-1}s^{-1}keV^{-1}$. The count rate (C) of an electrostatic analyzer can be shown to be proportional to j_E.

Differential electron flux is $j = \frac{j_E}{E}$, in other words the differential energy flux per unit energy:

$$j = \frac{N}{\Delta A\, \Delta t\, \Delta\Omega\, \Delta E} \tag{B.2}$$

Electric current density J is found by integrating differential particle flux j over energy and solid angle and multiplying by charge per particle q.

The geometry factor (G) is the quantity that relates the count rate (C) of the detector with the differential energy flux, $G=\frac{C}{j_E}$. For the OEDIPUS-C forward payload, G was $5 \times 10^{-6}cm^2ster$ for the 90° detector, and $1 \times 10^{-6}cm^2ster$ for the 45° detector.

For curved plate analyzers, the energy resolution $\frac{\Delta E}{E}$ is constant over all energy ranges, and for OEDIPUS-C it was equal to 0.05.

The electron detectors aboard OEDIPUS-C were designed to take a measurement

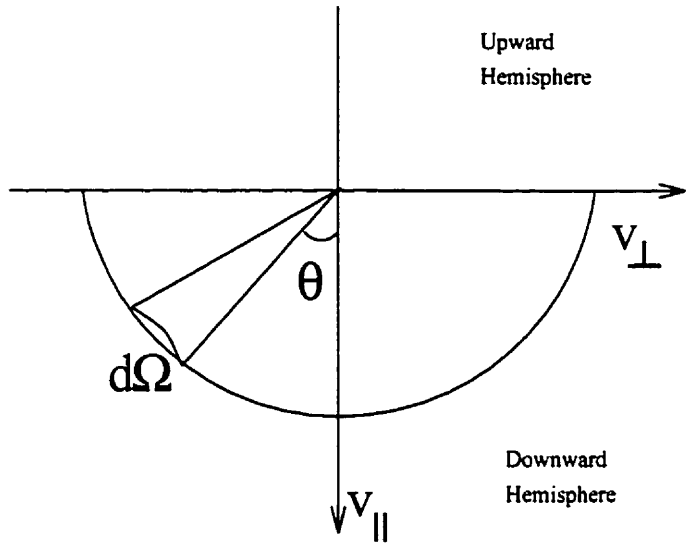

Figure B.2: Phase space coverage of electron detectors

of the ambient particle flux from one of two configurations: Perpendicular to the magnetic field and at a 45 degree angle looking upward. A diagram of the detector acceptance range appears in figure B.2. The total particle current density in the field aligned direction ($J_{||}$) can be calculated by integrating differential particle flux ($\frac{j_E}{E}$) over energy and downgoing angles, assuming isotropy in flux over ϕ and θ. An extra factor of $\cos\theta$ is needed to select the field-aligned component of the particle velocity.

$$
\begin{aligned}
J_{||} &= q\int\int \frac{j_E}{E} dE d\Omega \\
&\text{with } d\Omega = \sin\theta d\theta d\phi \\
J_{||} &= q\int_0^{2\pi}\int_0^{\frac{\pi}{2}} \sin\theta\cos\theta d\theta d\phi \int \frac{j_E}{E} dE \\
&= 2\pi[\frac{1}{2}\sin^2\theta|_0^{\frac{\pi}{2}}]\int \frac{j_E}{E} dE \\
&= \pi\int \frac{j_E}{E} dE
\end{aligned}
\tag{B.3}
$$

The configuration of the detectors is such that no electrons with upward velocity

components were measured.

Since the detector's energy acceptance ΔE is proportional to measured energy E, energy step size increased exponentially with center energy E in order to cover the range from 200 eV to 18 keV uniformly. The constancy of $\frac{\Delta E}{E}$ allows this factor to be taken out of the integral, which can be reduced to a sum over the 16 energy steps used by the instrument:

$$J_{\|} = q\pi \int \frac{j_E}{E} dE = q\pi \frac{\Delta E}{E} \sum_{i=1}^{16} j_{Ei} \tag{B.4}$$

Appendix C

HEX/REX

The high frequency transmitter/receiver pair outfitted for OEDIPUS-C produced frequency information on wave mode propagation in the ionosphere between the two sub-payloads. Plasma frequency information from this experiment was used to find the local plasma density during the flight.

The plasma frequency f_p is a quantity depending only on plasma density [*Chen*, 1984], and can be calculated from:

$$f_p^2 = \frac{n_e e^2}{\epsilon_o m_e} \tag{C.1}$$

with m_e = electron mass, e = electron charge, and f_p = electron plasma frequency in MHz. This frequency is the characteristic frequency that electrons will oscillate at due to random motions in the plasma.

The HEX/REX experiment measured the propagation of various electromagnetic wave modes in the ionosphere. These wave modes are functions of the orientation of the wave vector to the electric and magnetic fields.

An ionogram is an image of the frequency response of the receiver, which can show the wave modes as "traces" in the ionogram.

O and X modes are the ordinary and extraordinary modes of waves perpendicular to the magnetic field. R and L waves propagate along the magnetic field. W is the whistler mode. The traces that appear in figure C.1 are of the X and O modes. The plasma frequency f_p is shown, along with cyclotron frequency f_c, upper hybrid

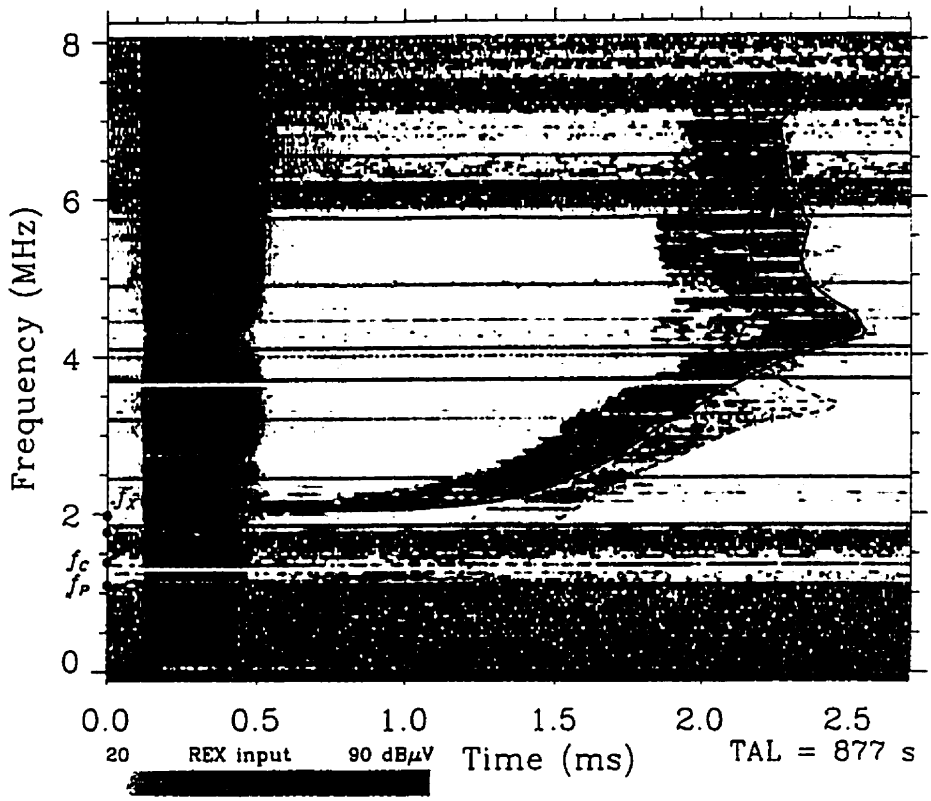

SH3 ionogram at TAL = 877 s, obtained when the payload was at an altitude of 327.9 km.

Figure C.1: Ionogram from OEDIPUS-C [*James and Calvert*, 1998.]

resonance frequency f_{UH} and instrument cutoff frequency $f_x = 2.0$MHz [*Prikryl et al.*, 2000].

The wave mode propagation frequencies are traced to show the frequency response over the scan.

Figure C.2 shows the electron density profile for the OEDIPUS-C experiment. Ionogram measurements of f_p and equation C.1 were used to determine n_e.

The measured electron density was much lower throughout the flight than ex-

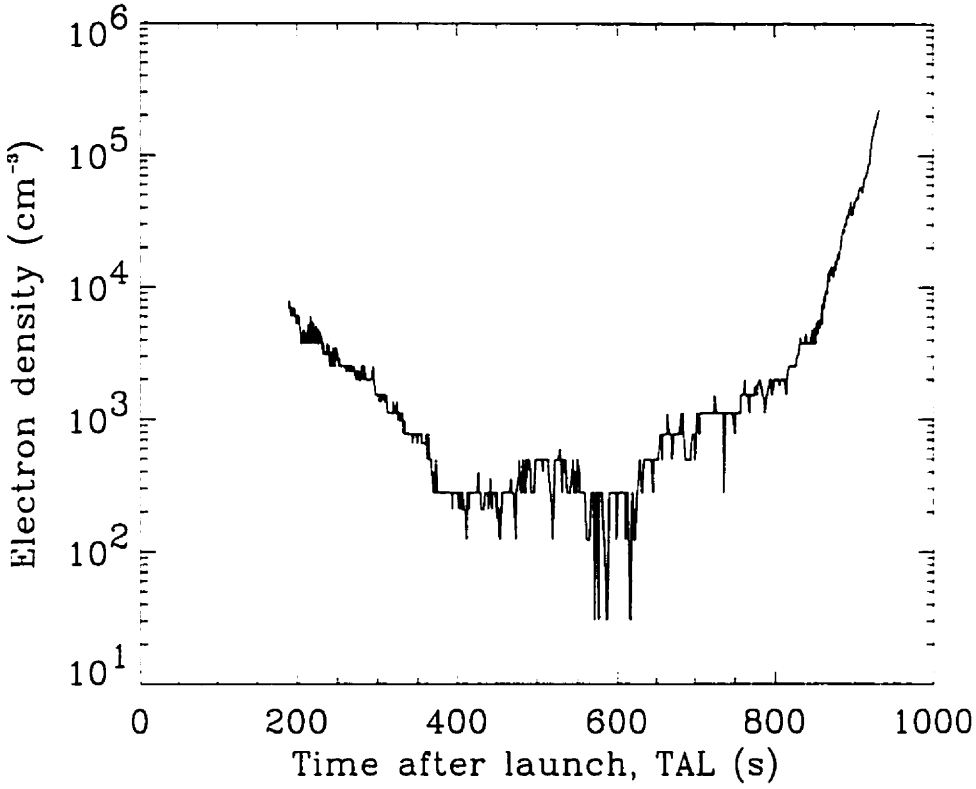

Figure C.2: Plot of electron density for OEDIPUS-C, courtesy Dr. H. G James, [personal communication].

pected, and reached the instrumental lower limit of $\sim$ 100 cm^{-3} near apogee.

Appendix D

Tables of Acronyms, Definitions, and Variables

Table D.1: Acronyms

AVC	Attitude Video Camera
CANOPUS	Canadian Auroral Network for the OPEN Program Unified Study
CEM	Channel Electron Multiplier
eV	electron-Volts
FAC	Field-Aligned Currents
FAST	Fast Auroral SnapshoT
GEI	Geocentric Equatorial Inertial coordinate system
GEO	Geocentric coordinate system
GIMA	Geophysical Institute Magnetometer Array
GM	Geomagnetic coordinate system
HEX/REX	High frequency EXciter/REceiver eXperiment
IGRF	International Geomagnetic Reference Field
IMF	Interplanetary Magnetic Field
ISIS-2	International Satellites for Ionospheric Studies
R	Rayleighs
LG	Local Geographic coordinate system
OEDIPUS-C	Observations of the Electric field Distributions in the Ionospheric Plasma- a Unique Strategy
RF	Radio Frequency
SPS	Soft Particle Spectrometer (aboard ISIS-2)
UT	Universal Time
VDA	Vehicle Data Axis

Table D.2: Definitions

Apogee	Highest point of rocket flight
Coning	Precession of symmetry axis of a body about the total angular momentum vector of that body
Detrend	Removal of a baseline offset to a data set in order to identify smaller structure with in the larger offset itself
Inverted-V	Structure appearing in electron energy spectrograms that indicate regions of accelerated, precipitating electrons
J	Electric current density
Keogram	Image produced by a meridian scanning photometer
Loss cone	Particles with pitch angles equal or less than the angle at which a particle will mirror below 100km are said to be within the loss cone
nT (nanoTesla)	Unit of magnetic field strength, equal to 10^{-5} Gauss
Nutation	Variation in coning angle for non-rigid or asymmetric spinning bodies
Pitch angle	Angle between the velocity vector of a particle and the magnetic field. For a constant velocity vector, the greater the velocity component parallel to the magnetic field, the smaller the pitch angle
Rayleigh	Unit of photon flux, equal to $10^6 h\nu \mathrm{cm}^{-2}\mathrm{ster}^{-1}\mathrm{s}^{-1}$, with ν the frequency of the photons measured
Spin	Induced rotation of spacecraft for stability purposes
Substorm	Magnetospheric disturbances that can produce increases in auroral activity

Table D.3: Variables

Chapter 1	
α	Pitch angle
$\vec{B}$	Magnetic field
$\vec{F}$	Lorentz force
$\vec{J}$	Current density
μ_o	Permeability of free space ($4\pi \times 10^{-7}\mathrm{N/A^2}$)
μ	Magnetic moment
r_c	Gyroradius
$\vec{v}_{\|\|}$	Particle velocity parallel to magnetic field
$\vec{v}_{\perp}$	Particle velocity perpendicular to magnetic field
Chapter 2	
D	Declination
$\|\vec{F}\|$	Total magnitude of the magnetic field
$\vec{H}$	Horizontal component
I	Inclination
X	North component
Y	East component
Z	Vertical component
Chapter 3	
$\vec{L}$	Total angular momentum vector
ξ	Coning angle
$\rho(t)$	Spin phase or roll angle
α	Right Ascension
δ	Declination
ϕ	Longitude
ψ	Latitude
θ	Mean sidereal time; angle eastward between point of Aries and Greenwich meridian
$\hat{i}$, $\hat{j}$, $\hat{k}$	Unit vectors
$\vec{X}$, $\vec{Y}$, $\vec{Z}$	Payload coordinate axes; $\vec{Y}$ = Vehicle Data Axis (VDA), $\vec{Z}$ = Spin axis
M	Rotation matrix

Table D.3: *continued on next page*

Table D.3: *continued*

Chapter 4	
$\Delta\vec{B}$	Perturbation magnetic field
$J_{\|\|}$	Field-aligned current density estimated from electron detector data
$J_{pert.}$	Field-aligned current density estimated from magnetic field perturbations
$\frac{\Delta E}{E}$	Energy resolution of an electrostatic analyzer
Appendix A	
$\vec{B}$	Magnetic flux density
B_s	Saturation point of magnetic material
$\vec{H}$	Magnetic field
μ	Magnetic permeability
μ_o	Magnetic permeability of vacuum; $\mu_o = 4\pi \times 10^{-7} N/A^2$
ε	Electromotive force (emf) voltage response. also V_s
Appendix B	
C	Count rate
$E\hat{r}$	Radial electric field
E_k	Kinetic energy
F_c	Centripetal force
F_{esa}	Force experienced by a charged particle in an electrostatic analyzer
G	Geometry factor
j	Differential electron flux
j_E	Differential energy flux